Increasing Efficiency and Power Density Of a Liquid Piston Air Compressor / Expander With Porous Media Heat Transfer Elements

A THESIS
SUBMITTED TO THE FACULTY OF
UNIVERSITY OF MINNESOTA
BY

Jacob Henry Wieberdink

IN PARTIAL FULFILMENT OF THE REQUIREMENTS
FOR THE DEGREE OF
MASTER OF SCIENCE

Perry Y. Li & Terrence W. Simon

December, 2014

Acknowledgements

I would like to thank my advisers Professor Perry Li and Professor Terry Simon, as well as Professor James Van de Ven and Dr. Farzad Shirazi, for their guidance and support during this project. Their feedback and insight, as well as their words of encouragement were invaluable to me. I would also like to thank all of my research colleagues and friends at the University of Minnesota and the University of Virginia, especially Bo Yan, Pieter Gagnon, Chao Zhang, and Mohsen Saadat, for their collaboration and support. A special thanks is due Srinidhi Murali for her friendship and her feedback over the past two years. To all of my other friends and family who made getting to this point possible, thank you for your prayers, support and encouragement. I am so grateful to my parents, Wes and Judy, for their unconditional love and for everything they have done to equip me for a life of service.

This work is supported by the National Science Foundation under grant NSF-EFRI #1038294, and University of Minnesota, Institute for Renewable Energy and Environment (IREE) under grant: RS-0027-11

Abstract

In this thesis, a power dense and efficient air compressor/ expander is investigated experimentally. High power density and high efficiency are realized with a quasi-isothermal process, made possible by a liquid piston compressor/ expander and the addition of porous media heat transfer elements. Uniform and non-uniform distributions of porous media are considered and compared with a baseline case.

Experiments are conducted using a 2.2 L displacement compressor/ expander. Air is compressed from 7 bar to 210 bar in compression tests and expanded from 210 bar to 7 bar in expansion tests. Baseline compression times vary from 2s to 400s and compression power density varies from 4 kW/m^3 to 600 kW/m^3. Baseline expansion times vary from 1s to 400s and expansion power density varies from 4 kW/m^3 to 2 MW/m^3. The baseline compression experiments covered. This study finds that as power density increases, efficiency decreases. At 90% efficiency, a moderate amount of porous media (uniform distribution of 76% porosity) improves compression power density by a factor of 10 and expansion efficiency by a factor of 17. Further improvements are possible with an optimized porous medium geometry.

These results have implications for many applications where efficient gas compression/expansion is required including: compressed air for energy storage at scales that range from residential-scale to grid-scale, pneumatics, compressed industrial gasses, and compressed gaseous fuels like hydrogen and natural gas. Quasi-isothermal compression and expansion also enables the realization of thermodynamic cycles that require isothermal compression or expansion.

Table of Contents

List of Tables

List of Figures

Chapter 1: Introduction

1.1 Energy Storage Background

The demand for environmentally-friendly, reliable, and affordable electricity has never been higher and is projected to rise for the foreseeable future. In 2013, the U.S. used 3,692 TWh of electricity [1] and according to a 2012 NREL estimate, the demand could be as high as 5,000 TWh by 2050 [2]. In the U.S., most electricity is generated from non-renewable sources. In 2013, 67.5% of all electrical generation in the U.S. came from fossil sources and another 19.4% from nuclear [1]. Fossil fuels are a finite resource and electrical generation from fossil fuels is the largest single source of greenhouse gas (GHG) emissions in the U.S. [3] . For these reasons and more, there has been a push from policy makers to incorporate more renewable energy sources into their energy mix or renewable portfolio standard (RPS). Minnesota, for example, has a goal of 25% from renewable sources by 2025 across the state and 30% from renewable sources by 2020 from utility providers that operate nuclear powered plants [4].

While there are a number of political, societal, and economic challenges to incorporating more renewable energy sources into the energy mix, there are also significant technical challenges to overcome. Biomass, fossil fuels, and nuclear sources naturally store energy until it is released by a chemical or nuclear reaction. Energy from wind and solar, however, is inherently irregular on a number of timescales: seasonally, daily, and hourly. While some of this variability can be predicted, it becomes more and more difficult to maintain grid operating frequency as more of these variable generation sources are integrated. In addition to the variability in supply, there is also variability in energy demand

on a number of timescales. Grid-scale energy storage can provide a means for storing energy when supply exceeds demand and a means for recovering energy when demand exceeds supply.

Currently, pumped hydro provides 93% of the energy storage capacity in the U.S. The remainder consists of compressed air energy storage (CAES) (3%), thermal storage (3%), and electrochemical storage (1%) [5] (only systems with rated power >10kW were considered). Although CAES systems provide only a small fraction of current energy storage capacity, they have attracted significant attention from researchers and industry because of a number of benefits over other energy storage alternatives. The benefits of CAES include moderate ramp rates, scalability, reasonable cost, and potentially high energy efficiency [6]. Compared to batteries, CAES systems are attractive because they do not use toxic materials, they do not degrade with cycling or depth of discharge, and have longer life plant life [7]. As wind is the fastest growing renewable power generation source (see Fig. 1.1.1), energy storage systems that pair well with wind, including CAES systems, have also received significant attention. Previous research has included economic feasibility studies [8] [9] [10], controller design [11], system modeling [12], location studies [10] and comparisons with other energy storage methods [7] [13].

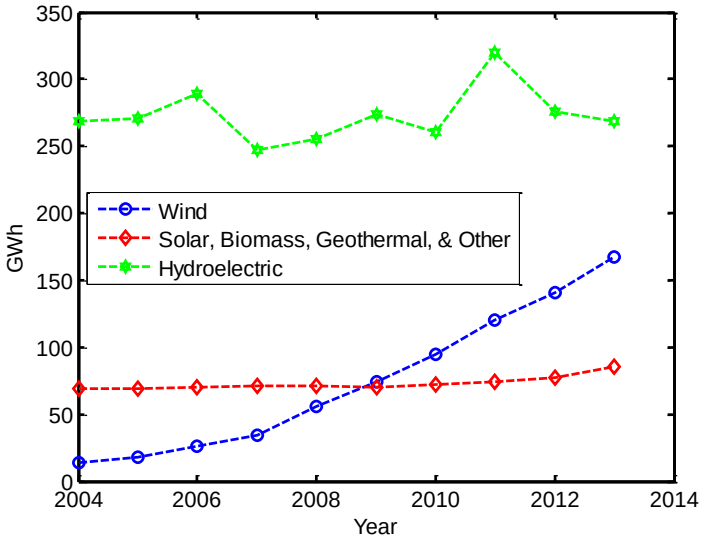

Fig. 1.1.1. Annual U.S. electrical generation from renewable sources. Data retrieved from [1].

Of particular interest to this thesis is a novel compressed air energy storage system suggested by [6]. The authors present a system that has several advantages over conventional CAES. These benefits include improved efficiency with isothermal compression/ expansion (as opposed to the more conventional adiabatic processes), improved power density, geographical freedom with an "open-accumulator" storage vessel, and no dependence on fossil fuels for energy recovery. The proposed system would be integrated with offshore wind farms allowing energy to be stored before it is converted to electricity and allowing electrical transmission systems to be sized for average power as opposed to peak power. This system will be discussed in more detail in Chapter 3.

Critical to this system, and any isothermal compression system, is an efficient and power-dense compressor/ expander. For compression or expansion to remain near-isothermal, the compression or expansion power must be balanced with heat transfer to or from the environment. Naturally, any discussion on efficiency improvement turns to heat

transfer augmentation and a number of approaches have been studied to approach this isothermal goal.

One approach is to use several adiabatic compression stages with intercooling between stages. In [14] the performance of a multistage adiabatic compressor with intercoolers was optimized using an ideal gas model. The optimum solution was found to consist of stages with equal pressure ratio. In [15] a multistage adiabatic CAES system with inter-stage heat exchangers was modeled and a thermodynamic analysis conducted. This study found that efficiency increased with the number of stages. The authors concluded that adiabatic compressor/expanders and inter-stage heat exchangers, both of which are widely available, could be combined to form a technically feasible system.

In [16], a three stage near-isothermal liquid piston compressor was simulated. Rather than using inter-stage heat exchangers, droplet spray cooling was used to facilitate heat transfer in the compression chamber. Three stages were used with a total pressure ratio of 350. The results of this analysis found the total efficiency to be 89.0% as compared to the 26.7% adiabatic/conventional case. In another study by the same author [17], droplet spray cooling at high mass loadings was found to improve compression efficiency from 71% (adiabatic) to 98% in a 5 kW compressor with a pressure ratio of 10.

In [18], a near-isothermal reciprocating air compressor with spray-cooling was discussed. This compressor uses multiple nozzles with an optimal timing of water spray to improve efficiency. The geometry of the compressor discussed was a 200 mm bore x 350 mm stroke. The water spray system was able to provide up to 100 grams of droplets per stroke. Experiments included a variety of nozzles and compression cycle times varied from

50-200 RPM. Experimental results showed a 28% savings in work input, compared to an adiabatic system, for a pressure ratio of 25 at 100 RPM. Temperature rise was kept under 100 C throughout the compression process.

There has also been a commercial interest in spray cooling for improving compression/ expansion efficiency. LightSail Energy, an American company, holds a number of patents related to droplet spray cooling technology. According to their website, LightSail's second generation system will be the first CAES system to outcompete gas-fired peaker plants [19]. Similarly, SustainX, another energy storage company, uses aqueous foam to facilitate heat exchange in a near-isothermal compressed air energy storage system. According to SustainX, foams can be created at a lower energy cost than sprays and can be engineered to last as long as is desirable. SustainX claims to have reached compression/expansion efficiencies as high as 95% on a megawatt-scale system [20]. SustainX has launched a 1.5 MW CAES demonstration system in Seabrook, New Hampshire that can run at peak power for one hour [5].

The use of an optimized compression/expansion rate profile has also been shown to improve performance in a number of studies. In [21], a simple heat transfer model where hA is constant is used to find the optimal compression/expansion rate trajectory. Reference [22] developed this further by allowing hA to vary as a function of air volume and in [23], the optimal profile was found numerically for a more general heat transfer condition than used in prior work. In a more recent study by [11], an iterative adaptive nonlinear controller was developed for a liquid piston compressor to track an optimal temperature-volume trajectory. This control methodology iteratively estimates h during the compression

process, ensuring that the optimal trajectory is followed. The key advantage that this method has over previous methods, is that it does not rely on a heat transfer model or assumption about *hA*, which is often uncertain. For the same efficiency, optimal compression profiles improved power density by up to 33%. These optimal trajectories were found to improve efficiency by up to 2% as compared to cases with constant compression rates at the same power level. These experiments were carried out on an experimental facility with a limited flow capability. It should be noted that without this flow limitation, further improvements in power density and efficiency are possible.

Additionally, the use of porous media has been shown to improve compression efficiency. Reference [22] presented experiments where aluminum meshes of different mass were used with a solid piston in low power, low pressure (7 bar maximum absolute pressure) compression tests. These experiments showed a reduction in temperature rise as mesh mass increased and compression rate decreased. This study also presented compression tests with a liquid piston compressor using a copper mini-tube array inside the compression chamber. The maximum temperature rise in these tests was reduced 86.6% from 109K to 15K at the same power level, 25W, and same pressure ratio, 7.

The use of porous media in a liquid piston compressor has also been studied computationally by Zhang. In [24], an interrupted plate style heat exchanger was designed and studied computationally. A key result from this study is a heat transfer correlation based on hydraulic diameter that is valid for a number of different interrupted plate geometries. Another study by the same author [25] found the optimal distribution of a metal foam heat exchanger in a liquid piston compressor. Experiments in this thesis will be

compared with the heat transfer coefficient correlation developed by Zhang and will experimentally investigate non-uniform porosity distributions.

Finally, [26] and [27] showed experimentally that the efficiency and power density of a liquid piston air compressor could be improved by adding surface area to the compression/expansion chamber with porous media. Five different porous inserts were considered in compression tests with a pressure ratio of 10. For a compression efficiency of 95%, the power density was increased by an order of magnitude with porous media. The authors showed that for all five uniform distributions of porous media, compression efficiency was a function of power density per specific area.

While there exists a large body of literature related to near-isothermal compression, many of the examples cited in the preceding paragraphs have been based on modeling and simulation. The experimental validation that is available tends to be for relatively low pressure (7 to 25 bar). In general, there is a lack of experimental data available to validate the various simulation results at the high pressures that would be necessary for a practical CAES system (~200-300 bar). Sprays, foams, porous media, inter-stage cooling, and optimized compression/ expansion rate control have all been shown to improve efficiency, but there has not been a conclusive study on which methods, or combinations of methods are best for a given set of conditions.

1.2 Objectives and Hypothesis of this Thesis

One goal of this thesis is to collect and analyze experimental data at conditions that are representative of those in a commercial second stage compressor/ expander. These data will be useful for guiding the design of a commercial compressor/ expander. Additionally,

these data will be compared with the heat transfer correlation proposed in [24] and similar low pressure experiments presented in [27]. Additionally, experimental results will be compared qualitatively with the optimal compression rate profiles.

Experiments are conducted using a liquid piston compressor/expander with porous media heat transfer elements. These experiments test the hypothesis that increasing the mass and total heat transfer area of these porous media will improve both the power density and efficiency of the compression and expansion processes.

Additionally, these experiments will test the hypothesis that for a given amount of porous media there exists an optimal way to distribute it in the chamber and this optimal distribution is with all of the porous media at the top of the chamber. This has been shown computationally in [25] and is expected because for an efficient compression/ expansion process (that is, a process with constant internal energy) there must be a balance between compression/ expansion power and heat transfer. Placing porous media in regions occupied by air when instantaneous power is high helps augment heat transfer in this region. Additionally, during compression the air velocity is lower in the top region of the compressor. Adding porous media increases velocity, and hence the convective heat transfer coefficient, and the total surface area in this region. Placing porous media in the top region allows it to be exposed to air for the longest amount of time, as opposed to porous media near the bottom of the chamber which is submersed by the liquid piston for the majority of the process.

Based on the work in [23] and [11], this thesis also claims that for a given efficiency, power density can be increased with an optimal compression/expansion rate profile.

1.3 Thesis Outline

This thesis is organized into seven chapters with appendices following for additional information. The first chapter has introduced the need for energy storage and has briefly presented a novel compressed air energy storage system. Relevant literature on the topic has been reviewed and gaps therein have been noted. The objectives and hypotheses of this thesis have been presented.

Chapter two describes in detail the experimental facilities used in these tests. The primary facility is a 2.22L liquid piston air compressor/expander with a maximum operating pressure of 210 bar.

Chapter three describes in detail the CAES architecture that was introduced in chapter one and explains liquid piston compression/expansion in detail. Modeling assumptions, governing equations, and figures of merit are presented. Chapter three also contains an uncertainty analysis.

Chapter four describes the various experiments that were conducted and explains the goals for each experiment. These experiments include water holdup tests in porous media, shakedown testing of the experimental facility, baseline compression/expansion tests, as well as compression/expansion tests with uniform and non-uniform porous media inserts.

Chapter five presents the experimental results of the compression and expansion tests.

Chapter six interprets and discusses the trends seen in chapter five. Trends in the experimental heat transfer coefficient are discussed and compared with a CFD-derived heat

transfer correlation. Implications for compressor/ expander design and future research are also discussed.

Chapter seven provides a conclusion and summary of the significant findings of this thesis.

Appendix A contains detailed design calculations. Appendix B contains a table of all the experimental data. Appendix C contains a list of nomenclature used throughout this thesis. Appendix D contains several figures from this thesis that have been reprinted in grayscale for better viewing in black and white. The MATLAB processing codes used to process experimental data, raw and processed data, and figures will be made available electronically.

Chapter 2: Experimental Facilities

2.1 System Requirements

The experimental facility was designed to study the compression and expansion of air with a liquid piston. The facility is required to be able to withstand the high pressures, up to 210 bar, encountered during the compression and expansion processes - this includes preventing leakage and withstanding the high pressure-induced forces. The facility is also required to be fitted with instrumentation to measure pressure, volume, and temperature. For these studies, it was critical that the compression / expansion chamber allows for the addition and rearrangement of porous media. The system needed to be controllable; specifically, it was desirable that compression and expansion rates be controlled. Due to the corrosive nature of water hydraulics, the materials needed to be water compatible. Finally, it was desirable to have a system with a wide operating range.

2.2 The Mechanical and Structural Components

A schematic of the entire schematic is shown in Fig. 2.2.1. The various components and subsystems in this schematic will be discussed in greater detail in the following section.

The heart of the experimental facility is the liquid piston compression/expansion chamber (item 11 in the schematic). This is the same chamber that was presented in [27] and detailed drawings can be found in the appendix. The compression/expansion chamber consists of three main parts: the cylinder, the base, and the top cap. A picture of the compressor is shown in Fig. 2.2.2.

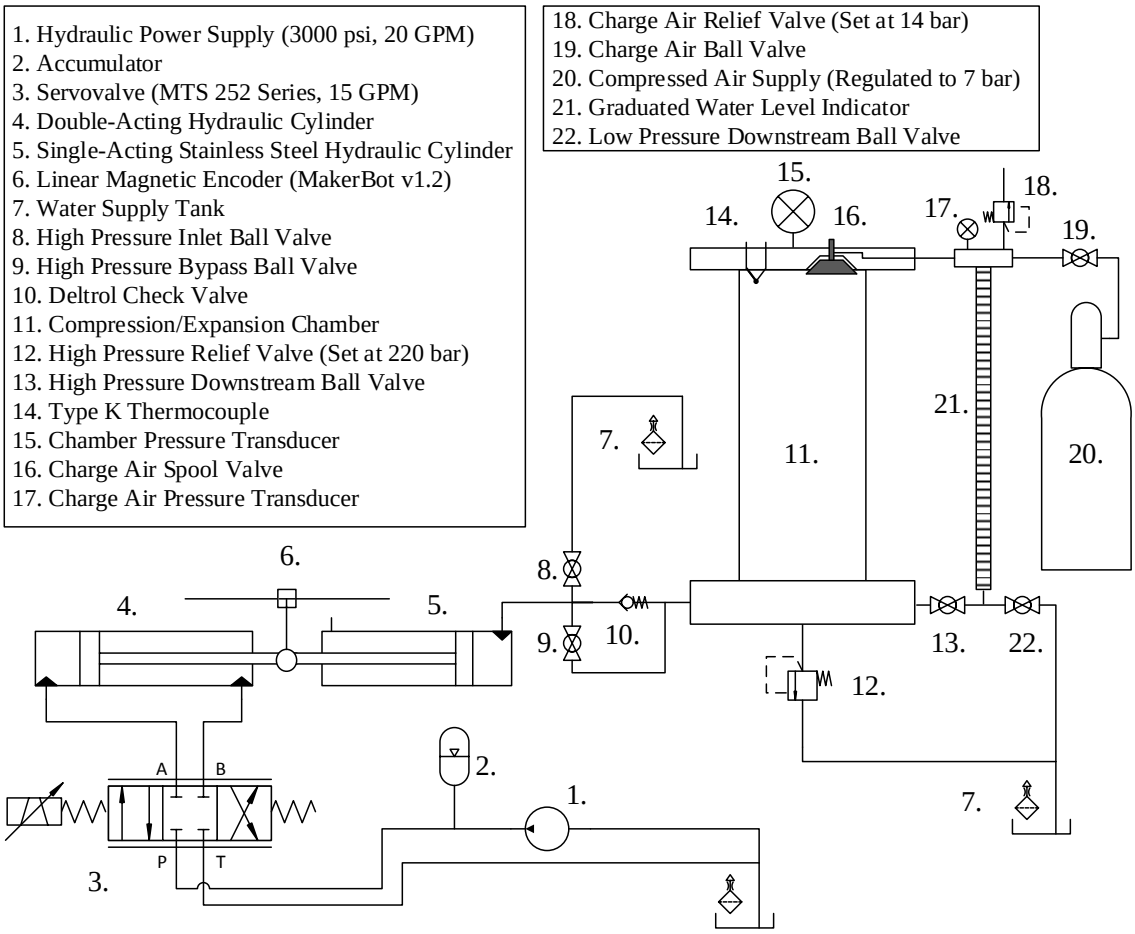

Fig. 2.2.1: Detailed schematic of experimental facility

The cylinder is made from 304 stainless steel and was designed for operation at 210 bar with a safety factor of 4 based on a standard hoop stress calculation. The internal diameter of the cylinder is 76 mm (3”) and the length is 483 mm (19”), a length to diameter ratio of 6.3. The exact displacement of the cylinder was measured to be 2227 mL.

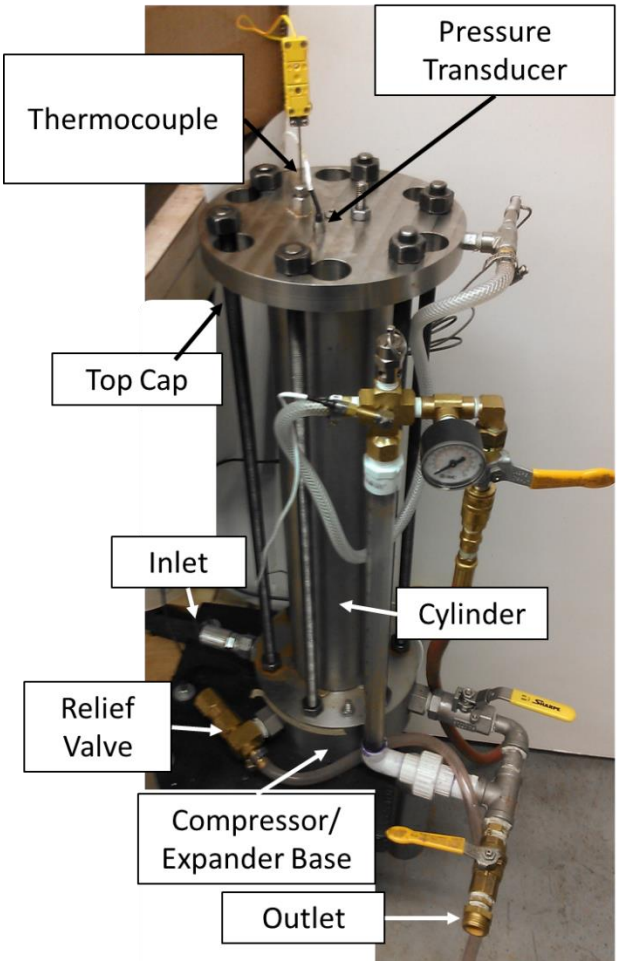

Fig. 2.2.2: Picture of compressor/ expander used in experiments

The base, shown in Fig. 2.2.3, serves as a manifold for inlet and outlet connections. The base is made from 316 stainless steel for corrosion resistance. An o-ring is used in a piston seal configuration to seal the high pressure side of the chamber from ambient pressure. The ports in the base have a diameter of 19.0 mm (0.75”). To ensure uniform liquid piston formation and to prevent jetting, a deflection plate was installed on the base where flow enters the cylinder. A safety relief valve (J.E. Adams Model #7438) was installed on the base and set to 220 bar to prevent over-pressurization of the chamber. A pressure gauge (not visible in Fig. 2.2.2 or Fig. 2.2.3) was also installed on the base to indicate pressure.

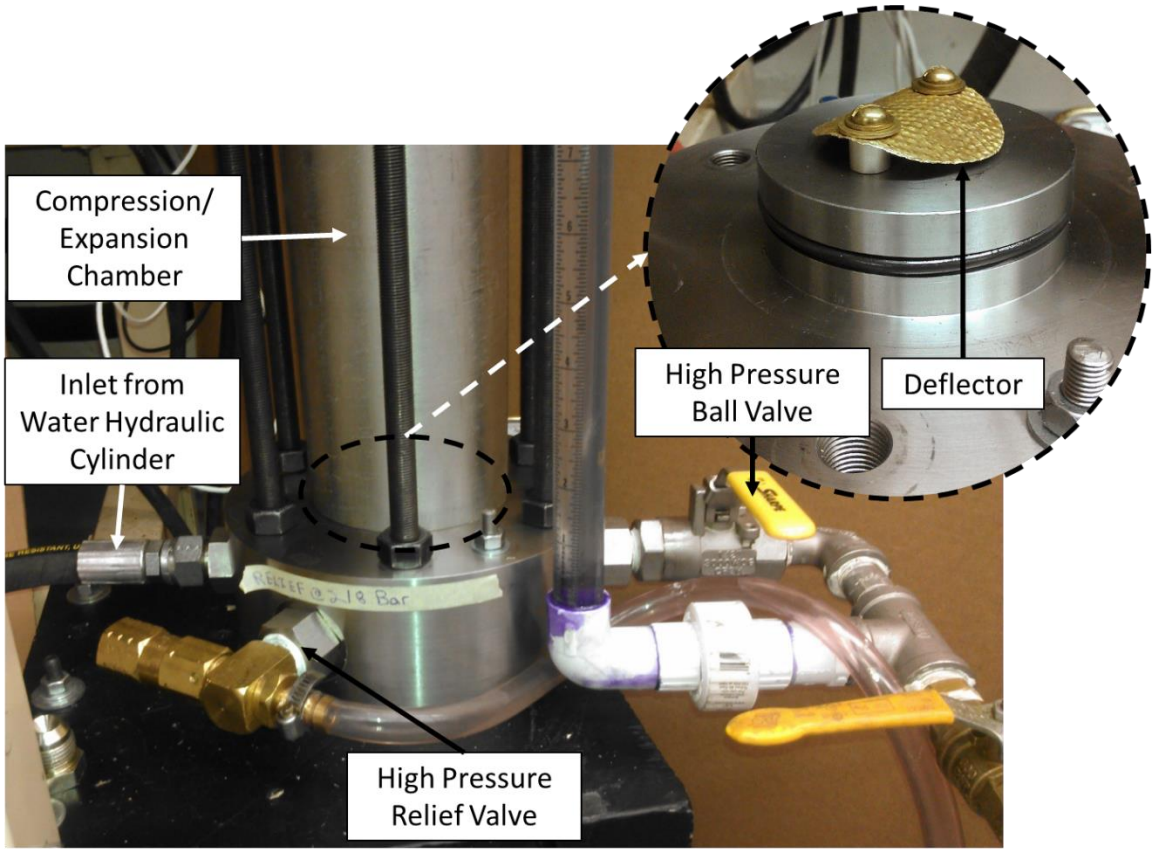

Fig. 2.2.3: Picture of compressor/ expander base

The top cap serves as a connection point for instrumentation and valving. It is connected to the base with 6 steel tie rods (ASTM A193 Grade B7 UNF 1/2 – 20). An o-ring (AS568-238, Durometer 90A) is used in an axial face seal configuration to seal the high pressure side of the compression chamber from ambient pressure. A spool valve is integrated into the top cap to provide an inlet for charge air.

In order to achieve high accuracy volume measurements over a wide range of compression and expansion speeds, a unique method for introducing flow into the compression chamber is used. Two hydraulic cylinders are oriented along the same axis, but in opposite directions, with the rods of each cylinder connected. This configuration, shown in Fig. 2.2.4, results in the linear speed of the two pistons being equal.

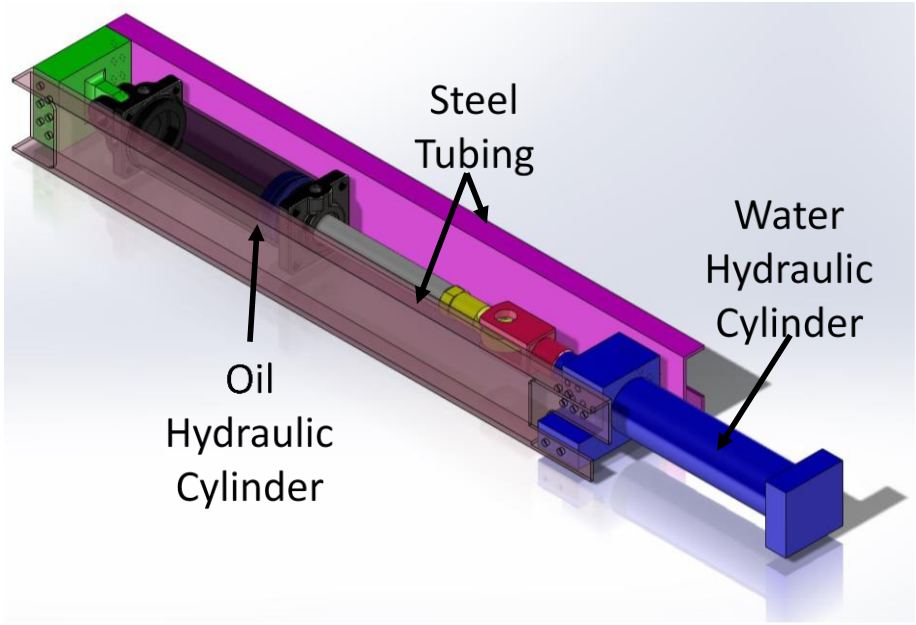

Fig. 2.2.4: 3D sketch of opposed hydraulic cylinder configuration

The first cylinder is an oil hydraulic cylinder. It is controlled with a servohydraulic circuit. The second cylinder is designed for water hydraulics and is plumbed directly to the liquid piston. This design allows oil hydraulic components to be used, which are less expensive and more easily available. The second advantage of this system is that it allows the displacement of the water hydraulic piston to be measured with a linear encoder. This direct measurement of the volume is both accurate and of high precision. The servohydraulic portion of this configuration is shown in Fig. 2.2.5.

The two hydraulic cylinders are held together with two sections of steel tube, one on each side the cylinders. At full pressure, the steel sections hold a combined tensile load of 660 kN (37,000 lbf). The steel tube sections are bolted directly to the water-side hydraulic cylinder using 7 UNC ½-13 bolts. These bolts provide a clamping force so that the C-channel and hydraulic cylinder are held together by friction. This prevents the bolts from high stress cyclic loading. In the same way, bolts are used to clamp the channel to a

clevis eye on the oil-hydraulic side. Figure 2.2.4 shows a sketch of the opposing cylinders and Appendix A shows the detailed design calculations.

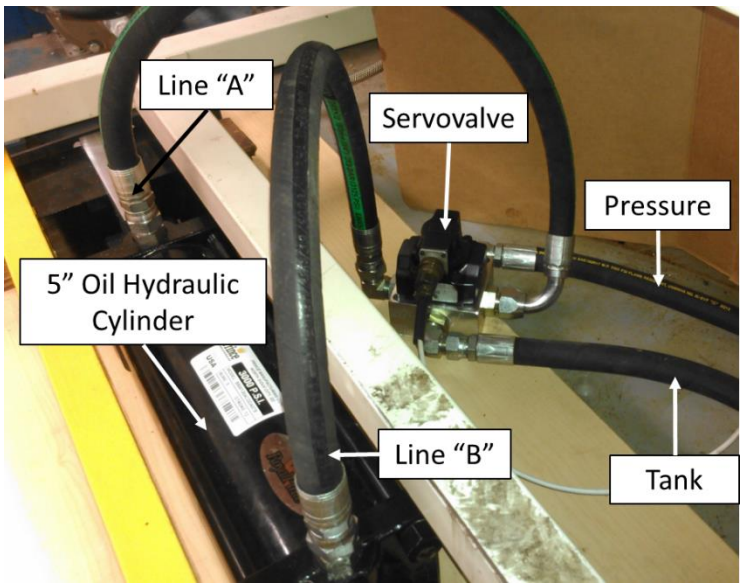

Fig. 2.2.5: Picture of oil hydraulic cylinder

Figure 2.2.6 shows the flow circuit between the water hydraulic cylinder and the liquid piston compression/expansion chamber. Unless otherwise specified, all connections are made with high pressure hydraulic hoses. Hoses with an inner diameter of 12.7 mm (0.500” or -08) were selected as a standard size which provided a good compromise between pressure drop and hose flexibility which aided in the installation and maintenance of the facility. These hoses have a non-negligible compliance that must be corrected for. This will be addressed in Chapter 3.

A ball valve isolates the tank from the rest of the high pressure lines. This is used for filling the system with water and bleeding any air from the lines. A check valve is installed inline as a safety feature to prevent the system from rapidly de-energizing in the

event of an accident. A second ball valve allows this check valve to be bypassed for expansion tests.

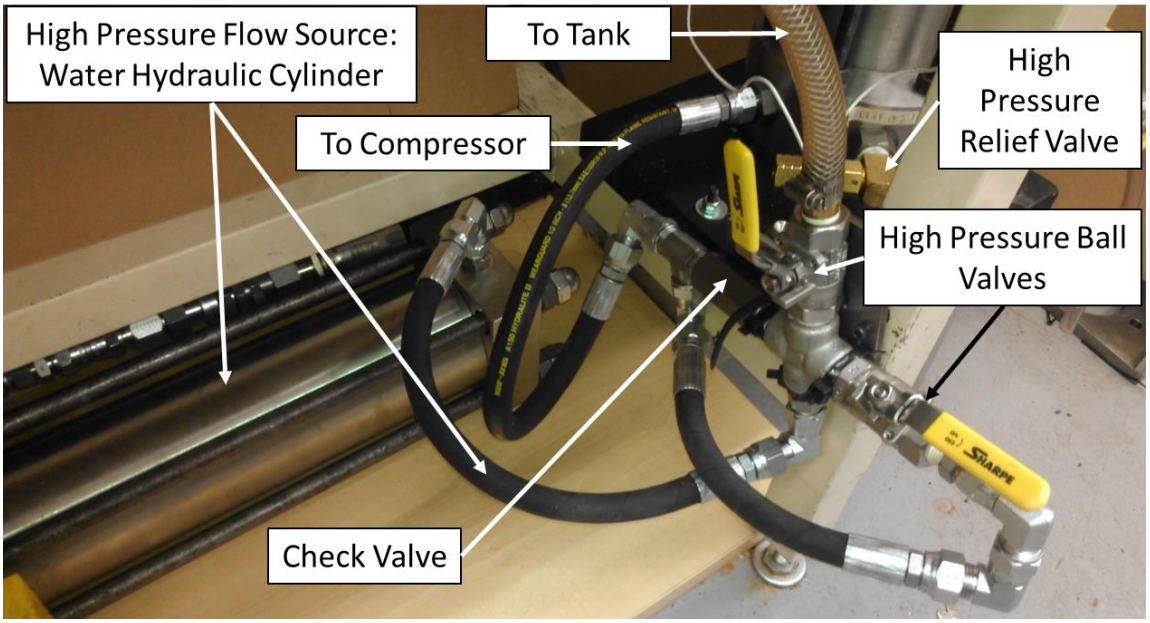

Fig. 2.2.6: Picture of water hydraulic cylinder and connections

Figure 2.2.7 shows the low pressure/charge air section. Here, a third ball valve isolates the high pressure in compression/expansion chamber from the sight glass. The sight glass is a clear PVC tube with graduations. When the high pressure ball valve and the spool valve on the compression/expansion chamber are open, the water level in the sight glass is the same as the water in the compression/expansion chamber. This is used to ensure that the starting height of the liquid piston is always the same. The top section of the sight glass provides a connection to the compression/expansion chamber and to a regulated compressed air supply. There is also a pressure relief valve, and pressure transducer in this section.

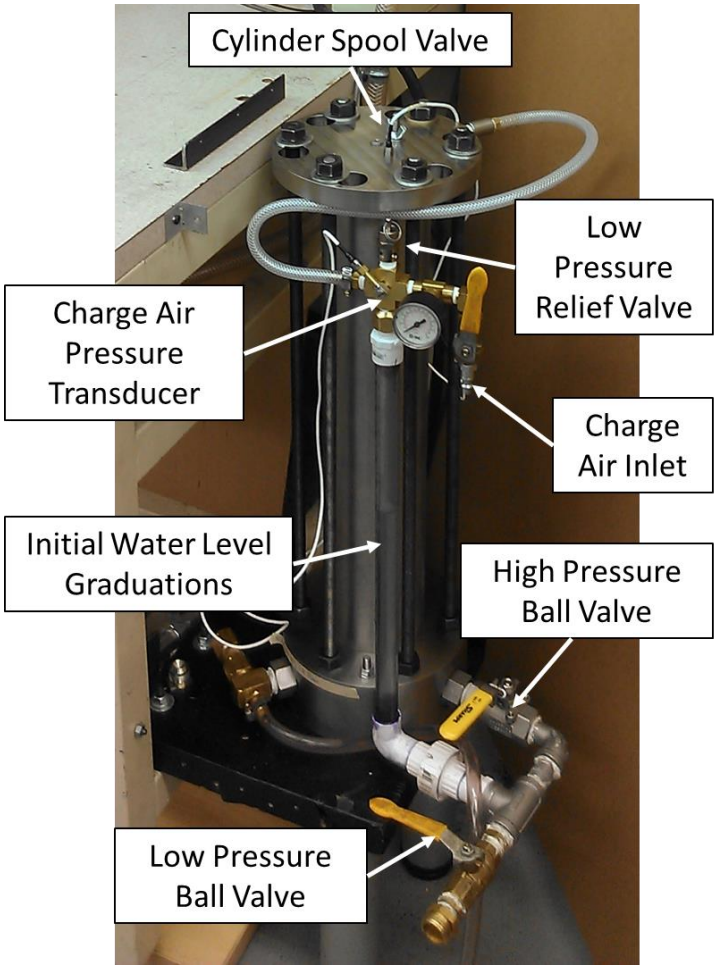

Fig. 2.2.7: Picture of low pressure/ charge air section

2.3 Instrumentation and Control

This experimental facility is equipped with two pressure transducers. The first transducer (Kulite Mdl # XTL-123B-190-3000SG) is mounted on the top cap of the compression/expansion chamber and directly measures the pressure of the chamber. It can accurately measure pressure up to 210 bar. This transducer was selected because of its high accuracy, small size, and fast response time. The second transducer (Kulite Mdl # XTL-123CEG-190-100SG) is of a similar style, but can measure pressure up to 7 bar. This transducer is used in the sight glass/charge air section to measure the initial pressure of the

system. Section 3.2 will explain how using two pressure transducers reduces the uncertainty in the experiments.

A type K thermocouple (Connax Technology P/N K-SS6-G-MPJFC) is installed in the compression/ expansion chamber. The tip of the thermocouple is placed 12.7 mm (0.500”) from the top cap. The thermocouple is used to measure the air temperature at steady state. The thermocouple is not used for measuring the transient temperature because it measures the temperature in only one place in the temperature field and has a relatively slow response. The thermocouple is used with an ice bath temperature reference. A low pass filter with a 30 Hz cut-off frequency is used to remove high frequency electrical noise from the measurement. A polynomial correlation available from NIST is used to relate the measured EMF to temperature [28].

To measure the displacement of the water hydraulic cylinder piston, and thus the volume of water displaced from the cylinder to the liquid piston, a sliding mechanism with a linear magnetic encoder was designed and attached to the cylinder. A picture of this mechanism is shown in Fig. 2.3.1. This mechanism is built around a linear magnetic encoder kit available from MakerBot (Fig. 2.3.1 a)). This encoder is capable of measuring a linear displacement with a resolution of 15 microns. This corresponds to a displacement resolution of ~0.11 mL when connected to the water hydraulic cylinder.

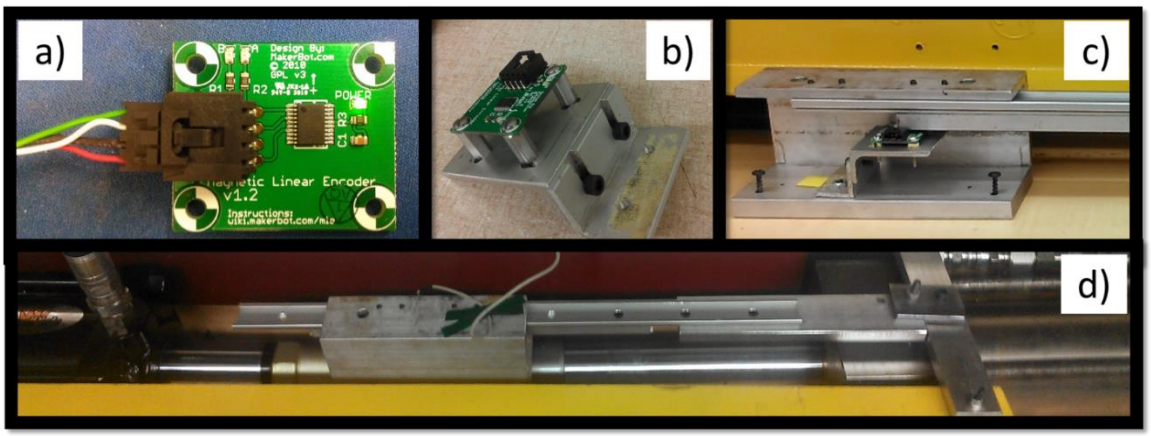

Fig. 2.3.1: Linear magnetic encoder: a) purchased encoder board b) encoder board installed on adjustable mount c) encoder board and magnet slider d) encoder slider mounted to water hydraulic cylinder

As previously alluded to, a servohydraulic system is used to control the compression and expansion rates of this facility. A servovalve (MTS model #252.25) is connected to the oil-hydraulic cylinder. For a constant upstream oil pressure, the flowrate of water into the liquid piston is a function of the pressure in the compression/expansion chamber and the command to the servovalve. A series of experiments were conducted to fully map this behavior. This mapping is used to provide feed forward control of the compression/ expansion flowrate. In addition, the difference between the measured air volume and an air volume trajectory is used as the error signal for a proportional-integral controller.

All instrumentation, with the exception of the encoder, is connected to the PC via a Measurement Computing PCI-DAS 1602/16 data acquisition board. This board provides 16 bit resolution digitization of the thermocouple and pressure transducer signals. It also provides the analog control signal to the servovalve. The encoder is connected to the PC via a separate data acquisition board, Measurement Computing PCI-QUA04. Using a separate board allows a high resolution encoder to be used with fast flowrates without

having to increase sampling time. Both data acquisition boards interface with MATLAB/Simulink via xPC target. For all but the very slow tests, the sampling time is set to 1ms and data are recorded for up to 200s. For the very slow tests the sampling rate was decreased to 3ms so that data could be recorded for as long as 600s.

2.4 Limits of the Facility

The most significant limit on this facility is the pressure-dependent limit on flow rate. When the pressure in the compression chamber is high, the compression rate is limited. Compression rates as high as 1000 cc/s are possible when the compression pressure is low, but as the pressure rises near the end of the process, this slows. At 100 bar, the maximum compression rate is approximately 600 cc/s and at 200 bar the maximum rate is approximately 200 cc/s. For the experiments presented in this thesis, the maximum "constant" compression rate cases considered were 800 cc/s. When the compression rate is plotted vs. time, this deceleration is hardly noticed because pressure rises so fast near the end of compression.

This facility is capable of very slow compressions and expansions, even slower than 5 cc/s; however, the longest compression time considered was 430s and the longest expansion time was 414s. There was concern that at much longer compression or expansion times, the impact of leakage and the dissolution of air into the liquid piston would no longer be negligible.

The maximum allowable system pressure was 210 bar.

During these experiments, air temperatures as high as 650 K and as low as 120 K were inferred. These extreme temperatures were considered in the design phase of the

facility. As shown in [27], the o-rings that seal the compression/ expansion chamber sit in o-ring groves between the cylinder and top cap. Because of the high thermal capacitance of the region, these grooves stay at near ambient temperature and allow standard Buna-N o-rings to be used. Likewise, the pressure transducer is protected from extreme temperatures because most of the transducer is threaded in the top cap.

2.5 Porous Media Heat Transfer Elements

Several geometries and materials were considered for use in these experiments. Parameters considered included pore size, material conductivity, specific surface area, anticipated water hold up, pressure drop through the medium, anticipated heat transfer coefficient, cost, water compatibility and commercial availability. In previous experiments, continuous mini-tubes, metal meshes [22], interrupted plate geometries and metal foams [26] [27] were considered.

In this study interrupted plates, metal foams, and interrupted honeycomb geometries were considered. Four different materials were considered: aluminum, copper, stainless steel, and ABS plastic. Table 1 shows a comparison of the different combinations considered.

Insert Considered	Material	Spec. Surface Area (m^{-1})	Porosity	D_h (mm)	L/D_h	Critical h, Bi=0.1 ($W/m^2 K$)	Total Heat Capacity (J/K per CC)
1/16 Honeycomb	Al	2520	94%	1.5	4.27	6.1E+5	0.16
40 PPI Foam	Al	1654	93%	0.6	N/A	4.8E+5	0.17
1/8 Honeycomb	Al	1260	94%	3.0	2.14	4.0E+5	0.16
10 PPI Foam	Al	708	93%	2.5	N/A	2.1E+5	0.17
1/4 Honeycomb	Al	630	96%	6.1	1.04	3.0E+5	0.10
2.5 mm plates	SS	655	76%	5.0	1.50	4324	0.97
2.5 mm plates	Cu	655	76%	5.0	1.50	1.1E+5	0.87
2.5 mm plates	Al	655	76%	5.0	1.50	5.5E+4	0.59
2.5 mm plates	ABS	655	76%	5.0	1.50	46	0.50
5 mm plates	ABS	377	86%	10.0	0.75	46	0.29

Table 1: Comparison of Porous Media

It is desirable that the porous medium have a high specific surface area to facilitate heat transfer. As seen in Table 1, the inserts with the highest specific surface are the fine featured aluminum honeycombs and foams.

It is also desirable that the porous medium have enough thermal capacitance to avoid a large temperature change of the medium during the compression or expansion process. All of the interrupted plate geometries have a high heat capacity because of their relatively lower porosity.

Ultimately, the stainless steel and plastic 2.5mm interrupted plates were selected for this study. This geometry has been studied extensively in [24], as discussed in the literature review, and provides a good balance of surface area and heat capacity. Additionally, the 2.5 mm interrupted plate geometry tends to have less water hold up than aluminum foams and honeycomb. Reference [27] found the water holdup in a similar

2.5mm interrupted plate geometry to be equal to 7-8% of pore volume as compared to 90% of pore volume for a 40 pore per inch aluminum foam and 60% of pore volume for a 10 pore per inch aluminum foam. In simple submersion tests, this author found the water holdup in 1/16th inch cell size aluminum honeycomb to be approximately 65% of pore volume. Finally, there was some consideration for the cost of fabricating these inserts. The stainless interrupted plate geometry was manufactured at a reasonable cost using a wire electric discharge machining (EDM) process. Other options, such as casting, traditional machining, and plate joining with welding or brazing were either impractical or expensive. The plastic parts were produced using a 3D PolyJet printer.

2.6 Description and Purpose of Water Holdup Facility

A secondary facility was built for the specific task of measuring water hold up in the various porous media. The facility consists of a test section with the same inner diameter as the compression/expansion chamber, 76 mm. The length of the test section is 55 mm. A picture of this facility is shown in Fig. 2.6.1. Below the test section is a 12.7 mm (0.50") inner diameter graduated tube made from clear PVC. The tube is oriented vertically and is initially partially filled with water. The base of this graduated tube is connected to a piston-and-cylinder arrangement which is filled with water.

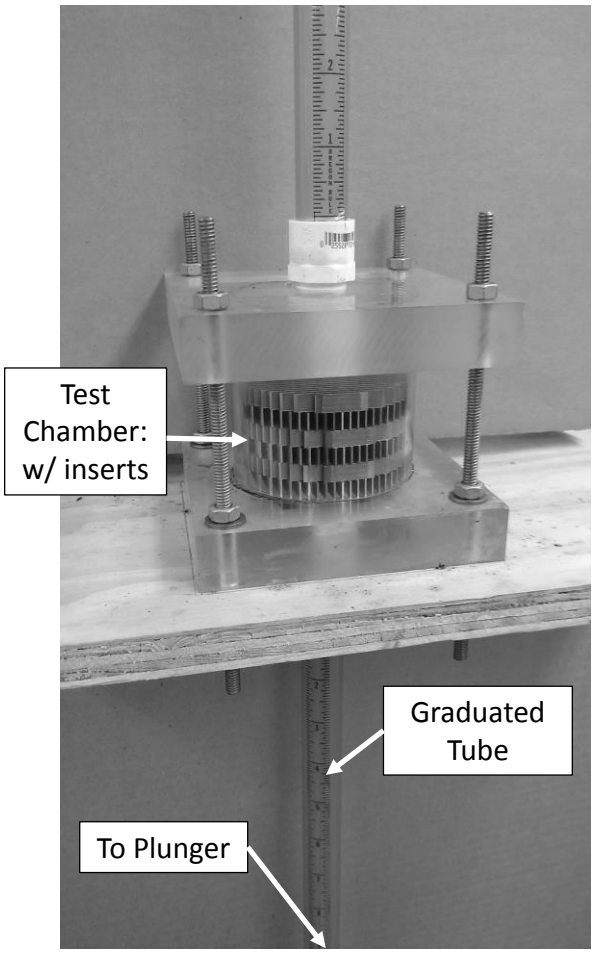

Fig. 2.6.1: Picture of water holdup facility

This facility simulates the conditions that a given porous medium sample would be exposed to in a liquid piston compressor/expander. As the solid piston moves forward, it injects water into the graduated tube and the liquid piston rises at a constant velocity. After one full stroke, the piston is retracted and the liquid piston recedes through the porous medium. After this process, some residual water remains trapped in the porous medium. The difference between initial and final water levels in the graduated tube corresponds to the volume of water that is trapped in the porous medium. Figure 2.6.2 explains this process graphically.

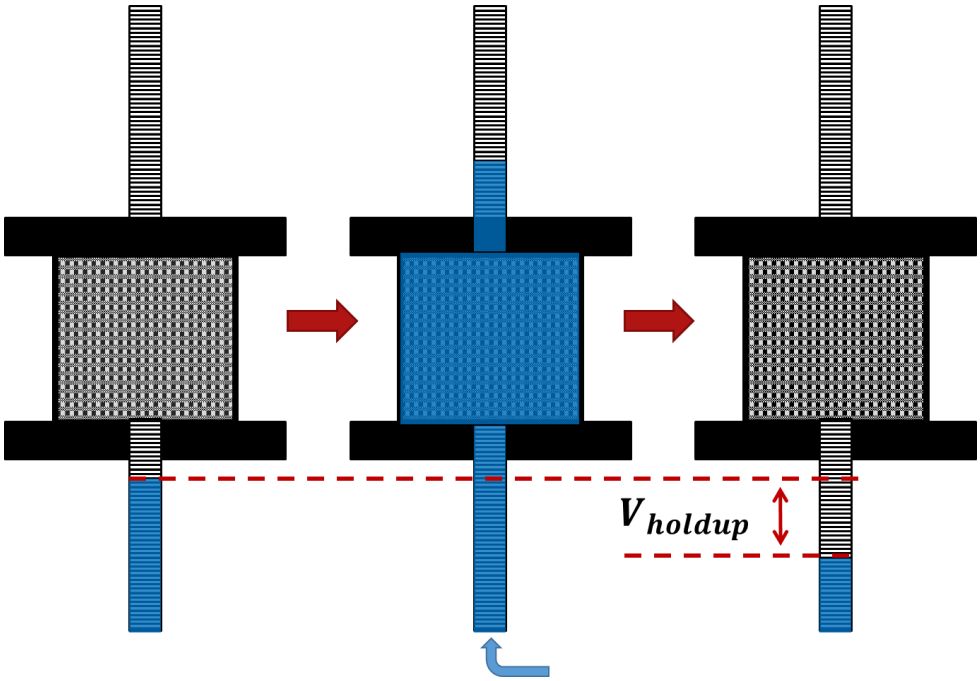

Fig. 2.6.2: Water holdup facility procedure

It is desirable that water holdup in a porous medium be minimal because a water-saturated porous medium will reduce the power density of the compressor/expander. This facility allows the water holdup in a porous medium sample to be measured with high resolution.

Chapter 3: Data Analysis

3.1 System Model and Assumptions

3.1.1 CAES Architecture and Liquid Piston Principles of Operation

In a liquid piston compressor/expander (see Fig. 3.1.1) a fixed volume chamber begins with some initial volume of gas and some initial volume of liquid. When liquid is added to the chamber the gas is compressed and the pressure rises; when liquid is removed from the chamber the gas expands and pressure falls. A functional air compressor/expander can be produced with the addition of valves and a storage tank.

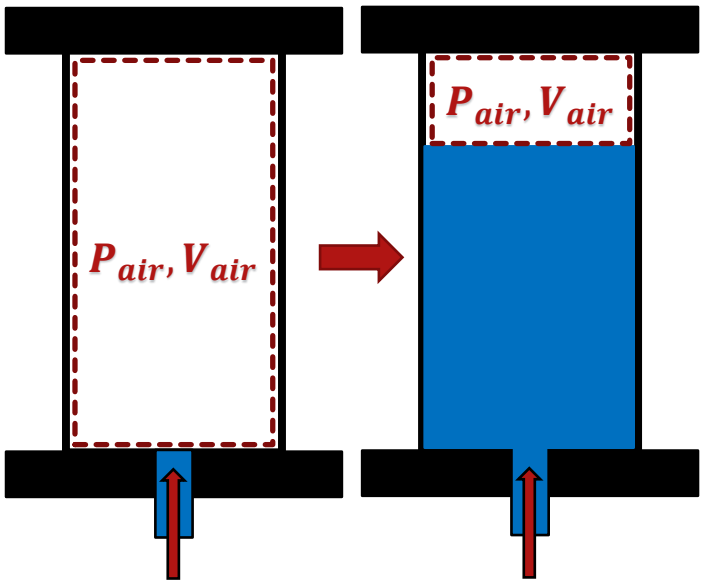

Fig. 3.1.1: Liquid piston – principle of operation

The concept of using a liquid piston for a compressed air energy storage system was introduced by Van de Ven and Li [29]. The authors found two key benefits from using a liquid piston. First, the liquid piston allows for an increase in the surface area to volume ratio of the compressor, which improves heat transfer and consequently, efficiency.

Second, the liquid piston eliminates gas leakage and the tradeoff between seal friction and gas leakage found in kinematic compressors. Third, a liquid piston can flow through a porous heat transfer matrix. Building off of this work, an architecture that integrated offshore wind turbines and compressed air energy storage was discussed in [6]. Figure 3.1.2 illustrates this architecture.

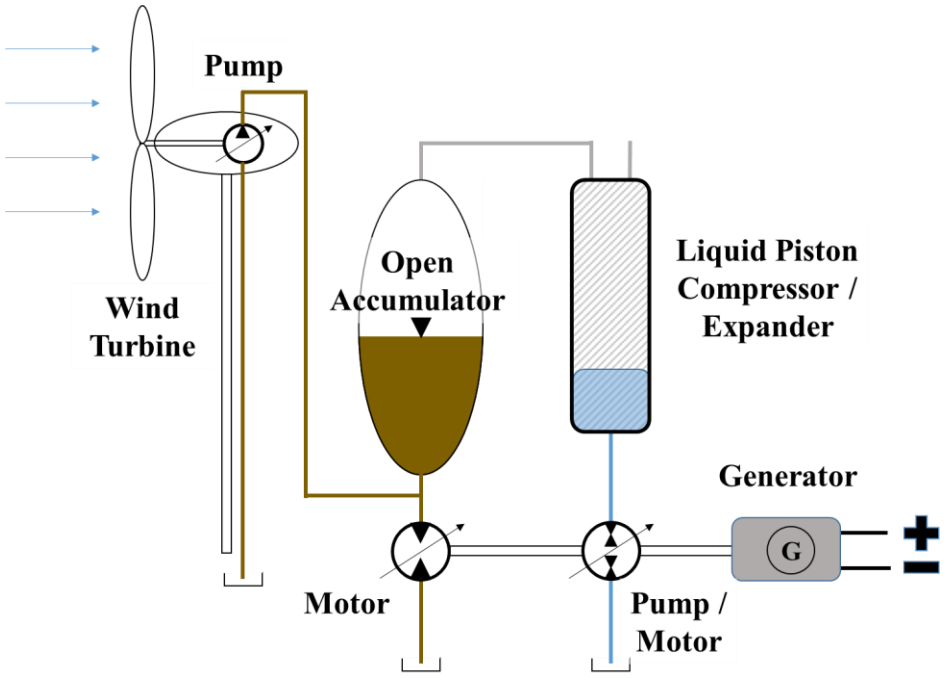

Fig. 3.1.2: Proposed CAES system: open-accumulator with liquid piston compressor/ expander

In this architecture, a hydraulic pump replaces the electric generator in the nacelle of the wind turbine. The pump is connected to a constant pressure open-accumulator and a hydraulic motor which powers both a liquid piston compressor/expander and an electric generator on a common shaft. The open-accumulator is regulated to approximately constant pressure, which allows the system to maintain a high power density. The generator is sized for the average power, rather than the peak power.

It is with this proposed system in mind that this thesis is written; however, this thesis seeks to evaluate the liquid piston compressor/ expander as a standalone component. Specifically, the experiments investigate the second stage compression and expansion processes, with a pressure ratio of 30 operating between nominal pressures of 7 and 210 bar. The source of the charge air, valving, and the source of flow for the liquid piston are not considered in the analysis. While these are important considerations for a real system, they are treated as ideal subsystems in this thesis.

3.1.2 Assumptions

As a model of the liquid piston compressor/ expander is developed several assumptions are made.

The first set of assumptions are thermodynamic assumptions. Both the compression and expansion processes are assumed to be quasi-static and reversible. All work done on the system is assumed to be PV work on a simple compressible substance.

The pressure field is assumed to be uniform. Pressure waves travel at the speed of sound. At 10 bar and 300 K the speed of sound is 348 m/s, three orders of magnitude higher than the fastest piston speed in these experiments. Compared to the relatively high pressure in the compression/expansion chamber, the difference in pressure created by gravity and the losses in porous media are negligible.

The compression/expansion chamber is assumed to be leak free and the air mass is assumed to be constant during compression or expansion. The liquid interface prevents leakage around the piston and the o-ring seals prevent a leakage from leaving the top of the chamber. The chamber was tested for leaks before any compression or expansion tests in a

hydrostatic pressure test. The cylinder was completely filled with water, brought to full pressure, and held at pressure overnight. During this time the pressure in the chamber was recorded. Over time the pressure in the chamber fell; the time rate of pressure change was found to be proportional to pressure. At the highest pressure, the rate was found to be 0.5 bar/min. The drop in pressure can be related to a loss in water volume using Eqn. (3.1) and assuming the water volume and bulk modulus of water to be constant.

$$\Delta V = -\frac{\Delta P}{K} V = \frac{0.5\ Bar/min}{22{,}000\ Bar} * 3L = 0.07\ mL/min \tag{3.1}$$

This leakage rate was deemed negligible since the final volume of air is approximately 70 mL.

The dissolution of air into water was also considered. Equation (3.2) is used to approximate the time for gas to propagate a distance, *x*, into the liquid.

$$t \cong \frac{x^2}{2D} \tag{3.2}$$

Taking *D* to be 2 x 10^{-5} cm^2/s, the diffusion time for the gas to propagate 1 mm is 250 s. As most of the experiments are less than 200 seconds, the dissolution effect was deemed negligible.

Air is not assumed to be an ideal gas in this analysis. The compressibility factor, Z, given by Eqn. (3.3) gives an indication of how far from ideal behavior a gas deviates. For an ideal gas Z=1. Table 2 lists values for Z for some of the experimental conditions encountered in this study. As shown in Table 2, values for Z deviate from unity. The deviation is particularly strong at high pressures and low temperatures, encountered in expansion. For this reason, Lemmon's real gas model for air is used [30].

$$\frac{P}{\rho RT} = Z \tag{3.3}$$

	Pressure, Bar								
Temp, K	**5**	**10**	**20**	**40**	**60**	**80**	**100**	**150**	**200**
120	0.94	0.87	0.67	0.18	0.26	0.34	0.41	0.60	0.77
160	0.97	0.95	0.90	0.78	0.66	0.57	0.55	0.63	0.76
200	0.99	0.98	0.95	0.91	0.87	0.84	0.81	0.81	0.85
250	1.00	0.99	0.98	0.97	0.95	0.95	0.94	0.95	0.97
300	1.00	1.00	1.00	0.99	0.99	0.99	0.99	1.01	1.03
400	1.00	1.00	1.00	1.01	1.02	1.02	1.03	1.05	1.08
500	1.00	1.00	1.01	1.02	1.02	1.03	1.04	1.07	1.09
600	1.00	1.00	1.01	1.02	1.03	1.03	1.04	1.07	1.09

Table 2: Compressibility factor for air at experimental conditions [31].

Finally, air is assumed to be a homogenous, thermodynamically pure substance. There are no chemical reactions at any point during the process.

Radiative heat transfer is ignored in these experiments. When calculating the convective heat transfer coefficient, heat flux is assumed to be uniform throughout the porous medium. For a uniform porous medium, the velocity field inside the gas is assumed to vary linearly from the liquid interface to the top cap. Thus, the average velocity for the gas is equal to half of the piston velocity. Computational studies of liquid piston compression support this assumption [25]. For non-uniform media, the gas velocity is assumed to vary linearly with respect to air volume. A lumped capacitance model is used for the porous medium and its temperature is assumed to be uniform in both axial and radial directions.

Losses in the delivery line to the liquid piston, and its valves, are not considered.

3.1.3 Governing Equations

The first law of thermodynamics for a closed system is used in the analysis of this system. The specific formulation used is shown in Eqn. (3.4).

$$dU = \delta W_{in} - \delta Q_{out} \tag{3.4}$$

Work is calculated directly from pressure and volume measurements. Internal energy and temperature values are found as functions of measured pressures and densities using the real gas relationship found in [30]. The ideal gas law is not used, as the air deviates from ideal behavior at high pressures. Once work and internal energy are known, Eqn. (3.4) is manipulated to solve for δQ. Equation (3.4) can be integrated with respect to time and the cumulative heat transfer, work, and internal energy change can be compared. It is also valid to differentiate with respect to time and compare rates.

At any instant during the process, the total surface area, the total heat transfer rate, and the bulk temperature of the gas are known. Assuming a uniform heat flux and a lumped capacitance model of the porous medium allows the temperature of the medium to be estimated. The driving temperature difference for heat transfer is assumed to be the difference between the bulk air temperature and the bulk porous medium temperature. With these assumptions, a zero-dimensional heat transfer coefficient, h, can be found using Eqn. (3.5).

$$h = \frac{\dot{Q}}{A\,\Delta T} \tag{3.5}$$

Where $\dot{Q}$ is the instantaneous heat transfer rate, A is the instantaneous surface area, and ΔT is the temperature difference between the air and the porous medium.

3.1.4 Figures of Merit

The system performance is characterized by: compression/expansion efficiency, compression/expansion time, maximum temperature change, mean power density, power per unit area, and bulk heat transfer coefficient. Each of these figures of merit will be discussed in more detail below.

When considering efficiency, it is helpful to think of an ideal thermodynamic cycle. The ideal compression and expansion cycles can be summarized in four steps:

1) Isobaric filling of the chamber at initial pressure
2) Isothermal compression or expansion of the gas
3) Isobaric ejection of air from the chamber at final pressure
4) Isochoric return to initial pressure at 0 volume

Figure 3.1.3 illustrates this graphically.

A real system will deviate from this ideal behavior. The actual compression or expansion process will not be truly isothermal. The intake and ejection processes may not be truly isobaric, this depends on the valves that are used. Finally, the real compressor/expander will likely have a small amount of dead volume, which will prevent the isochoric return from final pressure to initial pressure (step 4). The real efficiency for a compression cycle would be the ratio of the area enclosed by the ideal compression curve to the area enclosed by the actual compression curve. Likewise, the real expansion efficiency would be the ratio of the area enclosed by the real expansion curve to the area enclosed by the ideal expansion curve.

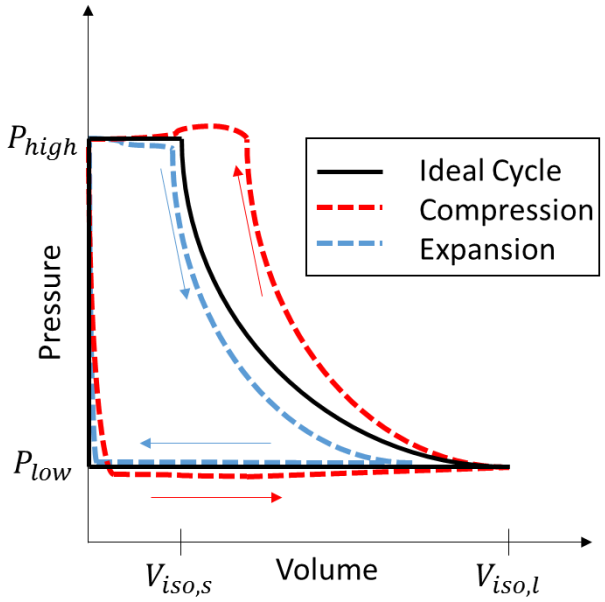

Fig. 3.1.3: Real and ideal compression and expansion in CAES system

For these experiments a different definition for efficiency is introduced. For this new definition only the portion of the cycle occurring during the compression or expansion process is considered. The isobaric filling and ejection work are not included. The definitions for compression and expansion efficiency are described by Eqn. (3.6) and (3.7), respectively, and illustrated in Fig. 3.1.4. These definitions provide a more conservative definition for efficiency than if the high pressure ejection work was included in both the numerator and denominator of Eqn. (3.6) and (3.7).

$$\eta_{comp} = \frac{-\oint_{P_{low}}^{P_{high}} (PdV)_{isotherm} - P_{low}(V_{iso,l} - V_{iso,s})}{-\int_{P_{low}}^{P_{high}} PdV + P_{high}(V_f - V_{iso,s}) - P_{low}(V_{iso,l} - V_{iso,s})} \tag{3.6}$$

$$\eta_{exp} = \frac{\int_{P_{high}}^{P_{low}} PdV - P_{low}(V_f - V_{0,e})}{\oint_{P_{high}}^{P_{low}} (PdV)_{isotherm} - P_{low}(V_{iso,l} - V_{iso,s})} \tag{3.7}$$

where P_{high}, P_{low}, $V_{iso,l}$, and $V_{iso,s}$ are the pressure and volumes shown in Fig. 3.1.3,V_f is the final volume for a compression or expansion process, and $V_{0,e}$ is the initial volume of

the expansion process and is equal to $V_{iso,s}$. The numerator of Eqn. (3.6) is the area under the isothermal curve, less the low pressure work. The denominator of Eqn. (3.6) is the area under the actual pressure-volume curve, less the low pressure work, plus the amount of work required to maintain pressure at P_{high} as the gas cools to ambient. The numerator from Eqn. (3.6) is the denominator in Eqn. (3.7); it is the amount of energy that is recoverable. The numerator of Eqn. (3.7) is the area under the actual process curve, less the low pressure work.

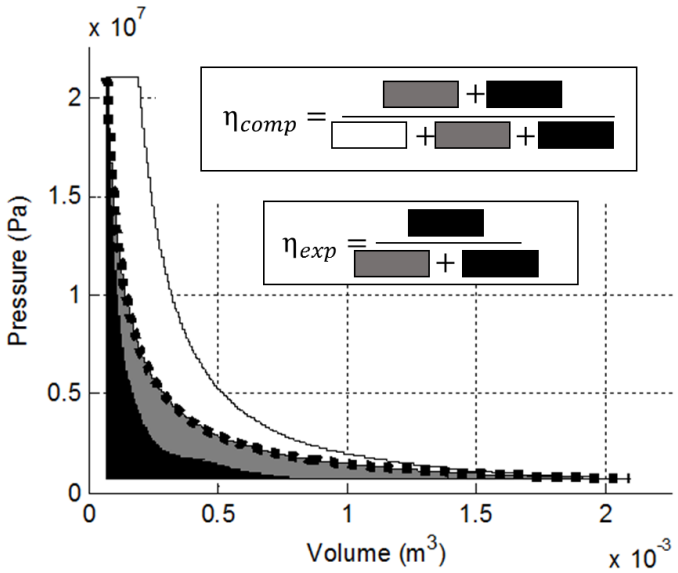

Fig. 3.1.4: Compression and expansion efficiency expressed graphically. Dimensions are for typical pressures and volumes encountered in experiments.

With these definitions, only the compression/expansion process is considered. For an isothermal compression or expansion, the efficiency is 100%. For an adiabatic compression with a pressure ratio of 30 the efficiency is 49%; for an adiabatic expansion with the same pressure ratio the efficiency is 43%. Although not added in these tests, inclusion of the injection/ejection process serves to increase efficiency. The full cycle efficiency can be approximated by adding the ejection work term to the numerator and

denominator of Eqn. (3.6) and (3.7). This term is given by Eqn. (3.8), and is calculated for all experiments in Appendix B. Compression and expansion efficiencies that include ejection work are given by Eqns. (3.9) and (3.10), where W_{iso} is the isothermal portion from Eqns. (3.6) and (3.7). Figure 3.1.5 shows the increase in efficiency that the ejection work provides based on typical values from baseline experiments. The values for W_{ejec} and W_{iso} will change with air volume, but the ratio of ejection work to isothermal work should remain constant, provided the pressure ratio remains constant.

$$W_{ejec} = (P_{high} - P_{low})\, V_{iso,s} \tag{3.8}$$

$$\eta_{comp,ejec} = \frac{1 + {W_{ejec}}/{W_{iso}}}{\eta_{comp}^{-1} + {W_{ejec}}/{W_{iso}}} \tag{3.9}$$

$$\eta_{exp,ejec} = \frac{\eta_{exp} + {W_{ejec}}/{W_{iso}}}{1 + {W_{ejec}}/{W_{iso}}} \tag{3.10}$$

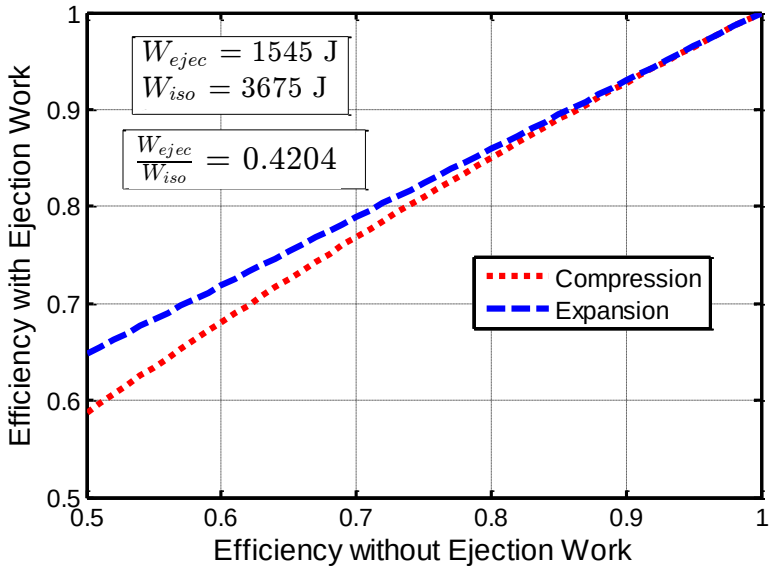

Fig. 3.1.5: Efficiency considering ejection work (Eqns. (3.9) and (3.10)) vs. efficiency without ejection work (Eqns. (3.6) and (3.7)). Textboxes provide information typical of baseline experiments with a pressure ratio of 30.

A second figure of merit is the total compression or expansion time, i.e. the total time it takes to complete the process. All else being equal, it is desirable that the process be fast so as to increase the power or power density. Power density is important because it is closely related to the cost and compactness of a compressor/ expander. If two equally sized compressors have the same thermal efficiency, the compressor that can operate at a faster rate it is more valuable. Likewise, if two compressors of different size store the same amount of energy at the same rate and efficiency, the smaller compressor will be preferred because it will be lower in cost

To achieve high efficiency it is desirable that the compression or expansion process be as close to isothermal as possible. One figure of merit used to characterize this is the maximum temperature change. This is simply the difference between the maximum or minimum temperature during the process and the initial temperature.

Mean power density is defined as the energy stored or recovered during a process, divided by the total time it took to complete the process, divided by the chamber volume. The definition of power density is given by Eqn. (3.11) for compression and Eqn. (3.12) for expansion. As previously discussed, a compressor/ expander that can operate efficiently at a high power density is desirable because power dense equipment is smaller, lighter, and lower in cost. An area-normalized power density can be introduced as well, by dividing power density by the specific area, given by Eqn. (3.13). The discussion of this term will resume later in this thesis when it is discussed in the context of experimental results.

$$\rho_{stor} = \frac{-\oint_{P_{low}}^{P_{high}} (PdV)_{isotherm} - P_{low}(V_{iso,l} - V_{iso,s})}{t\,(V_0 + V_{ins})} \tag{3.11}$$

$$\rho_{rec} = \frac{\int_{P_{high}}^{P_{low}} PdV - P_{low}(V_f - V_{0,e})}{t\,(V_f + V_{ins})} \tag{3.12}$$

where t is the compression or expansion time and V_{ins} is the volume of the insert. In both cases, the numerator for power density is the same as the numerator for efficiency.

$$PPA = \frac{\rho_{stor/rec}}{a} = \frac{E}{t\,V_{cham}} \frac{V_{cham}}{A} = \frac{E}{t\,A} \tag{3.13}$$

where $\rho_{stor/rec}$ is the stored or recovered power density, a is the power-weighted average specific surface area, E is the numerator of power density and efficiency, and V_{cham} is the total volume of the chamber including air and inserts, and A is total surface area.

A zero-dimensional bulk heat transfer coefficient has been introduced and defined in Eqn. (3.6). This heat transfer coefficient will be compared with CFD correlations for quasi-steady heat transfer in chapter 6.

3.2 Uncertainty Analysis

Pressure and volume of water added to the liquid piston are measured directly in these experiments and since the mass is assumed to be constant, the density can be calculated. The initial volume is measured with a 2000 mL volumetric flask and a 25 mL burette. The initial and final temperatures at thermodynamic equilibrium are measured with a thermocouple. During the compression or expansion process, temperature is calculated as a function measured pressure and density. A summary of uncertainty in the measured values is listed in Table 3.

Measurement	Instrument	Uncertainty	
P_0	Kulite XTL-123CEG-190-100SG	0.03	Bar
V_0	Volumetric Flask & Burette	0.6	mL
T_0	Type K Thermocouple	2.2	K
P(t)	Kulite XTL-123B-190-3000SG	0.2	Bar
$V_{add}(t)$	Magnetic Linear Encoder v1.2	0.4	mL

Table 3: Uncertainty in Measurements

For an ideal system with perfectly rigid plumbing and compression chamber, a perfectly incompressible liquid piston, and a perfect linear encoder the volume of air in the chamber would simply be found by subtracting the volume of water added to the system from the initial volume of air using Eqn. (3.14):

$$V_{air} = V_0 - V_{add} \tag{3.14}$$

In reality, Eqn. (3.14) fails to capture a number significant effects that impact experimental accuracy. The most significant effect that must be accounted is the compressibility of water. An additional complication is that the bulk modulus of water is not constant with respect to pressure and is dependent on the ratio of undissolved air to water [32]. An example is shown in Fig. 3.2.1.

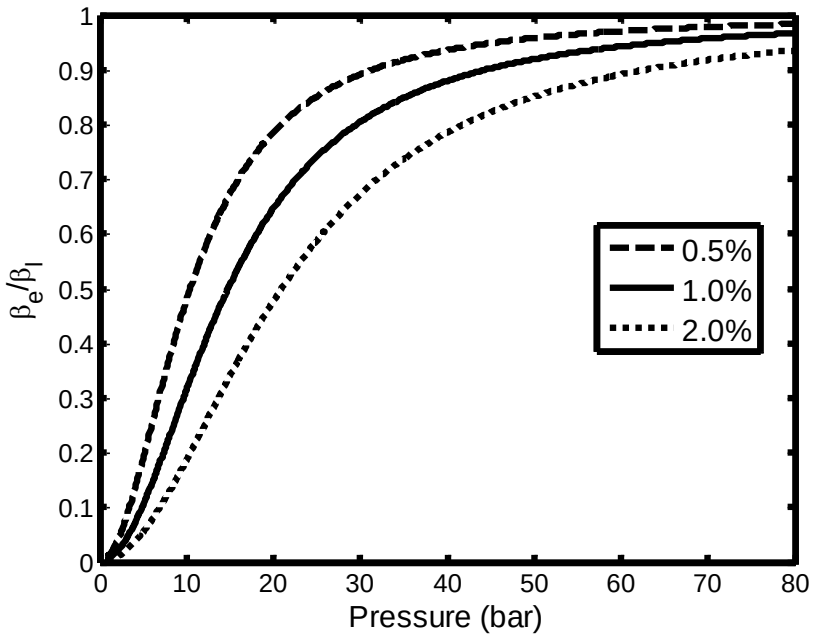

Fig. 3.2.1: Effective bulk modulus of water as a function of pressure and undissolved air (percent by initial volume).

To model this behavior, the water is assumed to consist of two independent phases: pure water with a constant bulk modulus of 2.2 GPa and a small volume of air bubbles that undergo isothermal compression. Combining this model with experimental measurements, the magnitude of this correction is approximately 25 cc at full pressure and normal experiment conditions.

Additional corrections are made for the volumetric expansion of the hoses and the compression/expansion chamber. The volumetric expansion in the chamber is found to be 2 cc/ 100 bar of pressure change by calculating the hoop strain and axial growth of the chamber. The volumetric expansion, or compliance of the hoses was measured using the experimental setup, with a slight modification. The hose was filled with water and capped at its connection point to the liquid piston compressor/ expander. The water hydraulic cylinder was used to increase the pressure in the hoses and the volume change was

measured with the linear encoder. Using the two phase compressibility model described above, some of the measured volumetric change was attributed to the compressibility of the water and entrained air in the system. This amount was subtracted from the measured pressure-volume curve, leaving the remaining 2.47 cc/ 100 bar of volumetric expansion to be attributed to hose compliance. This factor is in agreement with similar hydraulic hoses; however, the manufacturer of the hoses used in this experimental setup does not publish values for hose compliance.

A final volume correction is added to account for a slight deflection in the water hydraulic rod. This deflection is introduced by the high loads in the water hydraulic cylinder rod. The impact of this deflection increases with the rod extension length and the applied load. To account for this deflection, the hose compliance test is repeated for different rod arm extension lengths. An empirical correction for this deflection was found by fitting these experimental data with a best fit straight line. The magnitude of this final correction is the smallest, typically less than 1 cc in a normal experiment. When these additional terms are included, Eqn. (3.14) expands to Eqn. (3.15). After correcting for these effects, the total uncertainty in air volume at any point during the compression or expansion process is estimated to be ±2 cc.

$$V_{air} = \Big[V_0 - \Big\{ V_{add} + \frac{7.08\ CC}{100\ Bar}(P - P_0)(x) \Big\} + \frac{V_{wat}}{2.2\ GPa}(P - P_0) + \frac{-V_{0e}P_0}{P} + V_{0e} + \frac{2.47\ CC}{100\ Bar}(P - P_0) + \frac{2CC}{100\ Bar}(P - P_0) \Big] \qquad (3.15)$$

where:

- V_0 is the initial air volume in the compression chamber
- V_{add} is the volume added to the system as measured by the encoder
- x is the normalized extension of the rod, varying from 0 (fully retracted) to 1 (fully extended)
- V_{wat} is the total volume of water contained in the system
- V_{0e} is the initial volume of undissolved air in the water, at initial pressure, P_0
- P is the system pressure

Internal energy and temperature are functions of pressure and density. To estimate how errors in pressure and density affect internal energy and pressure, Eqns. (3.16) and (3.17) are evaluated at typical experimental values. Partial derivatives are calculated using a first order approximation over a small change (±0.5%) of the independent variables.

$$[\Delta T(P,\rho)]^2 = \left[\frac{\partial T}{\partial P}\Delta P\right]^2 + \left[\frac{\partial T}{\partial \rho}\Delta \rho\right]^2 \tag{3.16}$$

$$[\Delta u(P,\rho)]^2 = \left[\frac{\partial u}{\partial P}\Delta P\right]^2 + \left[\frac{\partial u}{\partial \rho}\Delta \rho\right]^2 \tag{3.17}$$

where Δ is used to indicate absolute uncertainty in a value.

A table of calculated results is shown in Table 4. The maximum uncertainty in temperature was found to be 10.2 K and occurs when the air has been compressed to a small volume. However, for most of the experiments the temperature error is 5K or lower. Similarly, the maximum error in specific internal energy occurs at high pressure when the volume is small. For most of the time the error in specific internal energy is approximately 2%.

Experimental Conditions		Error in Measurement		Errors as Percent in Measured and Calculated Values			
P (bar)	Rho (kg/m^3)	ΔP (bar)	Δρ (kg/m^3)	Measured Pressure	Measured Density	Temperature	Specific Internal Energy
200	236.0	0.21	6.55	0.1%	2.8%	1.8%	3.1%
200	225.0	0.21	5.99	0.1%	2.7%	3.4%	5.0%
200	100.0	0.21	1.42	0.1%	1.4%	1.6%	1.9%
100	157.0	0.21	3.07	0.2%	2.0%	1.1%	1.8%
100	116.9	0.21	1.83	0.2%	1.6%	1.3%	1.6%
100	60.0	0.21	0.68	0.2%	1.1%	1.2%	1.3%
50	100.5	0.21	1.43	0.4%	1.4%	0.8%	1.3%
50	58.6	0.21	0.65	0.4%	1.1%	1.3%	1.5%
50	36.0	0.21	0.36	0.4%	1.0%	1.0%	1.1%
20	52.0	0.21	0.56	1.1%	1.1%	1.0%	1.3%
20	23.3	0.21	0.22	1.1%	0.9%	1.6%	1.7%
20	17.9	0.21	0.17	1.1%	0.9%	1.3%	1.3%
10	29.5	0.21	0.29	2.1%	1.0%	2.0%	2.3%
10	11.6	0.21	0.11	2.1%	0.9%	2.2%	2.3%
10	10.4	0.21	0.09	2.1%	0.9%	2.2%	2.3%

Table 4: Uncertainty in calculated values: temperature and internal energy

Work input or output is found by integrating pressure with respect to volume. For a best case assumption, the errors in pressure and volume are stochastic and are eliminated in the integration. For a worst case assumption, the pressure or volume errors accumulate during the process. Using this worse case assumption, the error in work input or output is 1.6%. The real uncertainties in work input/output and efficiency, are somewhere between the best case scenario of 0% and the worst case scenario of 1.6%.

Cumulative heat transfer is found by taking the difference between the work term and the change in internal energy, as described in Eqn. (3.4). Thus, the uncertainty in cumulative heat transfer is the root sum square of uncertainty in the work term and the

uncertainty in internal energy. The error in cumulative heat transfer depends on the compression or expansion rate and whether or not porous media are used. The relative error in cumulative heat transfer is higher in cases with poor heat transfer and lower in cases with good heat transfer.

The trends in uncertainty of the calculated heat transfer rate, total surface area, and heat transfer coefficient are also considered. The instantaneous heat transfer rate depends on accurately calculating instantaneous power and the time rate of change of internal energy. At a given point in time, the certainty in measured values can be estimated, but the certainty in the time derivative values depends on the noise in the system and the degree of smoothing that is done in the post-processing calculation. This analysis used a moving window of ± 50 ms as a good middle ground of capturing all effects while removing noise from the system. Calculating the instantaneously available surface area is also challenging because it is difficult to characterize how water from the liquid piston affects surface area. Small water droplets on the interrupted plates, side walls, and top cap would serve to increase the total amount of surface area, while large droplets that fill pores would tend to reduce the total surface area. Finally, the calculation of h has the highest degree of uncertainty as it depends on the already uncertain values for instantaneous heat transfer rate, instantaneous surface area, and driving temperature difference.

Chapter 4: Tests Conducted

4.1 Water Holdup in Porous Media

The water holdup test facility as described in Chapter 2 was used to measure the water holdup in the porous media used in compression and expansion tests. Water holdup is simply defined as the volume of water that remains trapped within the pores of the medium after the liquid piston has receded from the medium.

The graduated tubes on the top and bottom of the test section were calibrated by adding water from a burette in 25 mL increments and recording the change in level height. Six readings were taken and the slope of the best fit line was found to be 4.75 mL/in. Water is added to the bottom of the facility with a piston and cylinder. This volume was found by measuring the change in mass of the water-filled cylinder between its fully retracted and fully extended positions. This volume was found to be 308 cc.

Each test begins with a completely dry test section. Next, 308 cc of water is added from the piston and cylinder and the piston is retracted. Even without a porous medium in the chamber, some residual water remains in the test section. The measurements of trapped water in the empty chamber are plotted in the first plot of Fig. 4.1.1

The plastic inserts and the stainless steel inserts (refer to Fig. 4.4.1) were tested in this facility. Because of the differences in manufacturing and material strength, the plastic inserts have an external ring for added strength. The bulk volume of inserts in each case was 199 cc. Results for the three cases are shown in Fig. 4.1.1.

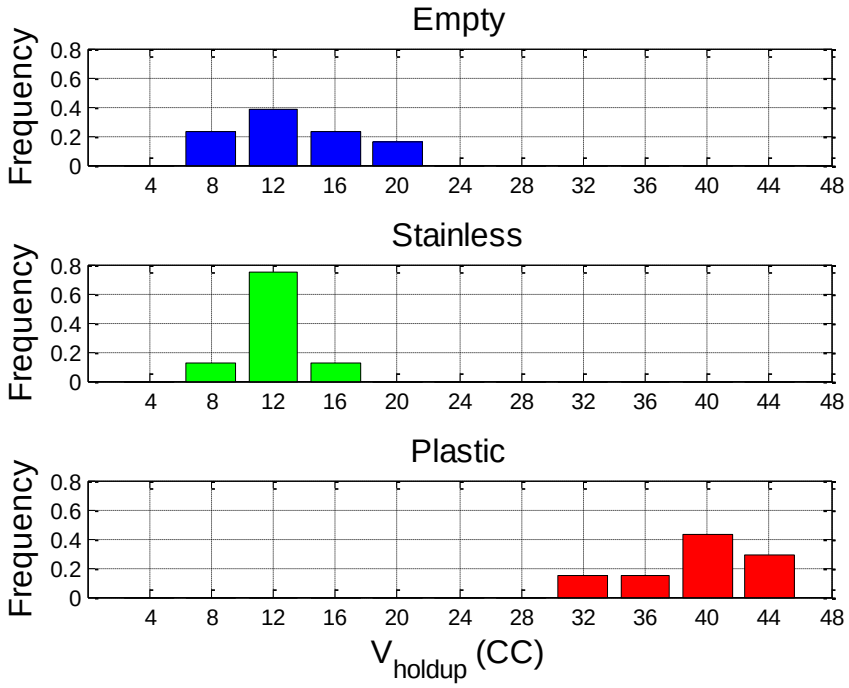

Fig. 4.1.1: Water hold up measurement probability distribution for empty test facility and two inserts.

There was observable variability in the measurements. For the empty chamber, the mean water holdup volume is 13.5 cc, with a standard deviation of 4.0 cc. For the stainless steel inserts, the mean water holdup volume is 12.7 cc with a standard deviation of 1.8 cc. For the plastic inserts, the mean water holdup volume is 39.6 cc with a standard deviation of 3.4 cc. The stainless steel inserts perform well and have very little water holdup, approximately the same as the empty case; however, the plastic inserts trap 3-4 times more water than the stainless inserts. Partnering with researchers at the University of Virginia, attempts were made to reduce the water hold up in the plastic inserts by applying a super hydrophobic coating to the insert. This coating, however, is still in the early stages of development and the pre-treatment process caused degradation to the insert sample.

Although super hydrophobic coatings have the potential to dramatically reduce water holdup, further discussion of them is beyond the scope of this work.

4.2 Calibration of Liquid Piston Compressor/ Expander

Prior to beginning the testing program, pressure transducers were calibrated against a deadweight tester. The new calibration was compared to the original manufacturer's calibration and the change in calibration was negligible, suggesting stability of the instrument.

The linear magnetic encoder can read a linear displacement with a resolution of 15 μm and an accuracy of 45 μm. This linear displacement must be related to a volume of water ejected from the cylinder. To calibrate the encoder, an appropriate plumbing configuration was used which enabled the water hydraulic cylinder to intake and eject water at atmospheric pressure. Water was ejected from the water hydraulic cylinder to nearly fill a 2000 mL volumetric flask. A burette was used to fill the remainder of the volumetric flask to precisely 2000 mL, allowing the volume of water ejected from the cylinder to be known with high precision. The volume and the encoder reading were correlated with a conversion factor that related the reading from the encoder to the ejected volume. This measurement was repeatable to within 1 mL at 2000 mL.

The flow rate of oil into the oil hydraulic cylinder, and hence the flow rate of water into the compression chamber, depends on the electric current sent to the servovalve, the supply pressure of the hydraulic system and the back pressure in the compression/ expansion chamber. In order to better control the flow rate during experiments, an effort was made to characterize the interaction of these variables. First, several flow rate

measurements were taken with constant servovalve commands (voltages varying from -5V to 5V) and with the chamber pressure held constant at atmospheric pressure. For small magnitude servovalve commands at constant pressure, the flow response is linear due to an internal feedback loop in the servovalve. As the magnitude of the servovalve command increases, the flow rate response saturates as the spool in the servovalve can no longer increase internal orifice area. The flow rate also decreases as back pressure in the compression chamber increases. By measuring the flow rate at different back pressures and different voltage commands to the servovalve, the map shown in Fig. 4.2.1 was created. Using this map, the voltage command to the servovalve is selected as a function of measured pressure in the compression/ expansion chamber and desired flow rate.

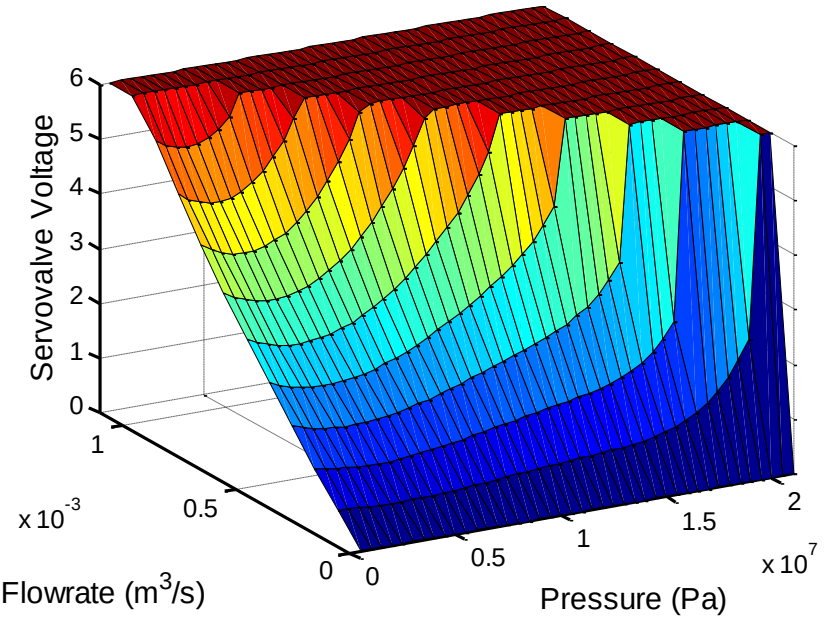

Fig. 4.2.1: Map of servovalve command for a desired flowrate at a given pressure

4.3 Baseline Tests

Tests with no porous medium are performed to establish a baseline to compare to all other tests. All baseline tests begin with the liquid piston level at the bottom of the chamber. The initial air volume is known, the initial temperature and pressure are measured. No porous inserts are placed in the compressor/expander.

Once the data acquisition system begins logging data, the experiment is manually put into "compression mode" in the Simulink control program. A combination of proportional-integral (PI) and feed forward control are used to track a defined volume trajectory. For the baseline cases, the volume varies linearly in time. Once a pressure of 210 bar has been reached, the experiment automatically switches from "compression mode" to a proportional-integral controller that maintains the pressure at 210 bar as the compressed gas cools. Once the gas has come into thermal equilibrium with the ambient temperature, a manual switch is used to put the experiment into "expansion mode." As in compression, feed forward and PI control are used to track the desired volume-time trajectory.

When post-processing the raw data, each experiment is split into two sets of data: compression from initial pressure to a pressure ratio of 30 and expansion from 210 bar to 7 bar. In both compression and expansion, the pressure ratio is 30. Compression tests were done at constant compression rates of: 5, 10, 12, 20, 50, 100, 200, 400, 600, and 800 cc/s which resulted in compression times of 2.7 to 438 s. Expansion tests were done at constant rates of 5, 10, 20, 50, 100, 200, 300, 500, 800, and 900 cc/s which resulted in expansion times of 0.9 s to 414 s.

4.4 Tests with Uniform Distributions of Porous Media

Tests with uniformly distributed porous media are conducted to evaluate the improvement in power density and efficiency that porous media offers. In many ways, the tests with the uniform distribution are like the baseline tests. As in the baseline cases, a linear volume-time trajectory is tracked with PI and feed forward control. The presence of porous media however reduces the initial air volume. Additionally, for the same compression or expansion rate, the piston velocity is faster because the cross-sectional area is reduced. Similar compression and expansion rates are used in the uniform distribution tests as in the baseline tests. Compression rates range from 12 to 800 cc/s, which correspond to compression times of 2.0 s to 129 s. Expansion rates range from 20 to 800 cc/s, which correspond to expansion times of 1.9 s to 73 s.

Unlike the baseline case, the compression chamber in these tests is filled with a uniform distribution of interrupted plate heat exchanger inserts. As discussed in Chapter 1, these plates have been used in previous computational and experimental investigations. Each plate is 7.5 mm tall and 0.8 mm thick. The plate separation distance is 2.5 mm. Two variations of this geometry are used. In the first variation, the plates are manufactured from a photopolymer called VeroWhite using a 3D printing process. To improve the strength of the porous insert, an outer ring was added to hold the plates in place. The second variation was manufactured from 316 stainless steel. These plates were manufactured using a wire EDM and the outer ring was not needed. The two different forms are shown in Fig. 4.4.1.

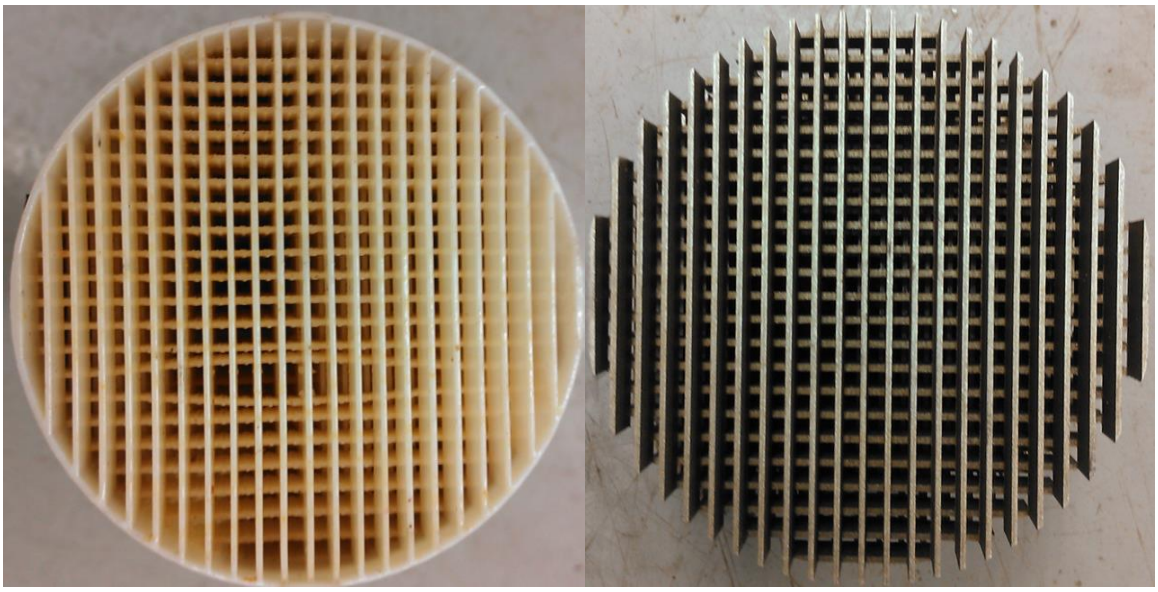

Fig. 4.4.1: Interrupted plate heat exchanger inserts. Left is made from photopolymer, right is made from 316 stainless steel.

The internal geometry of both forms is the same, so both were used in the uniform distribution experiments. The top 6 cm of the chamber is filled with the stainless steel inserts and the next 39 cm is filled with the plastic inserts. Because of the deflector that was installed to minimize jetting, the bottom 3 cm simply holds a spacer to hold the porous medium in place. Figure 4.4.2 shows the distribution in the upper portion of this distribution.

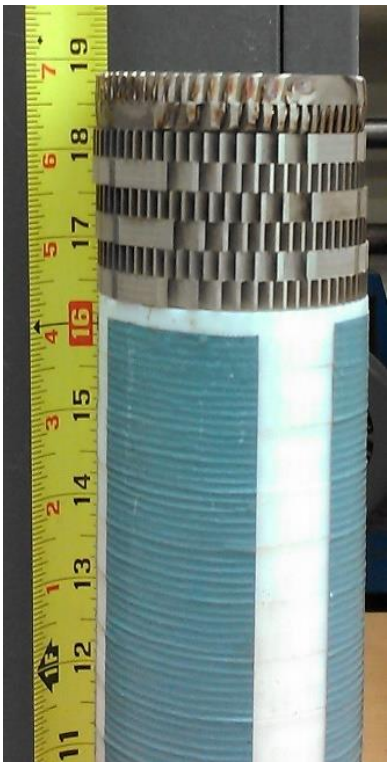

Fig. 4.4.2: Picture of top portion of uniform distribution. Tape measure shown for reference has units of inches. Stainless medium is only the top 6 cm (bottom section filled with plastic inserts, held in place with blue tape).

4.5 Tests with Non-Uniform Distributions of Porous Media

Five non-uniform porous media distributions are used to determine the optimal distribution for a given set of constraints. For all five distributions, the initial air volume and total insert surface area is fixed. A series of annular spacers of varying heights is used to locate the stainless steel interrupted plates at different locations inside of the compression/ expansion chamber (see Fig. 4.5.1). The combined height of all the spacers is 42.3 cm, so that the combined height of the spacers and inserts is 48.3 cm, the total height of the chamber. The annular spacers are made from aluminum and are approximately 6 mm thick. The outer diameters of the spacers were turned to fit snugly in the compression/ expansion chamber. The spacers are used to create five distributions, labeled "A" through "E" in Fig. 4.5.1. The

vertical locations of the interrupted plate inserts, expressed as a percentage are 14%, 72%, 86%, 97%, and 100% for distributions A, B, C, D, and E, respectively. When calculating power density, the spacers are treated as if they were part of the compression chamber wall, and not as additional porous media. For each distribution, four different constant compression/ expansion rates are used: 50 cc/s, 100 cc/s 200 cc/s and 500 cc/s.

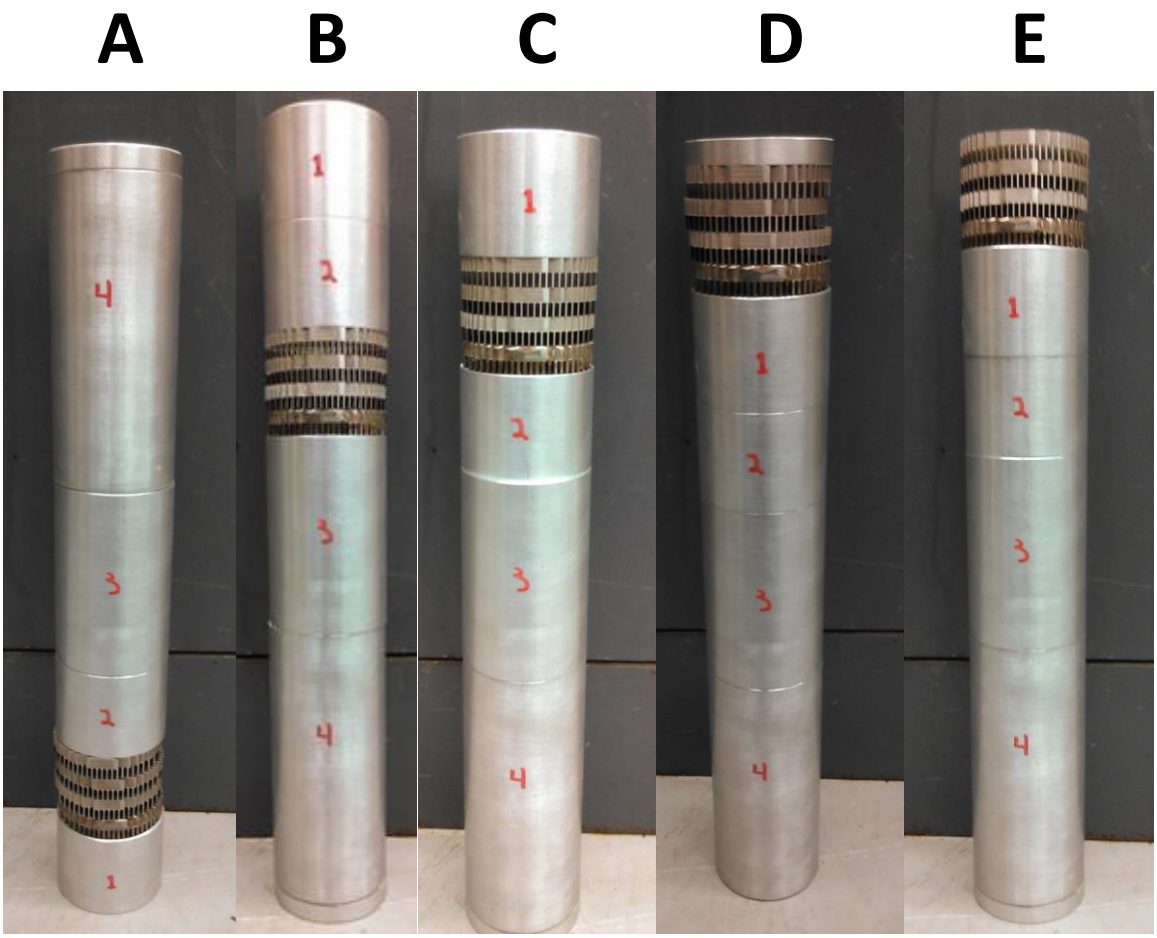

Fig. 4.5.1: Non-uniform distributions of 2.5 mm interrupted plate porous medium inserts and annulus-shaped aluminum spacers

4.6 Optimal Compression Rate Tests

Additional tests are designed to study the effect of an optimal compression profile. As discussed in Chapter 1, there have been several investigations to determine a compression profile that improves power density, efficiency, or both for given heat transfer conditions. A previous experimental effort tracked an optimal trajectory in a liquid piston compressor without additional porous media. However, it is possible to combine the benefits of porous media and an optimal trajectory. In order to make a good comparison, the uniform distribution of porous media as described in Chapter 4.4 is used as the reference.

To realize this, a one-dimensional optimization code will be written that models the compressor used in the experimental setup using real gas properties. This optimization will return an optimal compression temperature – volume trajectory for a specified efficiency. The experiment controller will be modified to track this temperature as a function of volume, rather than tracking volume as a function of time.

As of the writing of this thesis, this work has not been completed. The details of the optimization, the control methodology, and the experimental results will be presented in a subsequent publication.

Chapter 5: Results

5.1 Baseline Results

The compression rates for the baseline cases are shown in Fig. 5.1.1 and expansion cases are shown in Fig. 5.1.2. It should be noted that both the x and y axes are in log scale. In both figures the x-axis starts at 0.2s, as the flowrates have reached a constant condition at this point. For both compression and expansion cases, it is apparent that a wide range of experimental conditions have been achieved. For compression cases, compression times varied from approximately 2.5s to approximately 400s. Likewise, in expansion, the expansion times varied from approximately 1.4s to approximately 400s. Figures 5.1.3 and 5.1.4 show the ramp ups for compression or expansion cases that were plotted in figures 5.1.1 and 5.1.2.

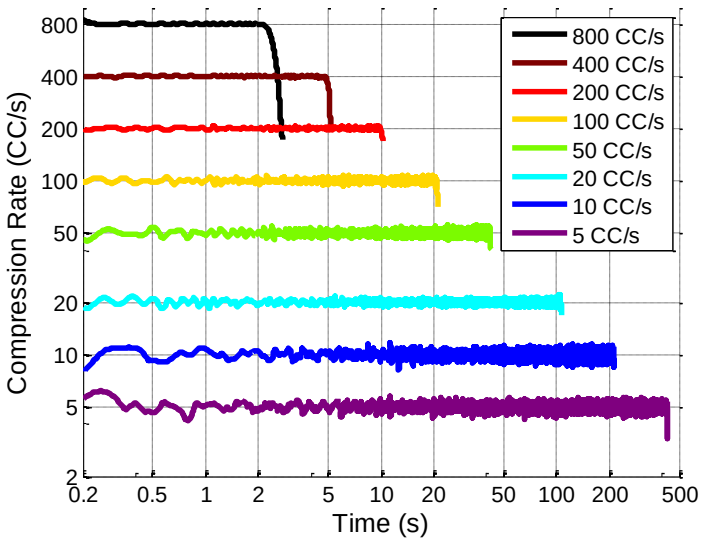

Fig. 5.1.1: Compression rates in cc/s plotted against compression time for the range of tests conducted. The legend denotes the target compression rate. Both axes are in log scale.

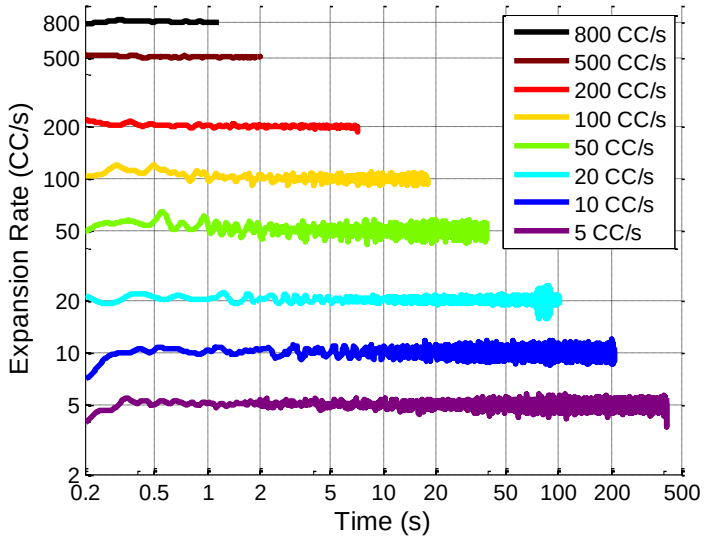

Fig. 5.1.2: Expansion rates in cc/s plotted against expansion time for the range of tests conducted. The legend denotes the target expansion rate. Both axes are in log scale.

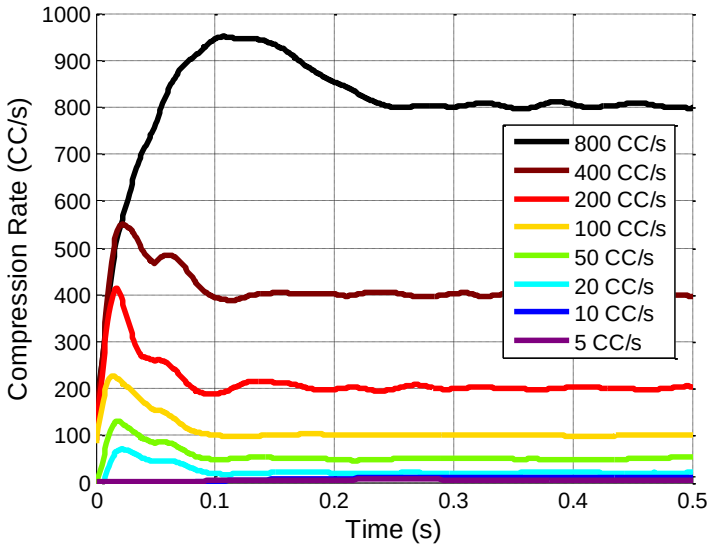

Fig. 5.1.3: Ramp up of compression rates

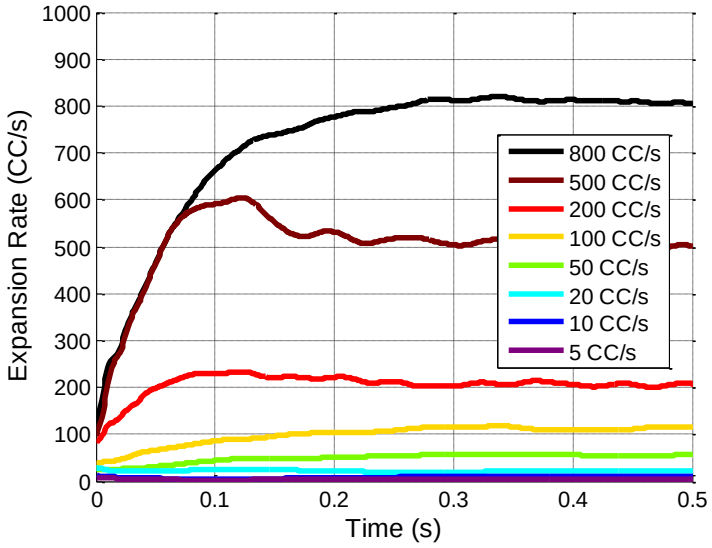

Fig. 5.1.4: Ramp up of expansion rates

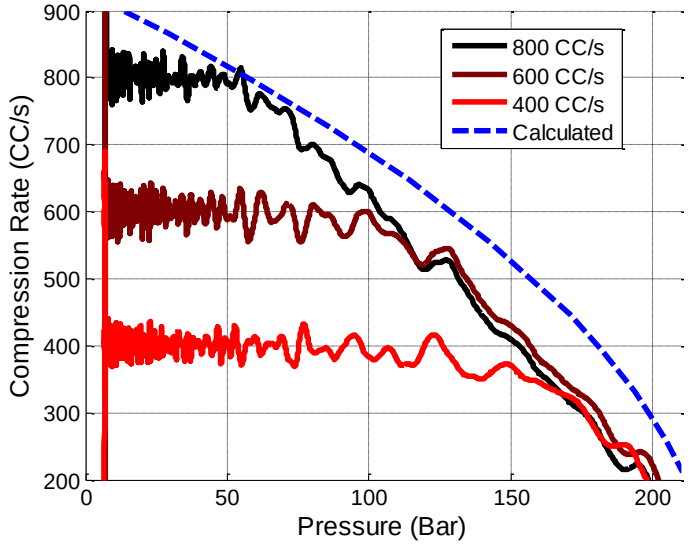

Fig. 5.1.5: Compression rate in cc/s plotted against pressure in Bar. The legend indicates the target compression rate. The dashed line shows the pressure-dependent limit of the flowrate.

As discussed in section 2.4, the compression rate is pressure limited. Figure 5.1.5 shows the theoretical flow limitation based on a simple servovalve model as well as three cases. The simple model assumes constant supply and tank pressure and that the only loss of pressure occurs across two servovalve orifices. This pressure limitation causes

compression rates that are faster than 200 cc/s to undergo some deceleration at the end of the compression process. This deceleration is negligible for cases slower than 200 cc/s. This effect is not as easily seen in the flow rate vs. time plots, (Fig. 5.1.1), because most of the compression (time) takes place at low pressure. Compression cases faster than 800 cc/s were not considered because of this deceleration. If a non-uniform compression rate is used, then the total compression time can be reduced by compressing at a fast rate at the beginning (low pressure) and slowing as pressure increases

The baseline pressure-volume curves are shown in Fig. 5.1.6 for compression and Fig. 5.1.8 for expansion. In both figures, the x and y axes are in log-scale. The theoretical limits of adiabatic and isothermal are also plotted for reference. In Fig. 5.1.8, the calculated adiabatic curve undergoes some non-ideal behavior as the temperature becomes very low. For both compression and expansion cases, experimental data cover most of the range between the two theoretical limits. For both compression and expansion, increasing the rate causes the process to become more adiabatic. In compression tests, increasing the compression rate changes the polytropic index (slope when plotted in log-scale) from near 1 (isothermal) to near 1.4 (adiabatic). For all baseline compression tests, the polytropic coefficients varied from 1.04 to 1.34. These coefficients are plotted against flow rate in Fig. 5.1.7 and discussed in greater detail in section 5.4 when compared with other tests and plotted in Fig. 5.4.7. Neither the adiabatic or isothermal extreme is reached, despite having tests with compression rates that differ by more than two orders of magnitude.

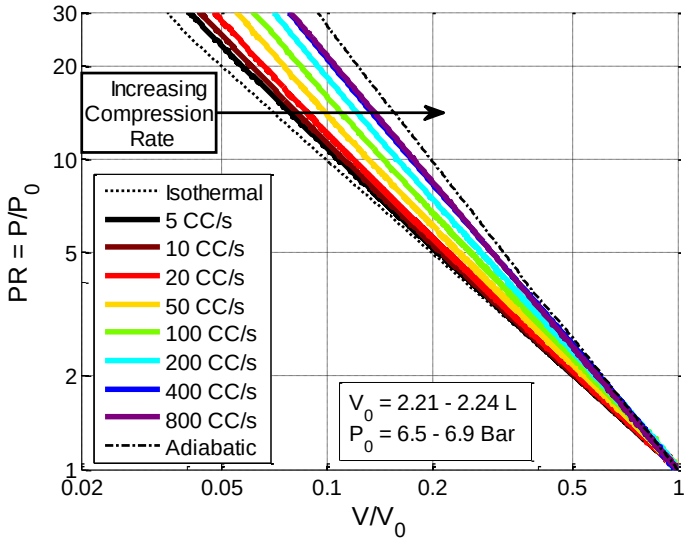

Fig. 5.1.6: Pressure-Volume curves for baseline compression cases. The legend indicates the constant compression rate used. Axes are in log scale. Pressure and volume have been normalized by initial conditions which are shown in the figure.

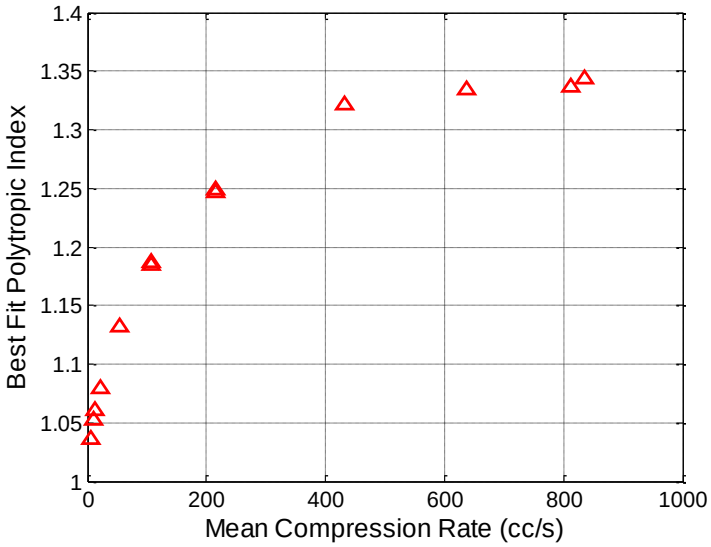

Fig. 5.1.7: Polytropic index for baseline compression cases plotted against compression rate

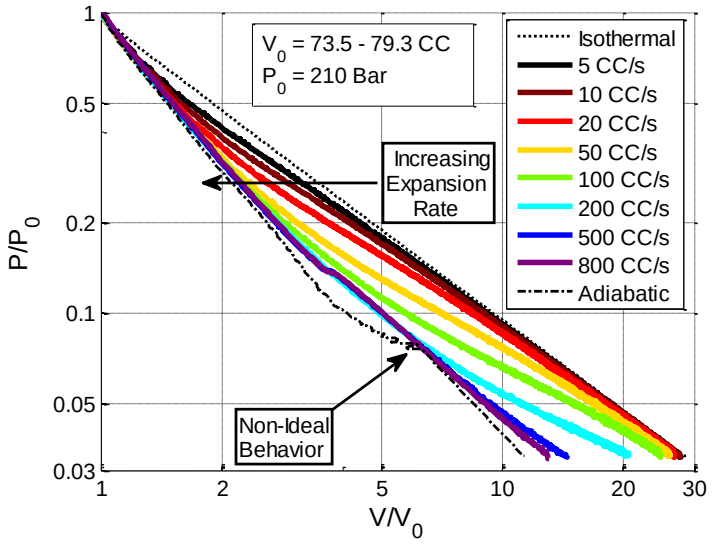

Fig. 5.1.8: Pressure-Volume curves for baseline expansion cases. The legend indicates the constant expansion rate used. Axes are in log scale. Pressure and volume have been normalized by initial conditions which are shown in the figure.

A different trend can be seen in the expansion cases. For the most part, the expansion data collapse at the onset of expansion. This initial portion of the process is near-adiabatic. During expansion, the process transitions from near-adiabatic to near-isothermal. Rather than affecting the polytropic index, increasing the expansion rate appears to change the point where the transition from near-adiabatic to near-isothermal begins. As the expansion rate increases, the process stays near-adiabatic longer. Because all of the baseline expansion tests exhibit this trend, no attempt was made to find a polytropic coefficient.

The temperature-volume curves for select compression cases are shown in Fig. 5.1.9; expansion cases are shown in Fig. 5.1.10. In both figures the final volume is smaller when the temperature is lower. This is because in each figure, the data are processed to the same final pressure (ratio), not the same volume. In the compression cases, the peak temperature always occurs at the end of compression. For expansion cases, the minimum temperature does not occur at the end of the process, but at some point before.

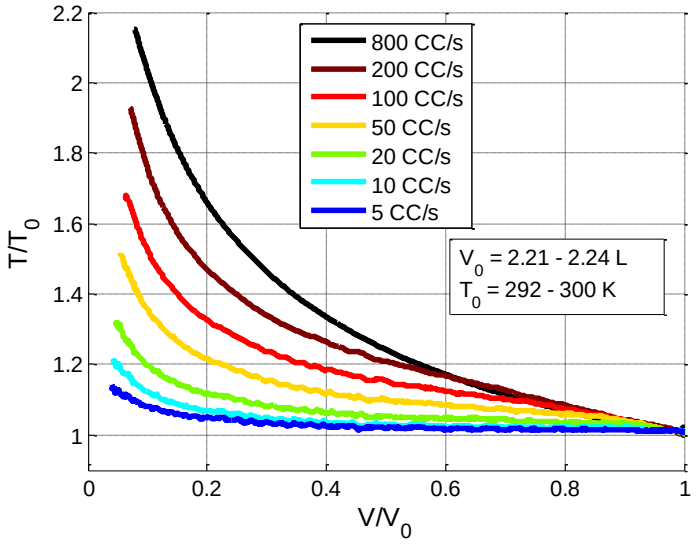

Fig. 5.1.9: Temperature plotted against volume for baseline compression cases. Temperature and volume have been normalized by initial values, which are shown in the figure. The legend indicates the constant compression rate used in the test.

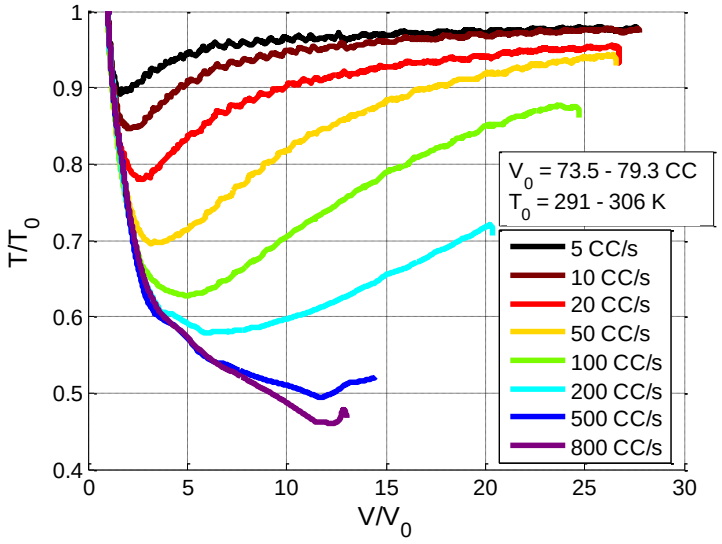

Fig. 5.1.10: Temperature plotted against volume for baseline expansion cases. Temperature and volume have been normalized by initial values, which are shown in the figure. The legend indicates the constant expansion rates used in the test.

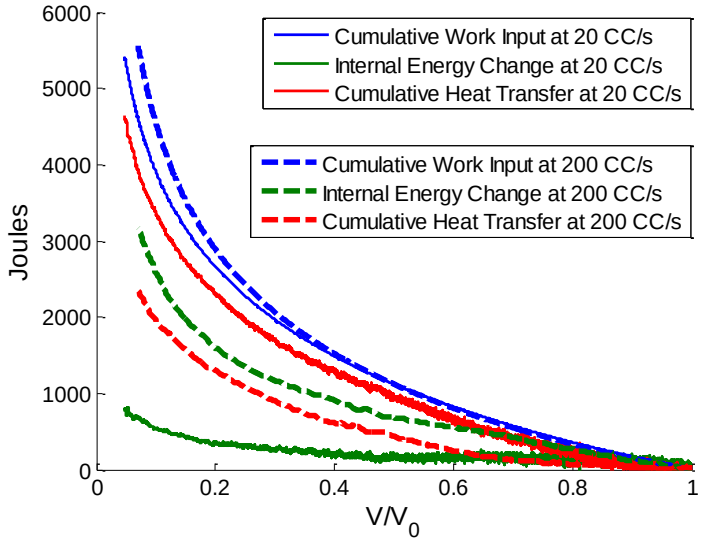

Fig. 5.1.11: Energy balance for two baseline compression tests at different compression rates. Legend indicates compression rate and energy form. Initial volume for both cases is 2.2 L.

Figure 5.1.11 shows the energy balance between cumulative work input, cumulative heat transfer out of the gas, and the net change in internal energy during two different compression cases. The two cases differ in compression rate by an order of magnitude: 20 cc/s and 200 cc/s. The initial volume for each case is 2.2 L. Comparing the two work input curves (blue), one observes that the final values for cumulative work input are approximately the same, but that the slower case has reached a smaller volume. Not shown in this figure is the additional work that is required to maintain a constant pressure as the gas cools to ambient temperature. Comparing the internal energy change of the two cases (green), one observes that the rise of internal energy in the slow case is approximately one fourth of the fast case. Internal energy rises due to the discrepancy between work input and heat transfer. In the slower compression, the cumulative heat transfer follows much more closely to the cumulative work input, compared to that of the fast case. Figure 5.1.11 does not provide us any time or rate information. Rate information is plotted in Fig. 5.1.13.

Figure 5.1.12 shows the energy balance between cumulative work input, cumulative heat transfer out of the gas, and the net change in internal energy during two different expansion cases. Since the gas is doing work on the surroundings and heat is being transferred into the gas, both cumulative work and heat transfer are negative, based on the sign convention used in this thesis. The two cases differ in expansion rate by a factor of 2: 50 cc/s and 100 cc/s. The initial volume for both cases is approximately 75 cc. Based on the temperature-volume data shown in Fig. 5.1.10, one would expect the internal energy to drop and then return to some value below its initial value. However, in Fig. 5.1.12 it is clear in both the fast and slow cases that the internal energy returns to some value above its initial value. This is counter-intuitive until one recalls that the non-ideal behavior of the gas causes internal energy to be a function of both pressure and temperature. The drop in pressure from 210 bar to 7 bar tends to increase the internal energy while the drop in temperature tends to decrease internal energy. In both expansion cases, the internal energy curve collapses to the cumulative work curve for the first portion of expansion. This is similar to the trends seen in the expansion P-V curves (Fig. 5.1.8) and the expansion T-V curves (Fig. 5.1.10). Comparing the cumulative work curves, one sees that the slower case was able to recover more energy during the expansion process. Also, the more slowly expanded gas has more potential to do work in the next stage of expansion, since it is not as cold as the more rapidly expanded gas.

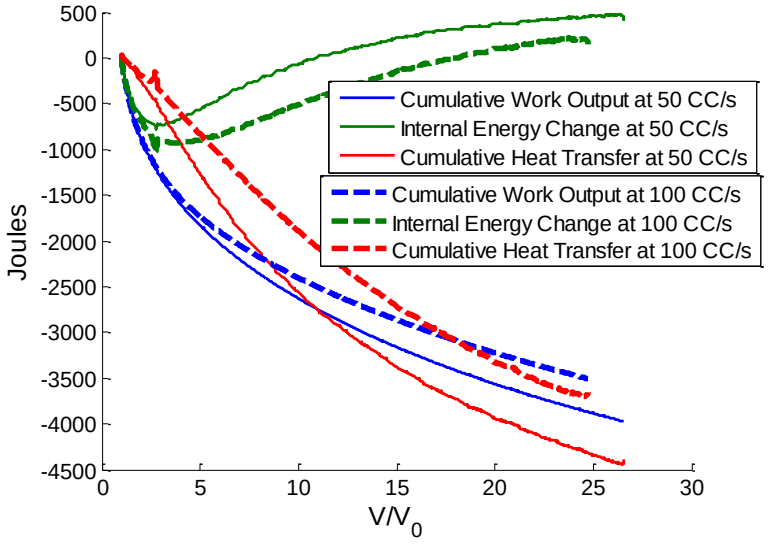

Fig. 5.1.12: Energy balance for two baseline expansion tests at different expansion rates. Legend indicates expansion rate and energy form. Initial volume for both cases is 75 CC.

Figure 5.1.13 compares the heat transfer rate and power for two baseline compression tests, one at 100 cc/s and one at 50 cc/s. Increasing the compression rate by a factor of two doubled the instantaneous power input at the same pressure and increased the instantaneous heat transfer rate by a factor of approximately 1.6. Even though heat transfer increases with compression rate because of an increase in average air velocity, it is not enough to compensate for the increase in power. This causes the internal energy to increase at a faster rate.

Figure 5.1.14 compares the heat transfer rate and power for two baseline expansion tests, one at 50 cc/s and one at 100 cc/s. For both cases, peak power occurs near the beginning of the expansion. For the compression cases shown in Fig. 5.1.13, the heat transfer rate followed the same trend as power, but at a lower value. The expansion cases are different. Figure 5.1.14 shows that during expansion the heat transfer rate does not change nearly as much as the power. Initially, the power is nearly an order of magnitude

higher than the heat transfer rate. Then as the power decays when pressure drops, it soon equals the heat transfer rate. For the 50 cc/s case, this occurs at a normalized volume of 2.9, for the 100 cc/s case this occurs at a normalized volume of 3.8. This transition is seen in all of the baseline expansion tests. It helps explain the temperature-volume curves in Fig. 5.1.10.

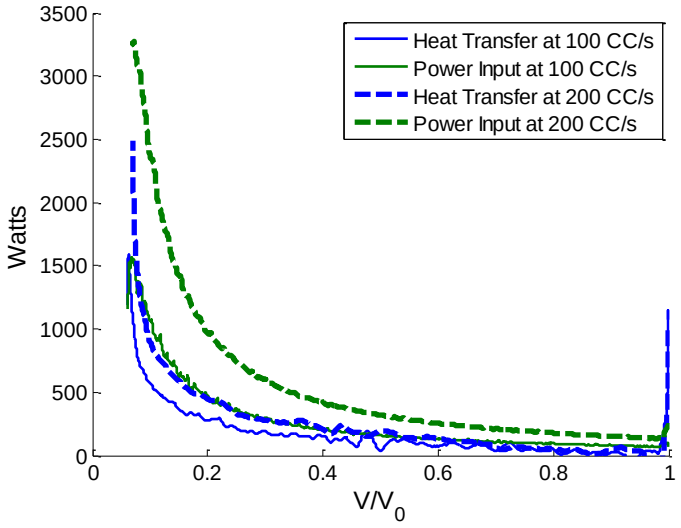

Fig. 5.1.13: Comparison of heat transfer rate and power input for two baseline compression cases with different compression rates. Initial volume is 2.2 L.

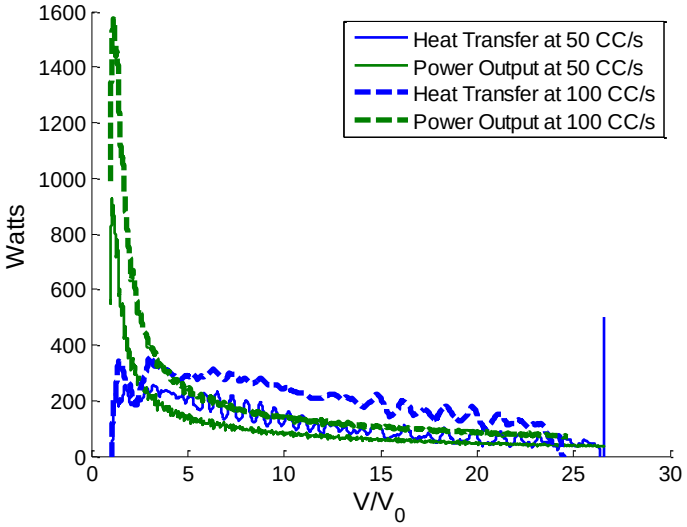

Fig. 5.1.14: Comparison of heat transfer rate and power output for two baseline expansion cases with different expansion rates. Initial volume is 75 CC.

The heat transfer coefficients for the compression cases are calculated using Eqn. (3.5), assuming a constant wall temperature of T_0 and are plotted for select baseline compression cases in Fig. 5.1.15 and select baseline expansion cases in Fig. 5.1.16. In both figures, a lag-less moving average filter with a span of 100ms has been applied. For the compression cases, from a normalized volume of 0.7 to 0.1, *h* increases as volume decreases. This happens because the air density is increasing during compression, increasing the Reynolds number, which improves heat transfer. The heat transfer coefficient, *h*, also increases as the compression rate increases. Again, this is because increasing the compression rate increases the average Reynolds number, improving heat transfer. The trends in h are less clear at the beginning of compression because ΔT is relatively small and fluctuates between positive and negative values. Similar trends in h are seen in expansion as shown in Fig. 5.1.16. As in compression, *h* is higher when volumes are smaller and air density is high, increasing with piston velocity.

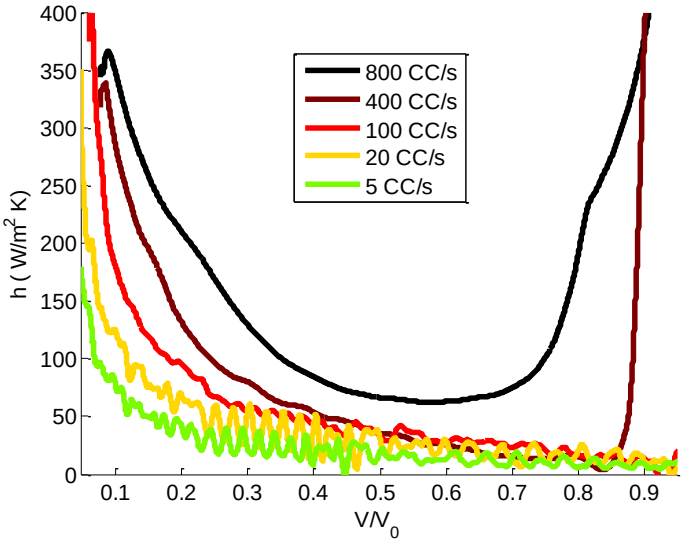

Fig. 5.1.15: Compression heat transfer coefficient plotted against volume for five constant compression rates as indicated in the legend. Initial volume is 2.2 L.

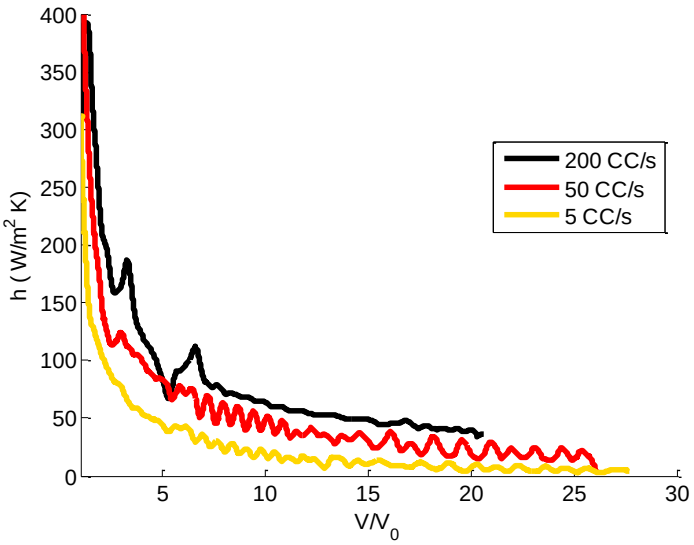

Fig. 5.1.16: Expansion heat transfer coefficient plotted against volume for three constant expansion rates as indicated in the legend. Initial volume is 75 cc.

In Fig. 5.1.17 the compression and expansion efficiencies, given by Eqn. (3.6) and Eqn. (3.7), respectively, are plotted against mean power for all baseline cases. Recall that these efficiency definitions are more conservative and do not include ejection work. For compression, mean power is based on the stored power, as given by Eqn. (3.11). For expansion, mean power is based the recovered power, as given by Eqn. (3.12). Efficiency effectively and concisely characterizes the performance of the compression or expansion process. For both compression and expansion there is a clear trend that efficiency decreases as power increases. A total of 16 compression tests and 15 expansion tests were performed. A few of these tests were repeat tests to show the repeatability of the experiments.

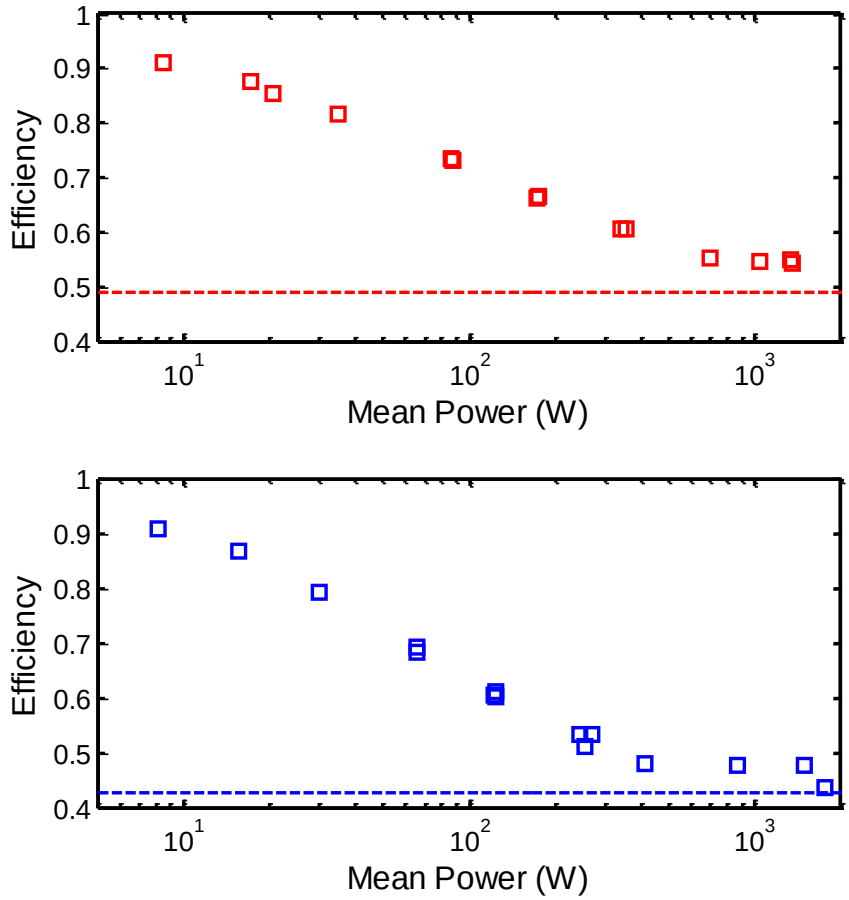

Fig. 5.1.17: Baseline compression and expansion efficiencies, given by Eqns. (3.6) and (3.7) plotted against mean power, given by Eqns. (3.11) and (3.12). The top plot, red, is compression cases and the bottom plot, blue, is expansion. The dashed line is the theoretical minimum efficiency corresponding to adiabatic compression or expansion.

These experiments covered more than three orders of magnitude of compression and expansion power, from less than 10 W to more than 1000 W. Compression efficiency varied from 91.0% at low power to 54.4% at high power. By definition, for a pressure ratio of 30, the adiabatic compression efficiency is 49.0% as shown by the dashed line. Expansion efficiency varied from 90.8% at low power to 43.5% at high power. By definition, for an expansion pressure ratio of 30, the adiabatic efficiency is 42.6%, as shown by the dashed line. These efficiencies are calculated with Eqns. (3.6) and (3.7), using a

conservative approach which does not include low pressure work or "ejection" work (as given by Eqns. (3.9) and (3.10)). Adding these additional terms to the numerator and denominator increases the efficiency by a few percent. It is valid to do this when the compressor is paired with an appropriate system, such as Van de Ven and Li's Open-Accumulator based approach [6]; however, the conservative approach is used in this thesis to focus on the compression/ expansion process directly without giving attention to the system of which it is part. Appendix B contains the essential data from all tests in this thesis and is sufficient to calculate alternate definitions of efficiency.

5.2 Uniform Porosity Results

Near-constant flow profiles (similar to Figs. 5.1.1 and 5.1.2), ranging from 12 cc/s to 800 cc/s, were used in the tests with uniformly distributed porous media. Figure 5.2.1 shows select pressure-volume curves for the compression cases with a uniform distribution of 2.5 mm interrupted plates. Figure 5.2.3 shows select pressure-volume curves for expansion cases with the same uniform distribution. Both figures include the fastest and slowest tests conducted as well as one intermediate-speed test. In general, the tests with the uniform distribution of porous media are closer to isothermal than the baseline cases, but similar trends are observed. Figure 5.2.2 plots the polytropic coefficients for compression tests with uniformly distributed interrupted plates. The polytropic coefficients from the baseline tests without porous media are included for reference.

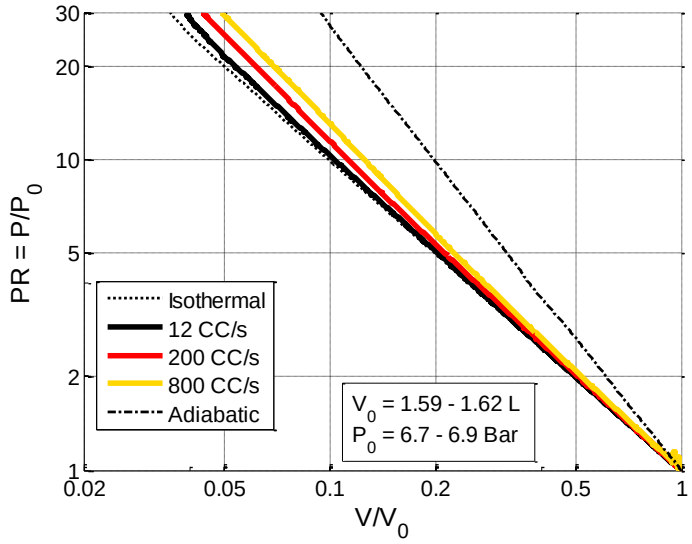

Fig. 5.2.1: Pressure-Volume curves for uniform insert compression cases. The legend indicates the constant compression rate used. Axes are in log scale. Pressure and volume have been normalized by initial conditions which are shown in the figure.

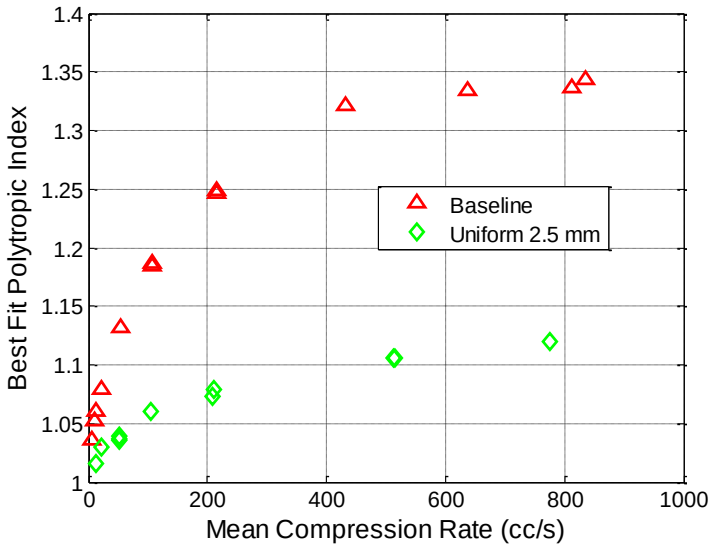

Fig. 5.2.2: Polytropic index vs. compression rate for cases using a uniform distribution of 2.5mm interrupted plates and baseline cases without porous media.

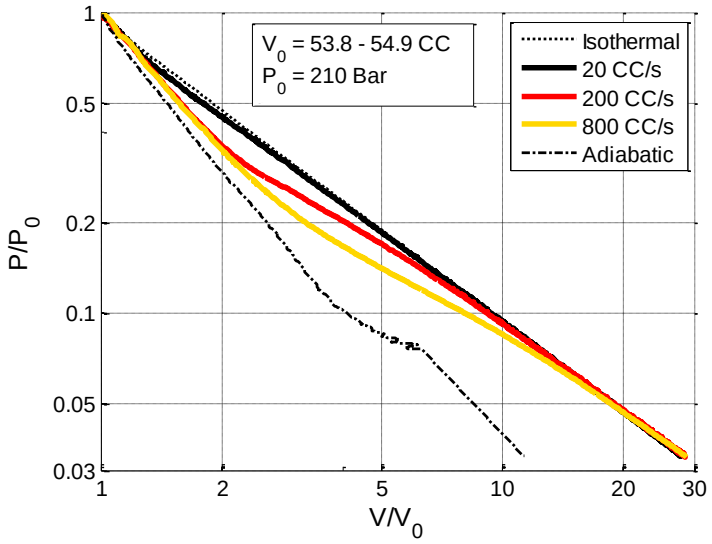

Fig. 5.2.3: Pressure-Volume curves for uniform insert expansion cases. The legend indicates the constant expansion rate used. Axes are in log scale. Pressure and volume have been normalized by initial conditions which are shown in the figure.

As in the baseline compression cases, the pressure-volume curves are approximately linear on the log-log plot. The polytropic coefficients for these tests varied from 1.02 at slow compression rates to 1.12 at the fastest compression rates. These values are significantly lower than for the cases without inserts at the same compression rate. Figure 5.2.2 shows that for the same polytropic coefficients, cases with a uniform distribution of 2.5mm interrupted plates achieved compression rates that were an order of magnitude faster than the baseline case. Similar to Fig. 5.1.8, Fig. 5.2.3 shows an observable change from near-adiabatic to near-isothermal during the expansion process; however, the expansion cases with porous media inserts are more efficient than those cases without.

The temperature-volume curves for compression and expansion are shown in figures 5.2.4 and 5.2.5, respectively. These figures show the same trends in temperature as those of the baseline figures, but the overall temperature change has been reduced. The

temperature-volume curves will be compared directly in Section 5.4, but for a quick comparison, Fig. 5.1.9 can be compared with Fig. 5.2.4 and Fig. 5.1.10 can be compared with Fig. 5.2.5.

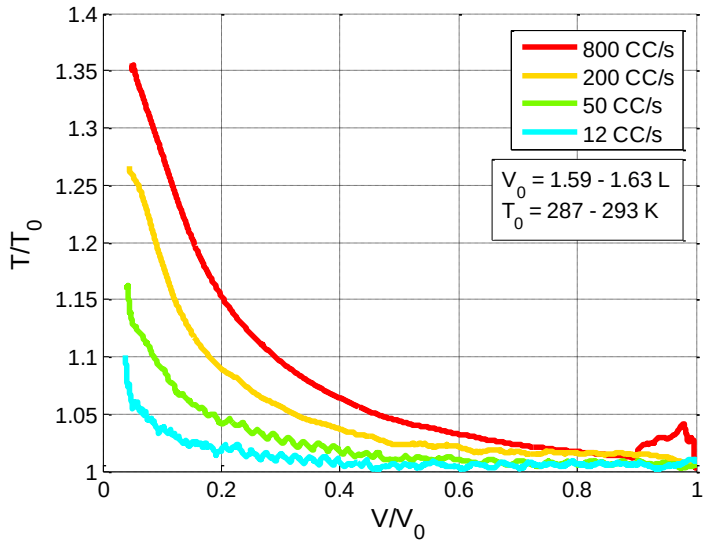

Fig. 5.2.4: Compression temperature for the uniform porous medium distribution at four different compression rates as indicated in the legend. Axes have been normalized by initial values which are shown in the figure.

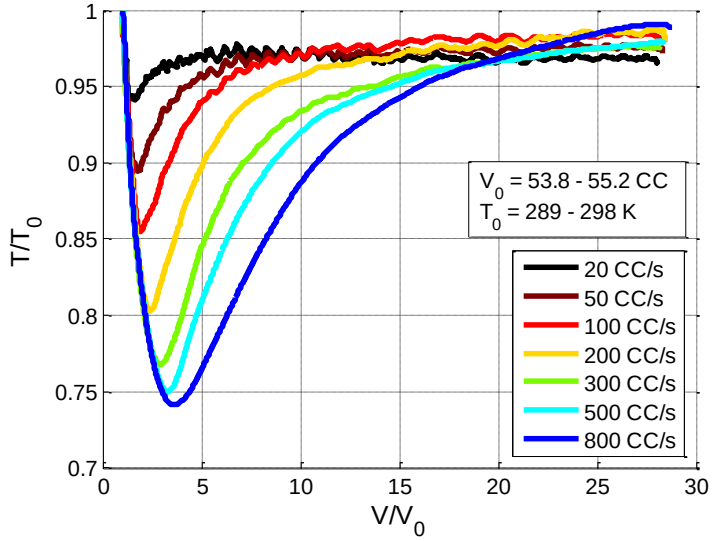

Fig. 5.2.5: Expansion temperature for the uniform porous medium distribution at seven different expansion rates as indicated in the legend. Axes have been normalized by initial values which are shown in the figure.

It is interesting to note that in Fig. 5.2.5 the fastest expansion case returns to the initial temperature fastest at the end. This trend was not observed in the baseline expansion tests where the faster expansion tests were always cooler than the slower expansion tests. Figures 5.2.6 and 5.2.7 help to explain this. Figure 5.2.6 plots the heat transfer rate during the expansion tests. It shows that the heat transfer rate is greater in the faster expansion cases. However, it is also known that increasing the expansion rate increases the power. Figure 5.2.7 plots the difference between power output and heat transfer rate, which is the time rate change of internal energy. In Fig. 5.2.7, negative values are regions where the instantaneous output power is greater than the instantaneous heat transfer rate. From these figures, it seems as though a fast expansion rate during the beginning of expansion dramatically reduces air temperature because power is much greater than the heat transfer rate; however, near the end of expansion, when pressure is low, a fast expansion rate causes air temperature to rise because the heat transfer rate is greater than the power. This also explains why the final temperature for the fastest expansion test is warmer than the slower cases (Fig. 5.2.5).

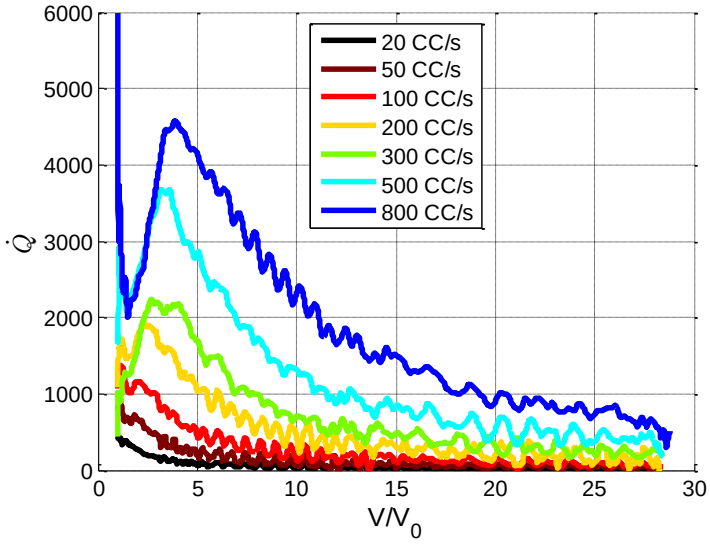

Fig. 5.2.6: Heat transfer rate in Watts plotted against volume for seven expansion cases with uniformly distributed 2.5 mm interrupted plates. Constant expansion rates shown in legend. Volume has been normalized by initial value of 54 cc.

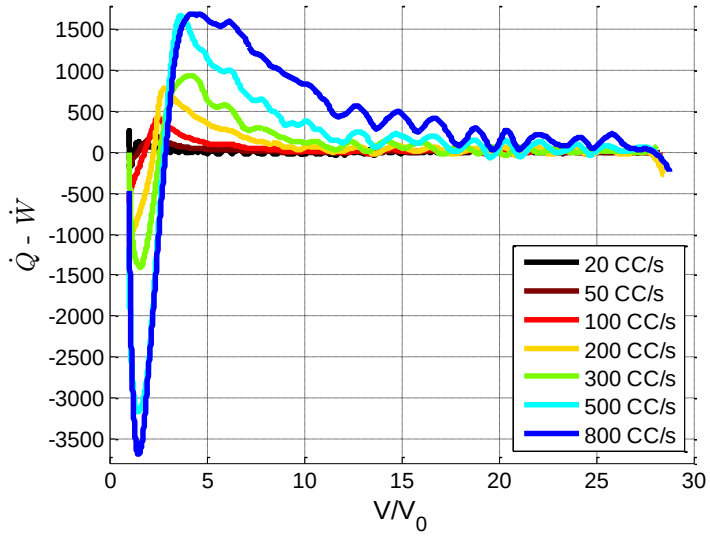

Fig. 5.2.7: Rate of internal energy change for seven expansion cases with uniform 2.5 mm distribution plotted against volume. Rate of internal energy change in Watts and volume has been normalized by initial value of 54 cc. Legend denotes expansion rate.

A volume and time-averaged heat transfer coefficient has been found for compression cases with a constant compression rate and the uniform distribution of 2.5 mm interrupted plates. The volume averaging of the heat transfer coefficient is a natural

result of using bulk temperature of the air, T_{air} , and the total instantaneous heat transfer rate, $\dot{Q}$. The surface area under consideration, A_{air} ,is the total surface area in contact with the air. This includes the side walls of the compressor, the top cap, and the liquid interface, but the majority of the available surface area is provided by the porous medium. The temperature of the porous medium, T_{media}, is not measured directly; rather, a lumped capacitance model is used to estimate the temperature rise. The initial temperature of T_{media} is assumed to be equal to T_{air}. The increase in media temperature for each time step is found by dividing the total heat transfer for that step by the heat capacity of the media exposed to the air for that time step. This method assumes that the heat flux from the air to the media is uniform and that the media has a uniform temperature. The temperature rise for T_{media} during a compression experiment varied from 12.9 K to 17.2K . This allows an average heat transfer coefficient to be calculated using Eqn. (5.1), an expansion of Eqn. (3.5).

$$\overline{h_{bulk}} = \frac{\dot{Q}}{A_{air}\,(T_{air} - T_{media})} \tag{5.1}$$

For added clarity, this volume averaged heat transfer coefficient, h_{bulk}, is time-averaged for 9 ranges during the compression process. These 9 regions are: 0-30%, 30-50%, 50-65%, 65-75%, 75-85%, 85-90%, 90-95%, 95-97.5%, and 97.5-100% of total compression time. These ranges were selected to better capture the changes in heat transfer coefficient near the end of the compression process. The calculated values for *h* are shown in Fig. 5.2.8, plotted against volume. This averaging method captures the important features of how *h* changes during compression without the noise that is introduced by measurements and processing. As in the baseline case, heat transfer coefficient increases with density and velocity both of which are contained in Reynolds number.

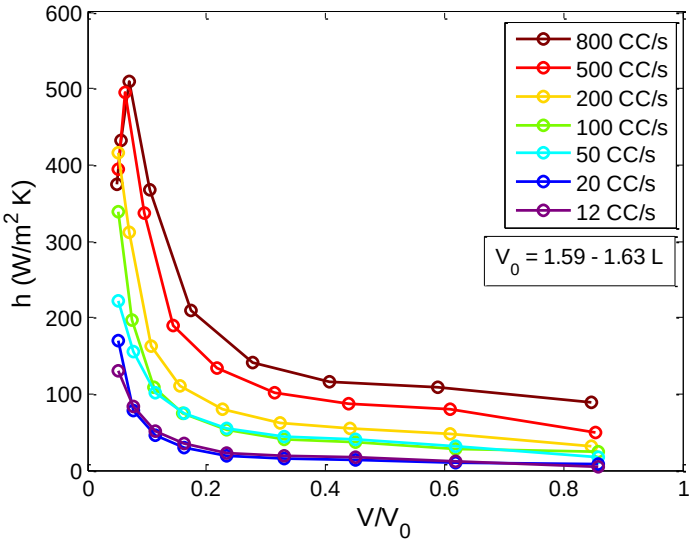

Fig. 5.2.8: Heat transfer coefficient for compression cases with uniform 2.5 mm interrupted plate porous inserts at 6 different compression rates. Volume has been normalized by initial volume, which is indicated in the figure. Legend denotes the compression rate.

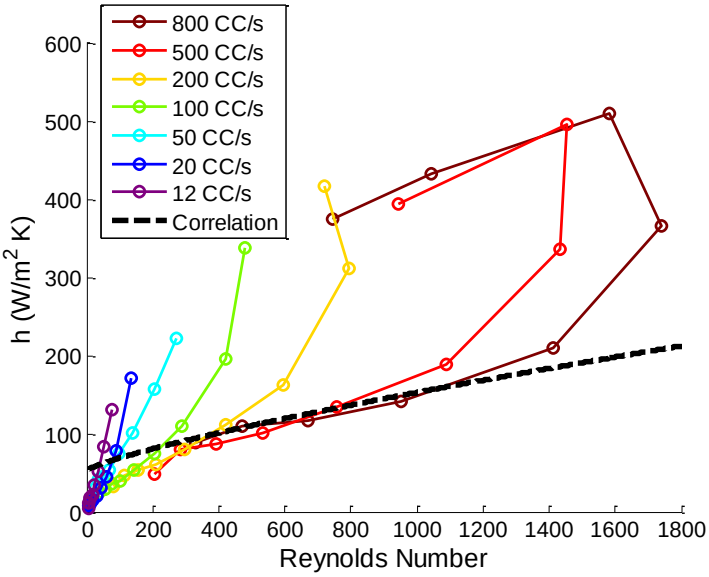

Fig. 5.2.9: Average heat transfer coefficient for several compression cases with uniform distribution of 2.5mm interrupted plates. Legend indicates compression rate. The characteristic length for Reynolds number is the hydraulic diameter of the plates and the characteristic velocity is half of the piston velocity

In Fig. 5.2.9, the values from Fig. 5.2.8 are plotted against Reynolds number, which is based on the hydraulic diameter of the interrupted plates and a characteristic velocity

that is equal to half of the piston velocity. This characteristic velocity is accurate if the air velocity varies linearly from the piston to the top cap, and there is no secondary flow. Fig. 5.2.9 shows that the data do not collapse to the same curve. There appears to be an additional parameter that is necessary for the data to collapse. For reference, the data are plotted with Zhang's heat transfer correlation for interrupted plates [24]. The experiments are generally in agreement with the correlation at moderate Reynolds numbers, but there are significant deviations at the end of the compression process and slight deviations at low Reynolds numbers. Reasons for these discrepancies will be discussed further in Chapter 6.

All of the uniform insert compression and expansion tests are summarized in Fig. 5.2.10 where efficiency is plotted against mean power. As in the baseline case, efficiency drops as power increases for both compression and expansion. Power levels range from 20 to 1270 W for compression and 34 to 1060 W for expansion. Compression efficiencies range from 79% to 95% and expansion efficiencies range from 77% to 95%. For all compression and expansion cases, the addition of porous media inserts improve efficiency (for the same power density) and power density (for the same efficiency). A comparison of all results will be presented in section 5.4.

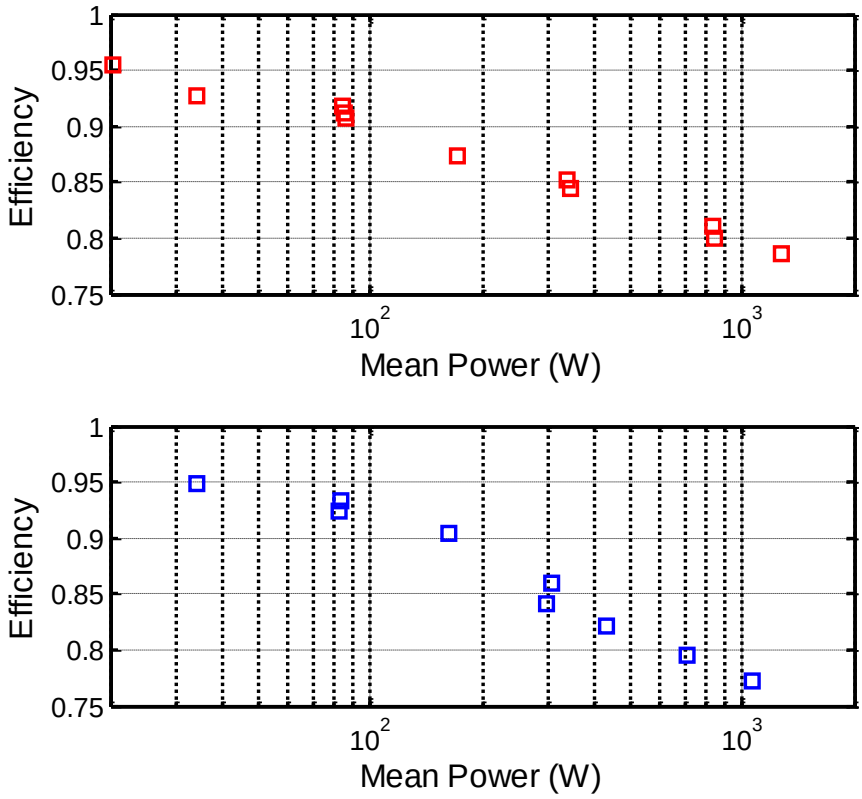

Fig. 5.2.10: Uniform distribution compression and expansion efficiencies plotted against mean power. The top plot, red, is compression and the bottom plot, blue, is expansion.

5.3 Non-Uniform Porosity Results

As discussed in Chapter 4, several tests with a non-uniform distributions of porous media were conducted. Four compression and expansion rates were considered (50, 100, 200, 500 cc/s) for each of the five distributions. The five distributions are labeled "A" through "E" and are shown in Fig. 4.5.1, where the vertical locations of the porous medium, expressed as a percentage, are 14%, 72%, 86%, 97%, and 100% for distributions A, B, C, D, and E, respectively. The pressure-volume curves for select non-uniform distribution compression tests are shown in Fig. 5.3.1. The pressure-volume curves for select expansion cases are shown in Fig. 5.3.2. Both figures show the most efficient and least efficient run as well as

two runs with equal efficiencies between the maximum and minimum. It is interesting to see that in Fig. 5.3.1 the two intermediate compression cases have the same efficiencies and very similar pressure-volume curves, despite having very different flowrates and distributions. By moving the porous medium from the bottom (distribution A) to the middle (distribution C), the flowrate could be increased by a factor of five without changing efficiency.

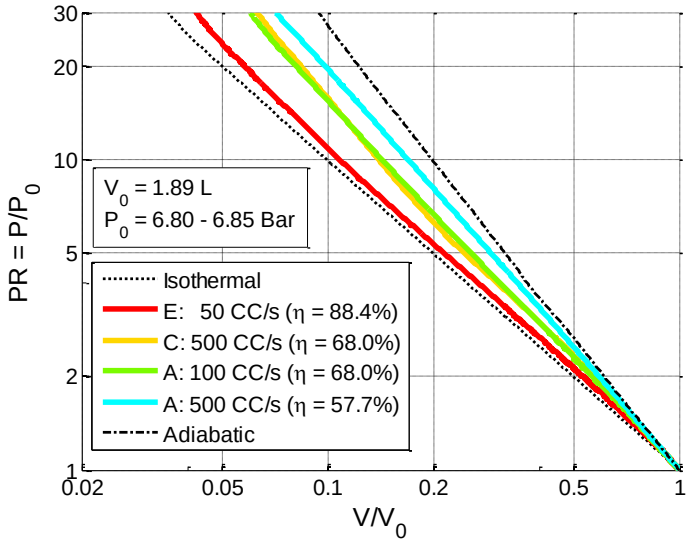

Fig. 5.3.1: Pressure is plotted against volume for several compression cases with non-uniform insert geometries. Axes have been normalized by initial values which are shown in the figure. The legend indicates the insert geometry by case letter, the compression rate, and the efficiency.

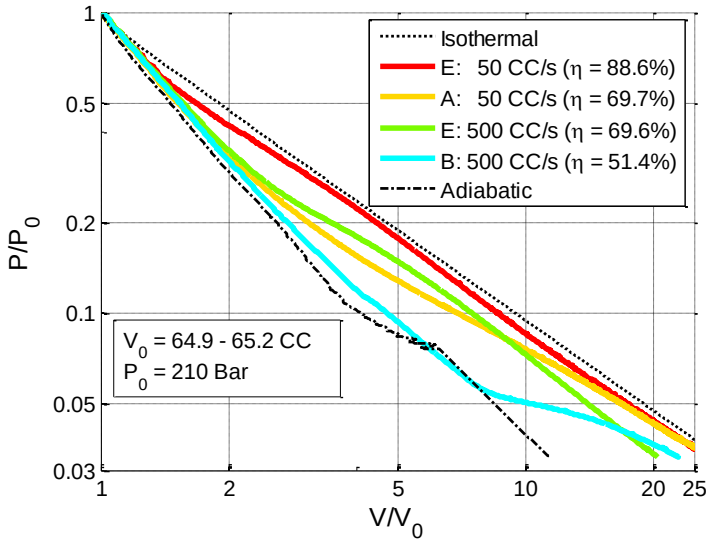

Fig. 5.3.2: Pressure is plotted against volume for several non-uniform expansion cases. Axes have been normalized by initial values which are shown in the figure. The legend indicates the distribution, the compression rate, and the efficiency.

In Fig. 5.3.2, one can see that moving the porous medium from the bottom (distribution A) to the top (distribution E) allowed the flowrate to increase by a factor of 10 without a decrease in expansion efficiency. Although the efficiencies of the two intermediate cases are the same, unlike the compression cases in Fig. 5.3.1 the pressure-volume curves of the two cases are quite different. The distribution E case is closer to the isothermal curve at the beginning of expansion, but cools near the end. Distribution A begins closer to the adiabatic curve, but warms near the end.

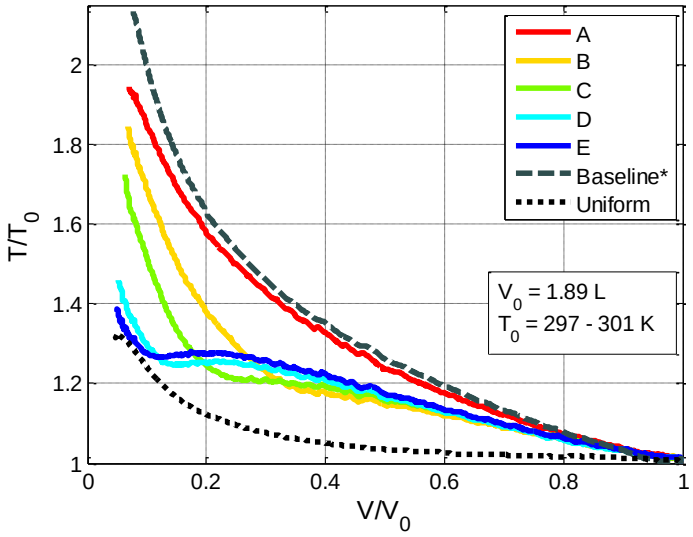

Fig. 5.3.3: Compression temperature for different distributions at compression rate of 500 cc/s (*Baseline case has compression rate of 400 CC/s). Axes have been normalized by initial values. Initial conditions for non-uniform cases are shown in the figure.

Figure 5.3.3 shows the temperature for different distributions at the same compression rate, 500 cc/s. Recall from Chapter 4 that the initial volume, initial total surface area, and initial pressure are the same for all five tests; the only difference is the location of the porous medium. There is a clear a difference between the five cases. As the porous media inserts are moved from the bottom to the top, the maximum temperature rise decreases. For distributions D and E, the temperature actually decreases slightly once the air is pushed into the region containing porous media. This trend will be shown more clearly in figures 5.3.4, 5.3.5, and 5.3.6, where compression temperature is plotted against volume for a specific distribution for the four different compression rates. Note that distribution E has a final temperature very close to the uniform distribution of interrupted plates, while distribution A has a temperature profile that is similar to the case with no inserts. Clearly, the location of porous media in the compression chamber dramatically affects the temperature rise.

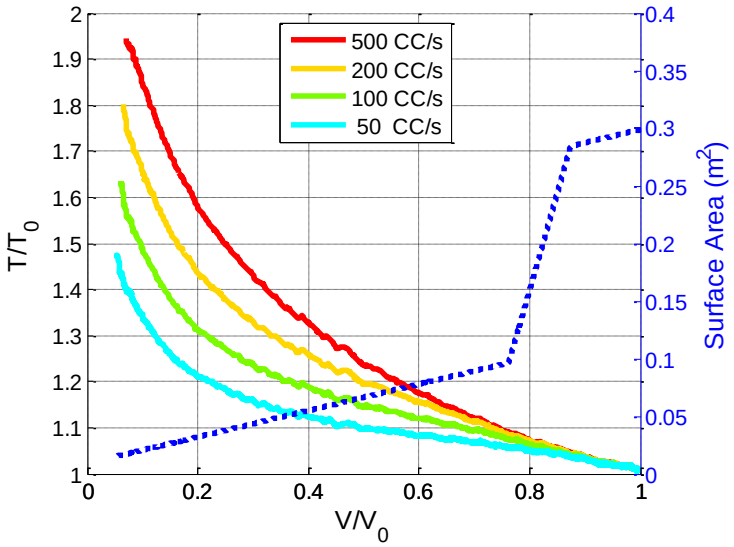

Fig. 5.3.4: Compression temperature is plotted against volume for distribution A at different compression rates, indicated in the legend. The secondary y-axis shows the total surface area available at a given volume.

Figure 5.3.4 plots the temperature for the worst performing distribution, distribution A, with the porous medium mostly at the bottom of the chamber. The trend in temperature between the four different compression rates is consistent. The trends and values observed for distribution A were similar to the cases where no porous medium was used (refer to Fig. 5.1.9). Distribution A, is only marginally better than the case with no porous insert. More interesting trends are seen for distribution C (Fig. 5.3.5) and distribution E (Fig. 5.3.6). For distribution C (Fig. 5.3.5) there is a quasi-isothermal region observed for the three slowest cases. As the compression rate increases, the value of this temperature increases and the duration of it decreases. For the fastest case, this quasi-isothermal region with a slope of zero, has disappeared. For the same compression rates, distribution C is cooler than distribution A, but warmer than distribution E.

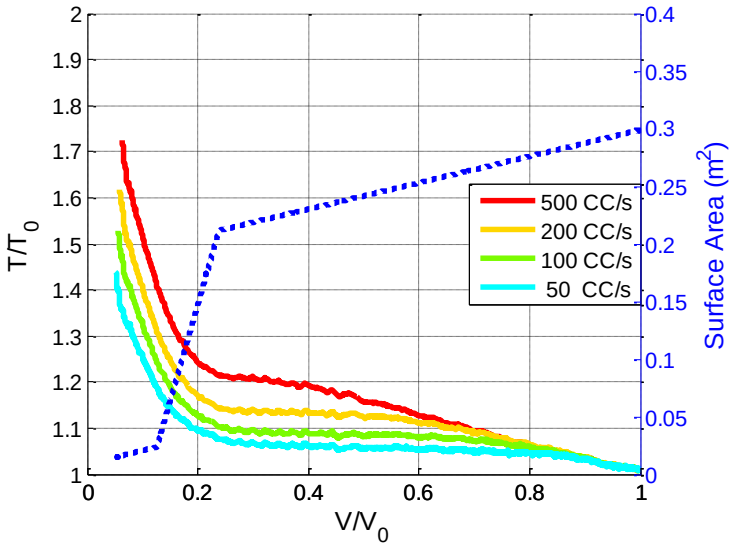

Fig. 5.3.5: Compression temperature is plotted against volume for distribution C at different compression rates, indicated in the legend. The secondary y-axis shows the total surface area available at a given volume.

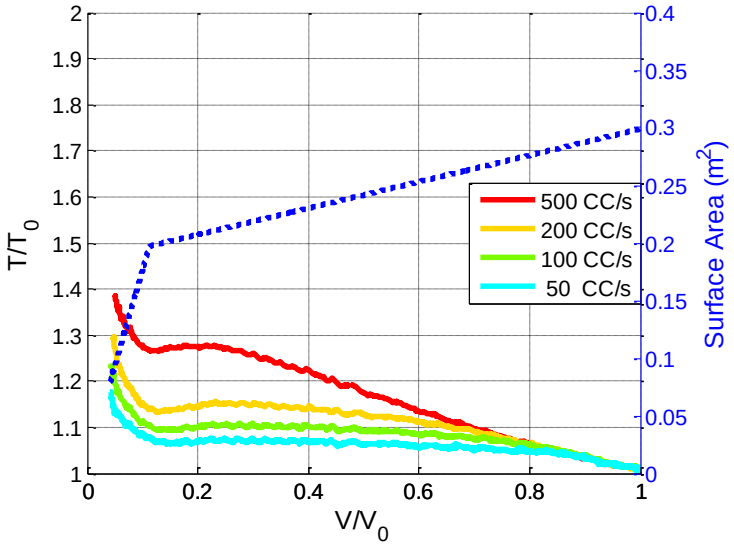

Fig. 5.3.6: Compression temperature is plotted against volume for distribution E at different compression rates, indicated in the legend. The secondary y-axis shows the total surface area available at a given volume.

For distribution E, (Fig. 5.3.6) there is a decrease in temperature that occurs as the warm air is pushed into the region having more porous media. This drop in temperature begins at around 0.2 to 0.3 of initial air volume for all cases. When the liquid piston is at this point, there is a small gap under the porous medium, but most of the air has been

pushed into the region with porous media. Distribution E, with the porous media at the top of the chamber, is the best-performing distribution.

The expansion temperatures for non-uniform cases are plotted for the five distributions at a constant expansion rate of 200 cc/s in Fig. 5.3.7. Features that have been seen in other results are repeated here; specifically the near-adiabatic drop in temperature at the onset of expansion, a minimum temperature reached relatively early in the expansion, and a warming of the gas caused by a decrease in power.

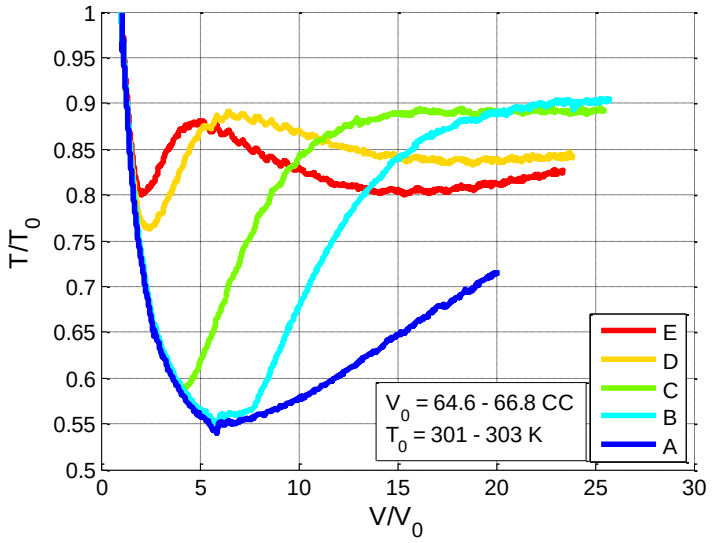

Fig. 5.3.7: Expansion temperature for five distributions at constant 200 cc/s expansion rate. Axes have been normalized by initial values, which are shown in the figure. The legend denotes the distribution.

There are several interesting trends that are unique to the non-uniform distributions. It is interesting to see that distributions E and D, which are more efficient, have lower final temperatures than distributions C and B at the same expansion rate. Distribution E is especially interesting because temperature falls, rises, falls again, and rises again even though the only thing that has changed is the location of the porous medium. This oscillation in temperature is caused by a balancing between instantaneous power and

instantaneous heat transfer rate. The temperature initially drops because the power output is so high and there are no thermal gradients to drive heat transfer. Power drops quickly and heat transfer becomes more dominant because there is much surface area in the top region of the expander. However, as the expansion continues, more air enters regions of the expander where there is little surface area. The final rise in temperature is caused when the power drops so low that it is surpassed by the heat transfer rate.

Figures 5.3.8, 5.3.9, 5.3.10, and 5.3.11 show the expansion temperature profiles for four different expansion rates and the five different distributions. Additionally, the surface area has been plotted against volume on the second y-axis as the temperature profile is somewhat correlated with changes in surface area.

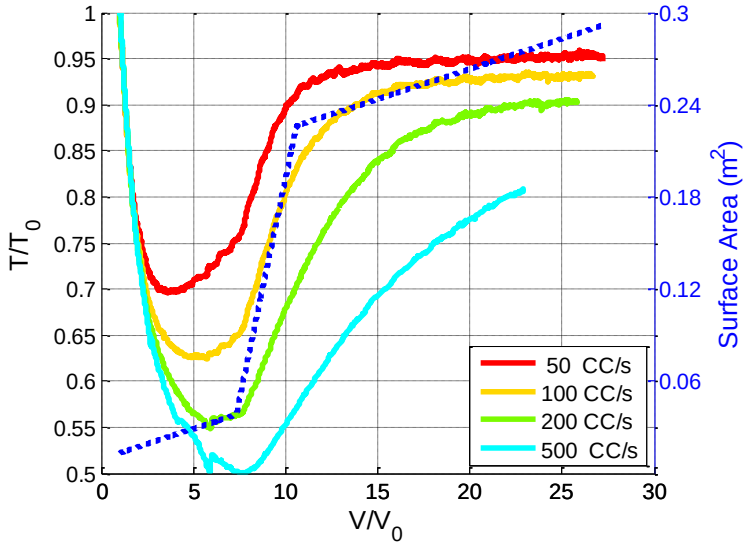

Fig. 5.3.8: Expansion temperature for distribution B at different constant expansion rates. Axes have been normalized by initial values, which are shown in the figure. The legend denotes the expansion rate.

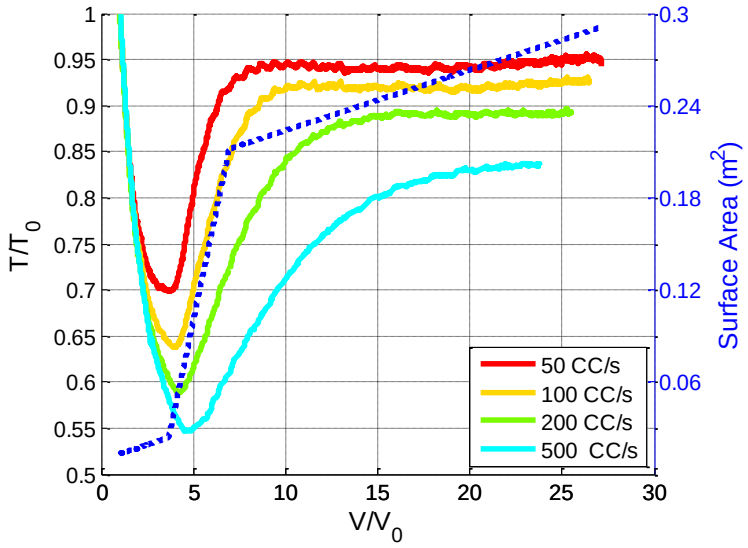

Fig. 5.3.9: Expansion temperature for distribution C at different constant expansion rates. Axes have been normalized by initial values, which are shown in the figure. The legend denotes the expansion rate.

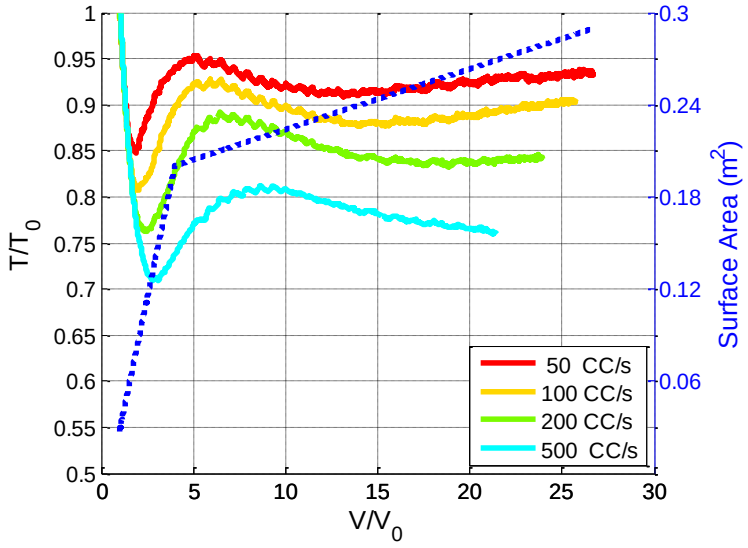

Fig. 5.3.10: Expansion temperature for distribution D at different constant expansion rates. Axes have been normalized by initial values, which are shown in the figure. The legend denotes the expansion rate.

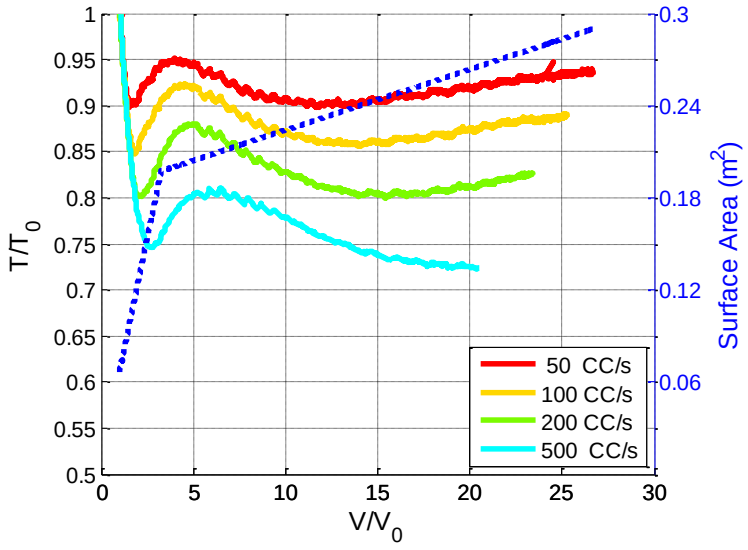

Fig. 5.3.11: Expansion temperature for distribution E at different constant expansion rates. Axes have been normalized by initial values, which are shown in the figure. The legend denotes the expansion rate.

Distribution E (Fig. 5.3.11) is the most effective distribution of the five that were tested and in these figures distribution E is generally warmer than the other distributions. The temperature oscillation that was observed in Fig. 5.3.7 is seen again for the additional cases plotted in figures 5.3.10 and 5.3.11. Figure 5.3.11 shows a temperature trend that has not been observed in any other experiments. For the fastest expansion and with distribution E, the minimum temperature does not occur early in the expansion as seen for all other cases. Rather, the minimum temperature happens during the second dip in temperature.

Figure 5.3.12 shows the efficiency for all non-uniform distribution compression and expansion tests conducted. Distributions are indicated with symbols as described in the legend.

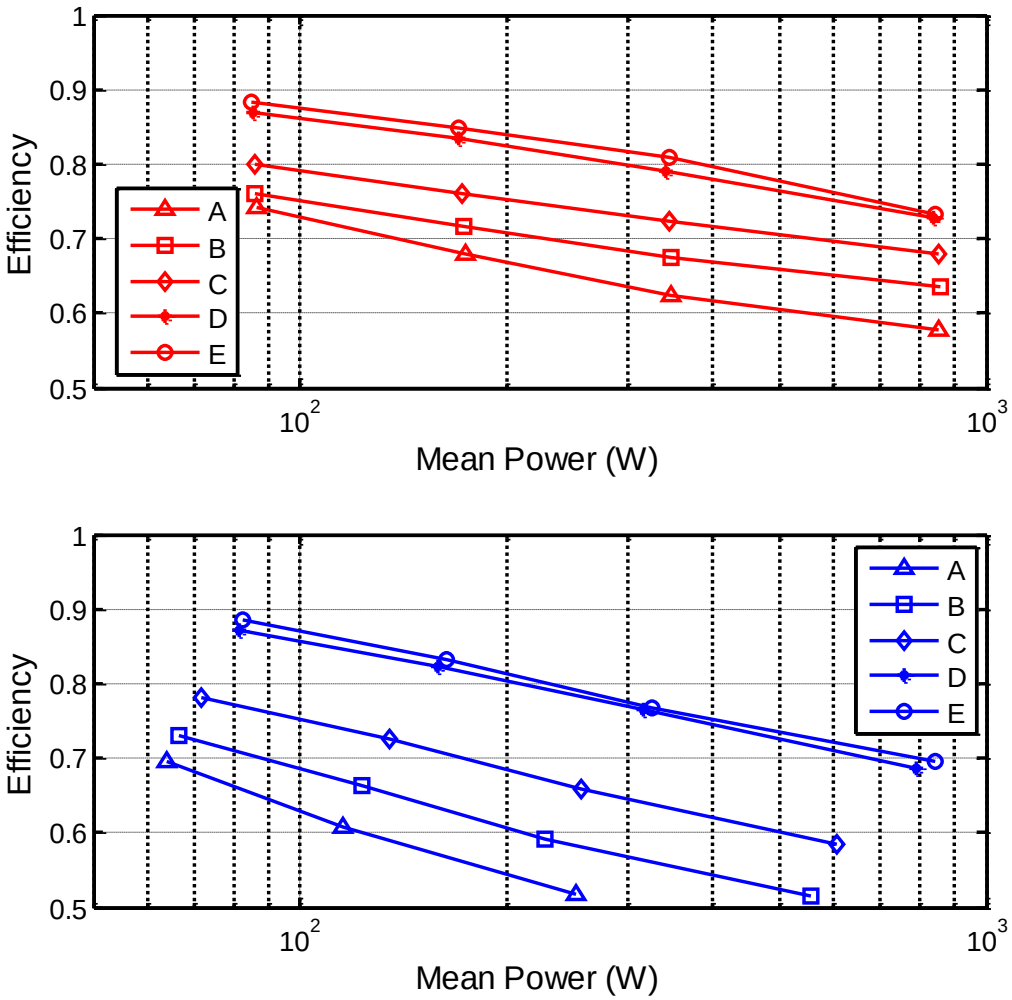

Fig. 5.3.12: Compression and expansion efficiency plotted against mean power in log scale. Compression cases are shown in red in the top figure. Expansion cases are shown in blue in the bottom figure. The distribution used is indicated by symbols in the legend.

Compression and expansion cases with distribution E were found to be optimal. For both compression and expansion, moving the porous medium from the worst location to the optimal location improved power density by an order of magnitude for the same efficiency. Likewise, moving the porous medium from the bottom (distribution A) to the top (distribution E) improved compression efficiency from 62% to 81% with the same power and expansion efficiency from 58% to 84% with the same power. For expansion

cases, efficiency is plotted against mean recovered power, which is dependent upon the efficiency. As the efficiency of an expansion process decreases, the amount of energy that is recovered also decreases. This is the reason why the expansion cases decrease in both power and efficiency as the expansion rate is increased. This is not seen in the compression cases because compression power is based on stored energy, which is independent of efficiency. In short, an inefficient compression process causes the work input to increase, but does not affect stored energy, while an inefficient expansion process reduces the amount of energy recovered but does not affect the potential energy that could have been recovered.

Figure 5.3.13 attempts to plot the data from Fig. 5.3.12, normalized in such a way that the data collapse. Intuition suggests that surface area should be a dominant part of the normalization because the more efficient cases are cases where the air is exposed to solid surfaces for a longer time. Surface area and specific surface area (*SSA(t)*, that is the instantaneous ratio of surface area exposed to air to air volume) are both functions of time, which makes choosing an appropriate average surface area problematic. A number of weighted averages were considered, but the most successful average was the power-weighted average specific surface area, $\overline{SSA_{pwr}}$, given by Eqn. (5.2). Power density was divided by this average specific surface area to normalize the data. This normalization does better for compression than for expansion. This will be discussed further in chapter 6.

$$\overline{SSA_{pwr}} = \frac{\int_{t_0}^{t_f} SSA(t)Power(t)\,dt}{\int_{t_0}^{t_f} Power(t)\,dt} \tag{5.2}$$

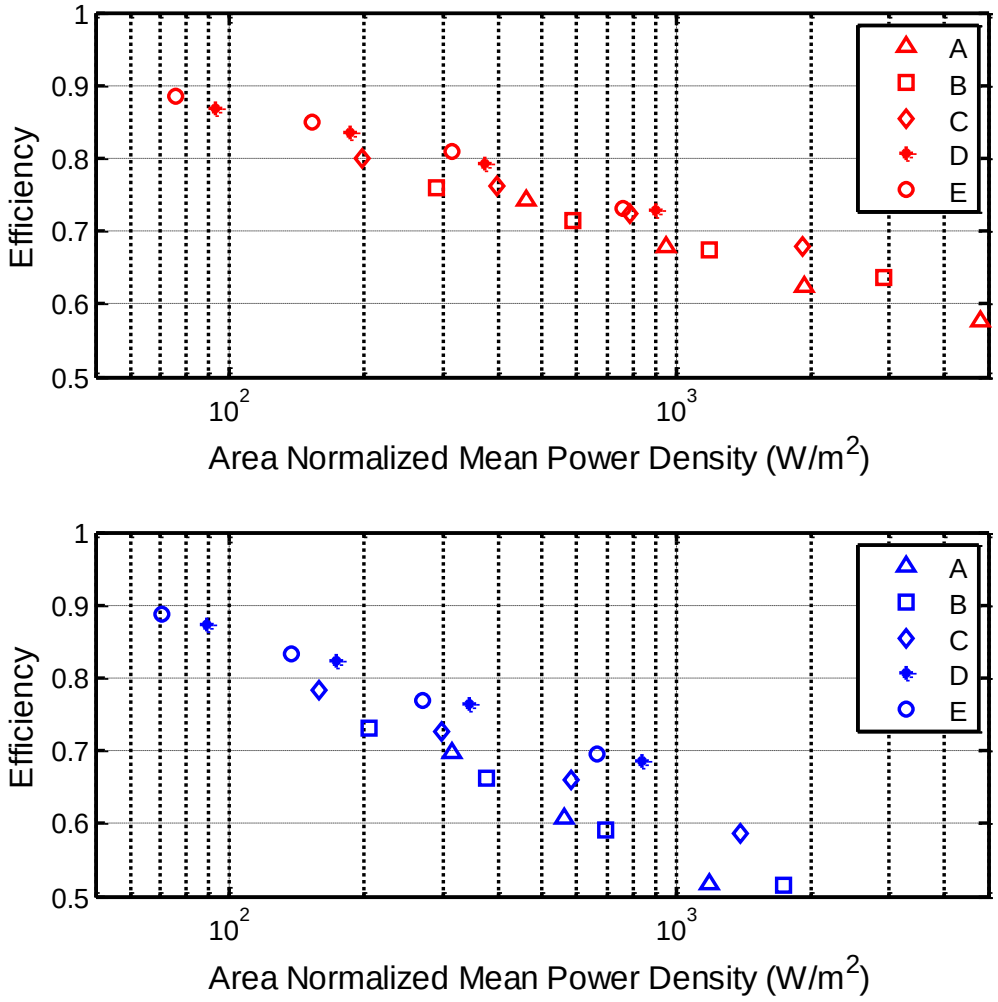

Fig. 5.3.13: Non-Uniform Efficiency vs. Area-Normalized Power Density. Compression (top) and Expansion (bottom) efficiency are plotted against the mean power per unit area. Power densities given by Eqns. (3.11) and (3.12) are divided by the power-weighted average specific surface area given by Eqn. (5.2) to give Area-Normalized Mean Power Density.

5.4 Comparison of All Results

Figures 5.4.1 and 5.4.2 plot the temperature profiles of baseline, uniform and non-uniform cases with flow rates selected such that they have similar efficiencies. Important details about the test are shown in the text boxes on the figures.

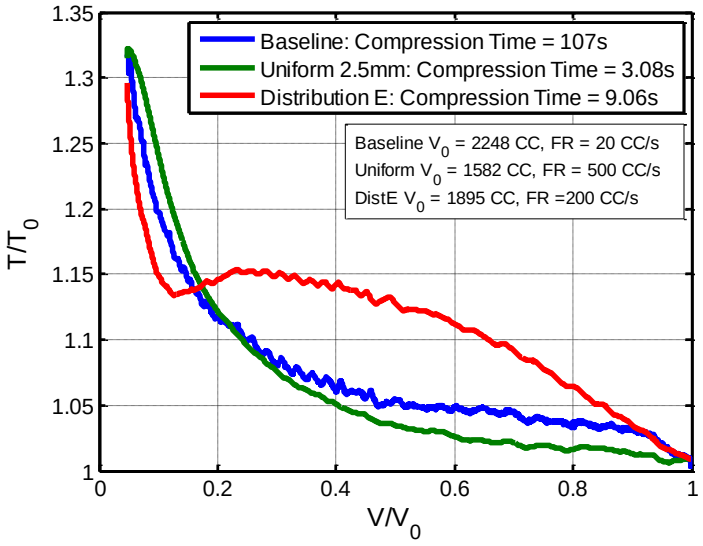

Fig. 5.4.1: Compression temperature plotted against volume for baseline, uniform, and non-uniform compression cases with the same efficiency of 81%. Initial volumes, flowrates, and total compression times are indicated.

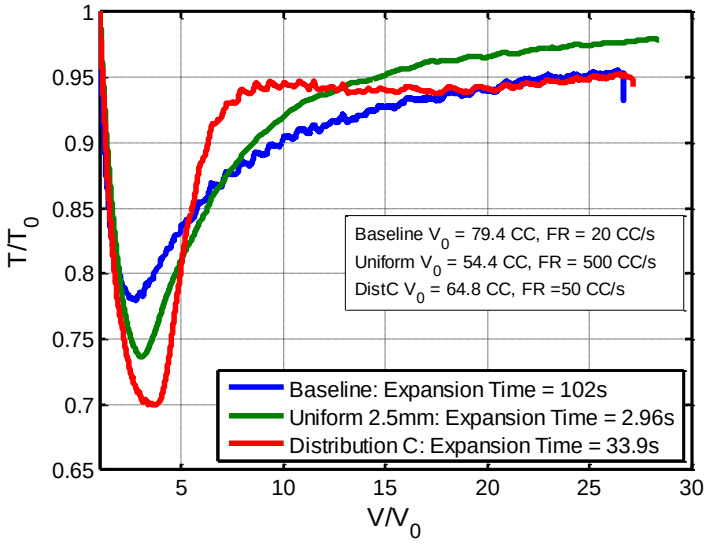

Fig. 5.4.2: Expansion temperature plotted against volume for baseline, uniform, and non-uniform expansion cases with the same efficiency of 79%. Initial volumes, flowrates, and total compression times are indicated.

Although the final temperatures are approximately the same for all three cases, the compression/expansion times for the three cases are very different. In order to achieve the same efficiency of 81% and 79%, the baseline case, with no porous media, requires the process to be relatively slow: 107s for compression and 102s for expansion.

Comparatively, the cases with a uniform distribution of porous media were able to take place over a much shorter period of time: 3.1s for compression and 3.0s for expansion. This has huge implications for the power density of the compressor/ expander. Filling the chamber with porous media allowed more work to be done in the same amount of time, without reducing efficiency or changing the compressor/ expander.

Both figures 5.4.1 and 5.4.2 show interesting trends in temperature. In Fig. 5.4.1 the temperature rises sharply in the initial stages of compression for the baseline case. This is caused by low heat transfer due to a low heat transfer coefficient, less surface area, and a small driving temperature difference. A similar sharp rise in temperature can be seen in the distribution E compression case in the first ~10% of compression. Another observation is that despite having a much higher temperature than the other two compression cases during the first 70% of the process, the distribution E compression case has the same efficiency. This can be attributed to the high heat transfer rate during the final 25% of the compression process. Figure 5.4.2 shows that the relationship between maximum temperature drop and expansion efficiency is not so straightforward – it is dependent on the distribution of porous media in the expansion chamber. All of the expansion tests plotted have the same efficiency of 79%, yet the drop in normalized temperature varies by over 35%.

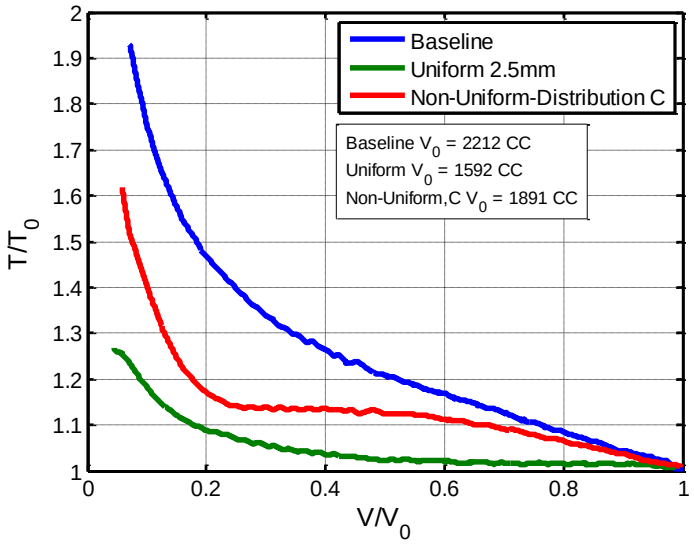

Fig. 5.4.3: Compression temperature plotted against volume for baseline, uniform, and non-uniform compression cases with the same compression rate of 200 cc/s. Initial volumes are noted.

Figure 5.4.3 shows the three compression cases that have the same compression rate. The case that is filled uniformly with interrupted plates is the closest to being isothermal. Distribution C is similar to the baseline case at the beginning and has the same slope near the end. During the middle portion, distribution C keeps the process at a constant temperature. Even a relatively small amount of surface area added to the middle of the chamber made a significant impact on the temperature – volume curves. Figure 5.4.4 shows the three expansion cases with the same expansion rate. As in compression cases, the case with the uniformly distributed inserts came closest to reaching the isothermal ideal. Even the small amount of porous media provided in the case marked distribution C allowed the temperature to rise much more quickly than in the baseline case.

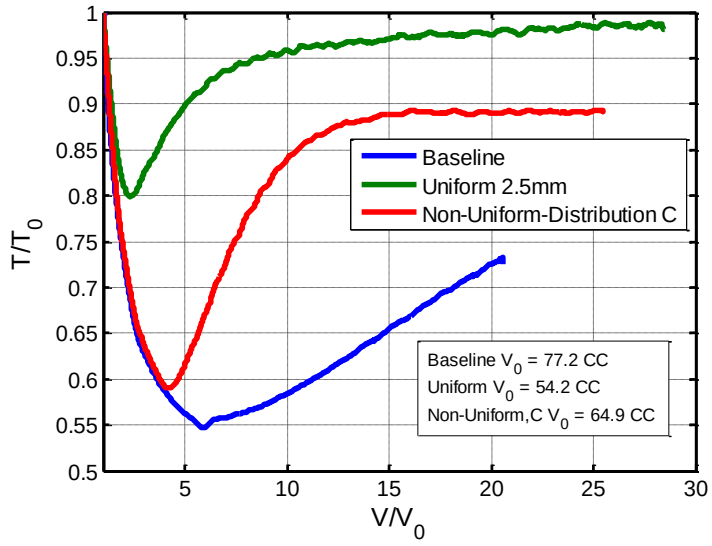

Fig. 5.4.4: Expansion temperature plotted against volume for baseline, uniform, and non-uniform expansion cases with the same expansion rate of 200 cc/s. Initial volumes are noted.

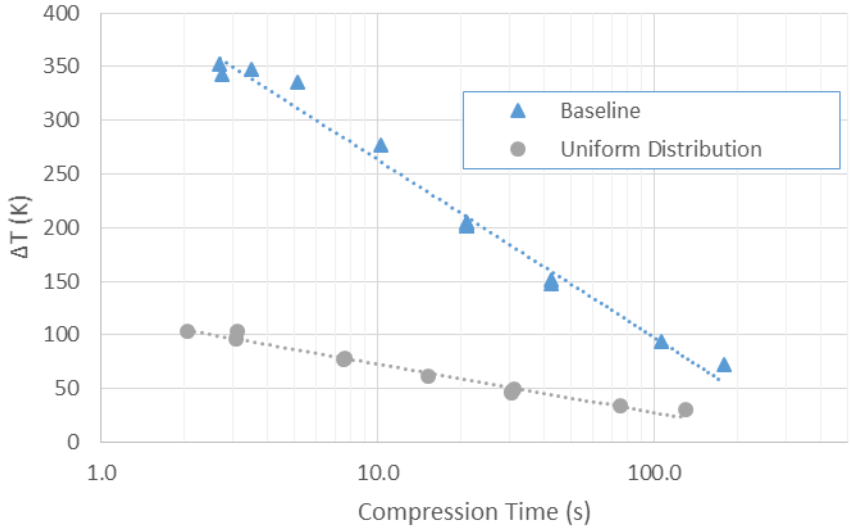

Fig. 5.4.5: Maximum temperature rise plotted against total compression time for all baseline and uniform distribution. X-axis is in log scale.

Figures 5.4.5 and 5.4.6 show the maximum temperature change for compression and expansion plotted against compression or expansion time. The change in gas temperature during compression or expansion, although not exact, is an indication of how efficient the process was. Only the baseline and uniform distribution cases are plotted. Non-uniform

distributions were not plotted here because, as was shown in Fig 5.3.11, the temperature trends of the non-uniform cases look very different from the temperature trends for baseline and uniform distributions. Figures 5.4.5 and 5.4.6 show a logarithmic relationship (linear on semi log plot) between maximum temperature change and compression / expansion time for the range of tests in this thesis (~1-500 s).

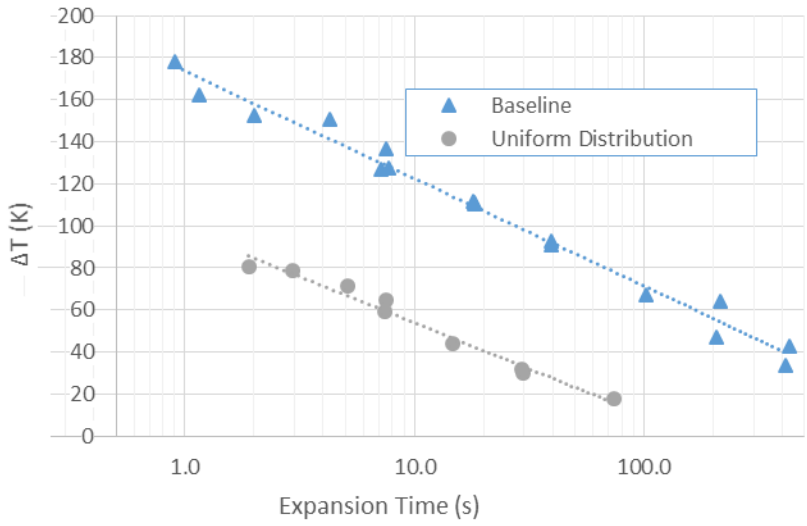

Fig. 5.4.6: Maximum drop in temperature plotted against total expansion time for baseline and uniform distribution expansion cases. X-axis is in log scale.

For all of the compression tests conducted in these experiments, a best fit polytropic index was found from the pressure-volume curve. Figure 5.4.7 plots these polytropic indices against compression efficiency. All the test points collapse along the same curve. This curve can be used to estimate efficiency directly from a pressure-volume curve. It should be noted that the adiabatic polytropic coefficient is 1.44, rather than 1.40 because of the deviation from ideal gas behavior. This method was not applied to the expansion cases as those tests tended to have pressure-volume curves that were not polytropic. As discussed in sections 5.1 and 5.2 expansion tests tended to be quasi-adiabatic at the onset

of expansion and quasi-isothermal near the end of expansion, with a period of transition in between. In Fig. 5.4.8 the polytropic indices for all compression tests are plotted against compression rate.

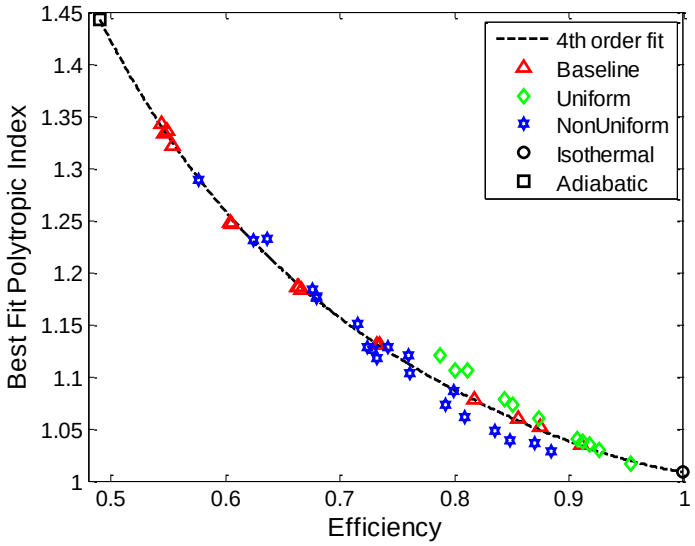

Fig. 5.4.7: Polytropic index of all compression cases plotted against efficiency

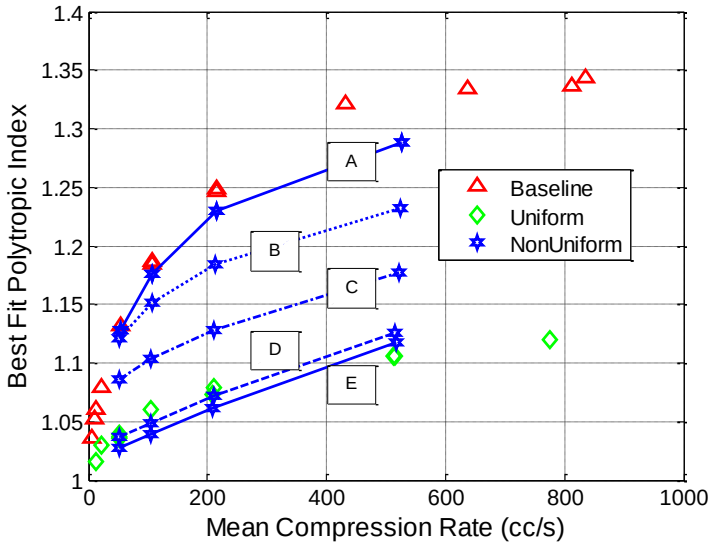

Fig. 5.4.8: Polytropic index of all compression cases plotted against compression rate.

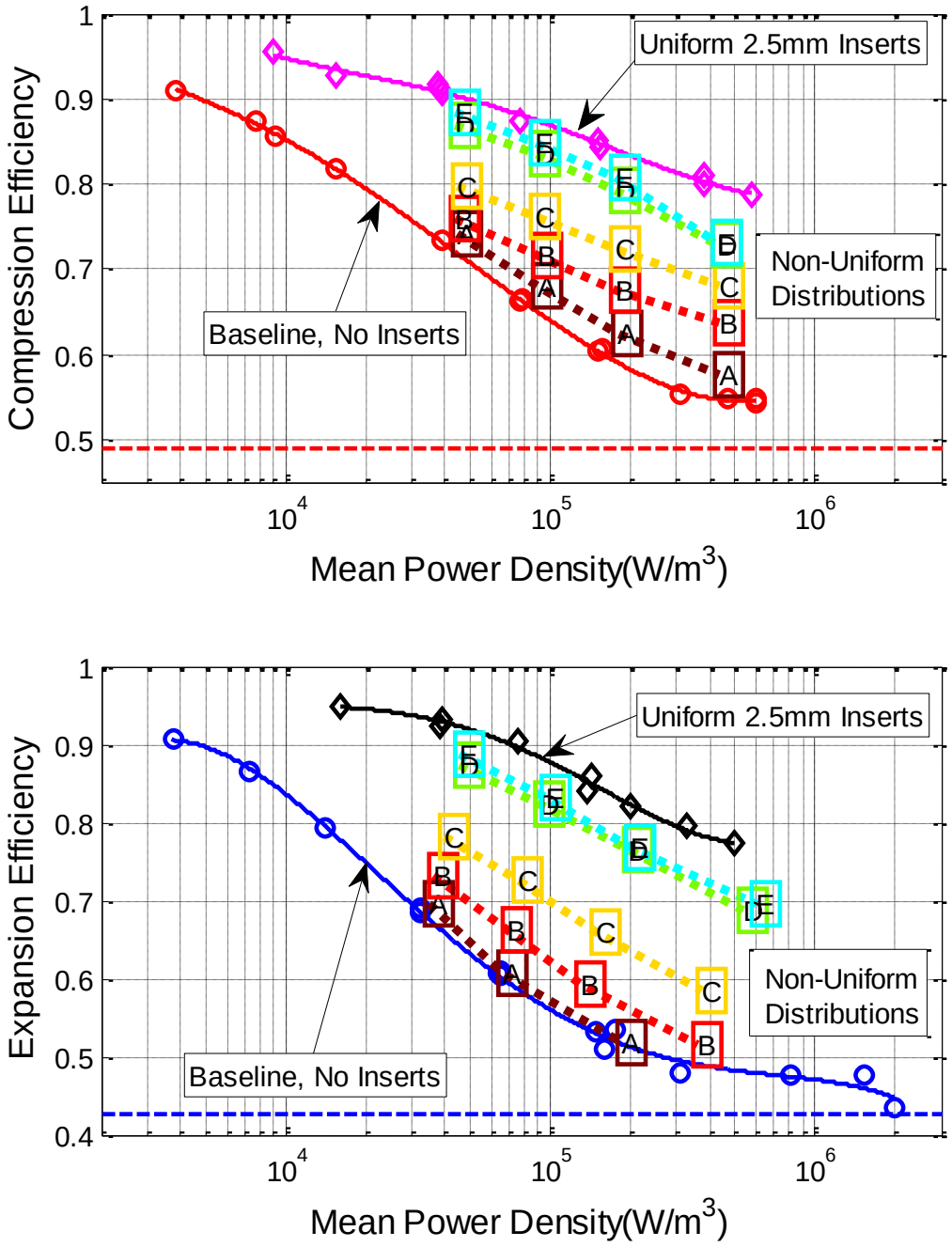

Fig. 5.4.9: Efficiency is plotted against mean power density for compression (top) and expansion (bottom). Baseline and uniform cases are denoted in the legend, non-uniform distributions are differentiated by letters corresponding to the five distributions.

Figure 5.4.9 shows efficiency plotted against power density for all of the tests discussed in this thesis. Recall from Eqns. (3.11) and (3.12) that power density is the average stored or recovered power per cycle divided by the volume of the chamber (air and inserts). For all cases, efficiency decreases as power density increases. For a given efficiency, power density increases as the total surface area is increased. For a fixed amount of porous material, efficiency increases as the solid is moved up in the chamber. At 90% compression efficiency, the power density of cases with uniform inserts was 10 times higher than the baseline. At 80% compression efficiency, the power density of cases with uniform inserts was 20 times higher than the baseline. At 90% expansion efficiency, power density was increased by a factor of 17 and at 80% expansion efficiency the improvement in power density was by a factor of 27 with the use of porous inserts.

Figures 5.4.10 and 5.4.11 show the same efficiency data from Fig. 5.4.9, but plotted against an area-normalized power density. Both figures are an application Eqn. (3.13), where the power density from Eqns. (3.11) or (3.12) is divided by the specific surface area. For Fig. 5.4.10, the specific surface area used in the normalization is the specific surface area at maximum volume. For Fig. 5.4.11, the specific surface area used in the normalization is the power-weighted average specific surface area, given by Eqn. (5.2).

Figure 5.4.10 shows that the baseline case with no inserts and the case with a uniform distribution of 2.5mm interrupted plates collapse at low values of power per unit area(<200 W/m^2), but begin to diverge as the power per unit area is increased. The efficiency curve for the uniform distribution of porous media is higher than that of the baseline at the same power per unit area which suggests that the porous media increases

not only surface area, but *h* as well. The non-uniform cases do not collapse in Fig. 5.4.10, but this is expected because the specific surface area changes dramatically during the compression process for non-uniform distributions. Figure 5.4.11 shows the normalization using the power-weighted average specific surface area, as opposed to the specific surface area at maximum volume. For cases where the specific surface area does not change significantly throughout the process, there is little difference between the two normalizations, but for the non-uniform cases the difference is quite significant. In Fig. 5.4.11 even the non-uniform data collapse to approximately the same curve as the baseline and uniform cases. A collapse of the data suggests a strong correlation between the efficiency and the normalized value on the x-axis. The significance of this will be discussed further in Chapter 6, but, essentially, Fig. 5.4.11 shows that placing more surface area (porous media) in regions occupied by air during periods of high power (the top of the chamber) will improve power density and efficiency. The data seem to collapse better for compression cases than for expansion cases. Compression and expansion tests differ in that during constant compression rate tests, the instantaneous power is always increasing and the total surface area is always decreasing. Constant expansion tests are the opposite – instantaneous power is decreasing as surface area is increasing.

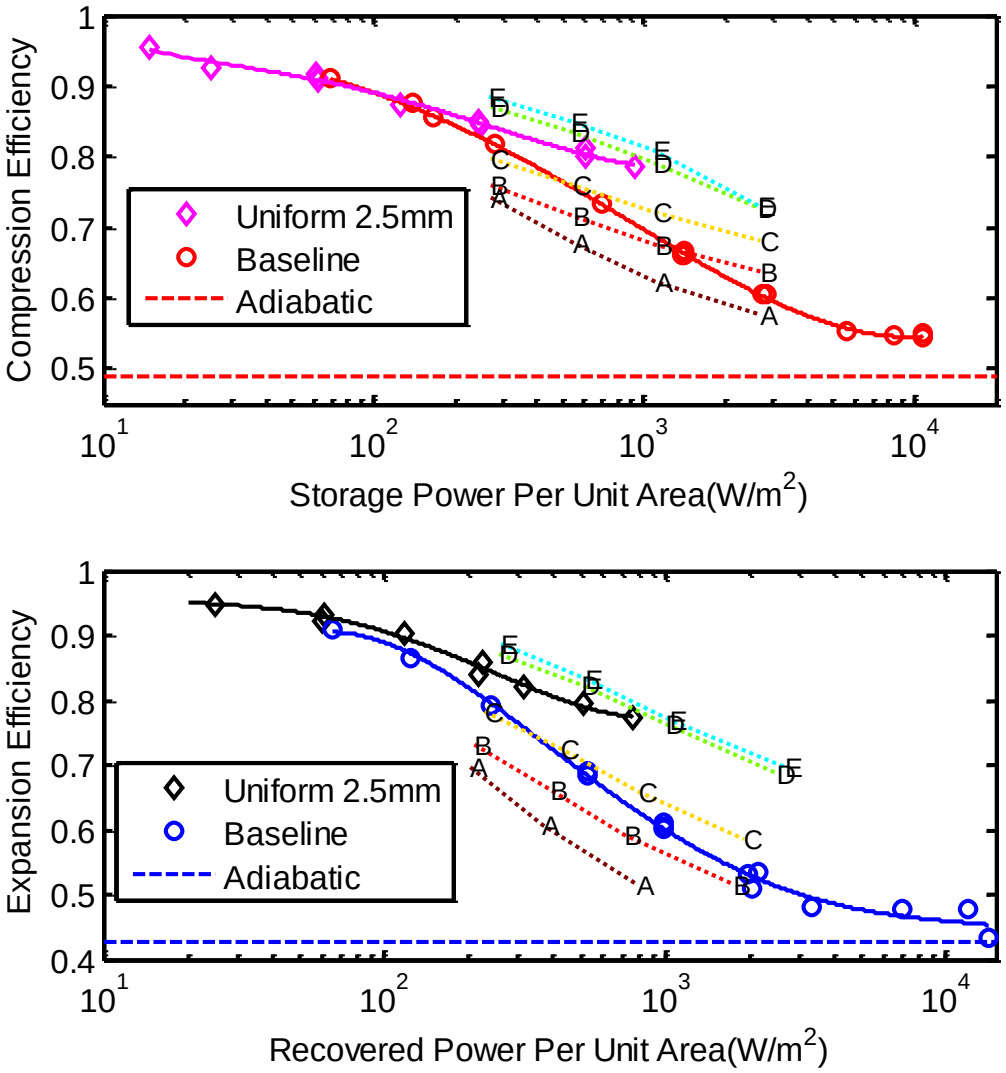

Fig. 5.4.10: Efficiency vs. Area-Normalized Power Density, initial specific surface area normalization. Compression (top) and expansion (bottom) efficiency are plotted against the mean power per unit area. Power densities given by Eqns. (3.11) and (3.12) are divided by the ratio of area to volume at maximum air volume. Baseline and uniform cases are marked as shown in the legend, non-uniform cases are marked with letters corresponding to the distribution used.

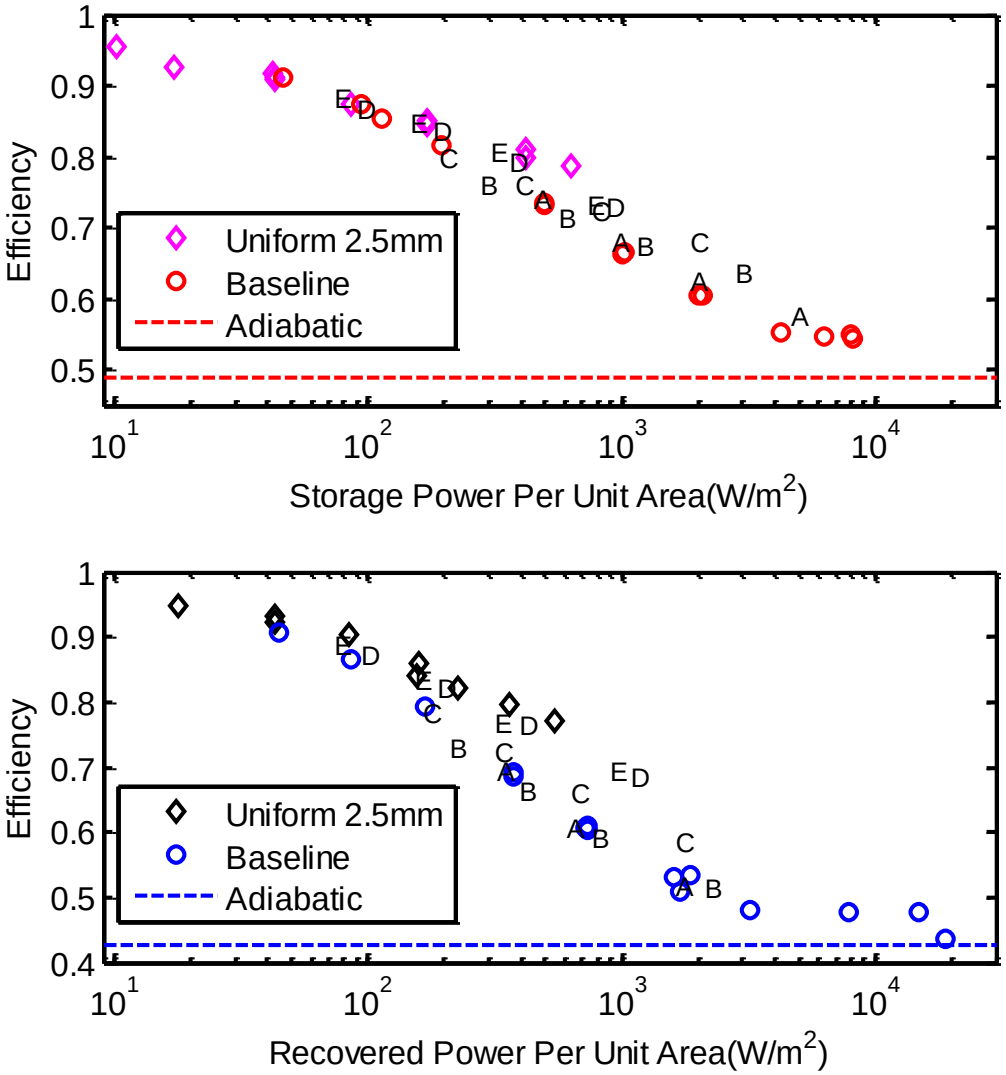

Fig. 5.4.11: Efficiency vs. Area-Normalized Power Density, power-weighted specific surface area normalization. Compression (top) and expansion (bottom) efficiency are plotted against the mean power per unit area. Power densities given by Eqns. (3.11) and (3.12) are divided by the power-weighted average specific surface area given by Eqn. (5.2) to give power per unit area, or area-normalized power density. Baseline and uniform cases are marked as shown in the legend, non-uniform cases are marked with letters corresponding to the distribution used.

Chapter 6: Discussion

6.1 Trends in the Data

One of the trends that is seen in all the data presented in Chapter 5, is a clear tradeoff between efficiency and power or power density. This trend is observed for the baseline (no media), uniform distribution, and all non-uniform distribution compression and expansion tests. If there is no constraint on the size of the compressor/ expander, then a trivial way to improve efficiency is to make the compressor/ expander very large or to run the process very slowly. Often, however, it is desirable for a compressor/ expander to be both energy efficient and power dense. While the tradeoff between efficiency and power was observed for every test, present experiments revealed that this tradeoff could be shifted toward higher power densities at the same efficiencies with the addition of surface area in the form of porous media inserts. Using a uniform distribution of porous media increased power density by approximately a factor of 30. In other words, an equal amount of energy could be stored or recovered in the same amount of time, but in a package size that is one-thirtieth the size.

Present experiments showed that the best location in the chamber for adding surface area is the region where the gas resides when the power is highest. For a constant compression rate, this happens to be the top of the chamber.

By normalizing the power density by the power-weighted specific area, all of the data approximately collapsed to a single curve in Fig. 5.4.11. This suggests that for a given efficiency, power density can be increased by increasing surface are in the chamber, particularly in regions where compression/ expansion power is high. The data collapsed

better for compression cases than for expansion cases. The main differences between compression experiments and expansion experiments are the trends in power and heat transfer rate. Figure 5.1.13 showed that for compression experiments, power and heat transfer increase together as the process progressed in time. Figure 5.1.14 showed that the expansion process tends to be power-dominated (near-adiabatic) at the beginning of the process and heat transfer-dominated from the middle to the end of the process. Figure 5.2.7 showed this same trend for expansion tests with a uniform distribution of interrupted plates.

It should also be noted that mean power has a slightly different definition for compression than for expansion. For compression, mean power is based on the amount of energy stored. This amount of energy is independent of the efficiency of the process. Thus, for the same flowrate, the power density is the same, regardless of the efficiency. For expansion, mean power is based on the amount of energy recovered, which depends on the efficiency of the process. Thus, expansion cases with the same flowrate will not necessarily have the same power density. This difference can most clearly be seen in Fig. 5.3.12. Notice how compression tests with the same flow rate, yielded mean powers that were approximately equal, regardless of efficiency. This is in contrast to expansion tests, where mean power decreases with efficiency at the same flow rate.

The power-weighted average specific area was found to be the best average specific surface area to normalize the data. Initially, it was not obvious which average specific area should be used in the normalization, so a number of weightings on area were considered: temperature, time, volume, instantaneous power, instantaneous power density, and instantaneous heat transfer. However, power-weighted average specific area was found to

collapse the data best. This follows from the first law of thermodynamics, which states that for the internal energy of the gas to remain constant, power must be balanced by the heat transfer rate.

Figure 5.4.11 shows that efficiency can be improved by reducing power, increasing the heat transfer coefficient, or by increasing surface area. Combining the information from Fig. 5.4.9 and that which is known about the different non-uniform distributions to develop Fig. 5.4.11 shows that for the same compression power density and the same total surface area, efficiency can be improved by moving surface area into high power regions of the compressor (the top). In Fig. 5.4.11, this is most clearly seen in the highest efficiency cases of distributions B, C, D, and E. For these three cases, the compression rate is the same, as are the initial volumes and surface areas. By moving the porous media into high power regions, the efficiency was significantly improved.

Figure 5.4.11 shows also that for the same efficiency, power density can be increased by some factor, α, provided that power-weighted average specific area is also increased by α. The porous inserts used in these experiments had average specific areas that were about twelve times those of the baseline (empty chamber) case. It is certainly possible to find porous materials with higher specific areas that would allow power density to be further increased for the same efficiency. Porous materials with average specific surface areas of fifty times that of the baseline case would not be too challenging to find. A thorough, systematic evaluation of a number of porous materials would be helpful for the design of a commercial liquid piston compressor/ expander, but that is out of the scope of the present work.

6.2 Heat Transfer Coefficient for an Insert of Uniform Geometry

The heat transfer coefficients for the uniform geometry insert cases were plotted in figures 5.2.8 and 5.2.9. Figure 5.2.9 showed that the data do not perfectly collapse when plotted against Reynolds number (based on half the piston velocity). Each case showed a "hook" near the end of the compression. This hook was in a favorable direction: the heat transfer coefficient increases sharply at the end of compression. There are a number of potential explanations for this, as follows.

The first explanation is based on the complex nature of heat transfer in a compressor. As discussed in [33], heat transfer in a compressor can be out of phase with the bulk temperature difference. This causes negative or infinite values of *h* when Newton's law of cooling is used. Physically, heat transfer depends on the temperature gradient at the wall. When a gas undergoes rapid compression, the temperature gradient near the wall becomes steeper as the compression process increases the gas temperature of the boundary layer. This steeper temperature gradient serves to enhance heat transfer from the gas to the wall. Hypothetically, flows could have the same Reynolds number and bulk temperature difference, but have different heat transfer coefficients because of the pressure effect on the near-wall temperature gradient. In general, this effect becomes more important as the compression rate is increased. Also, temperature, pressure, and thermophysical properties are continuously changing throughout the process.

The second explanation is that when the piston slows near the end of compression, the characteristic velocity of the air is no longer based on piston velocity, but some secondary flow velocity that has not been characterized. When the Reynolds number,

which is based on one half of the piston velocity, is divided by the square root of piston velocity, the heat transfer coefficients collapse to a linear relationship as seen in Fig. 6.2.1. Although the data collapse well, the physics of this are not obvious. A potential cause is that the velocity used in the Reynolds number is not really the proper characteristic velocity. This would be true if the velocity does not vary linearly from the piston surface to the top cap (i.e. there are significant secondary flows).

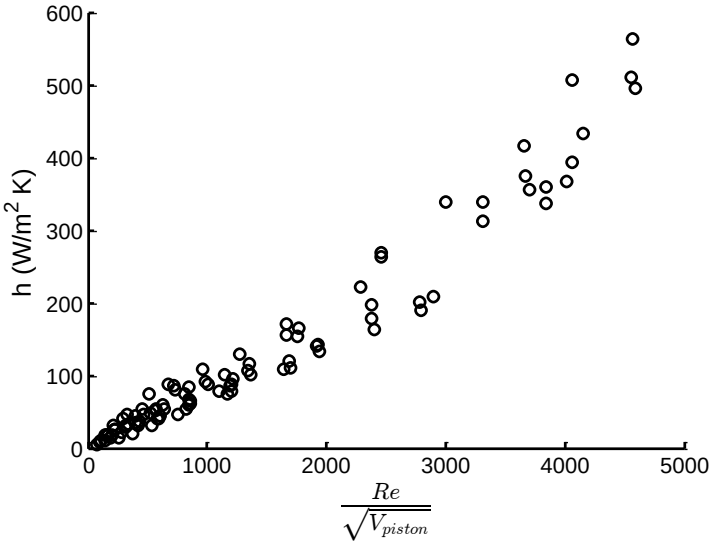

Fig. 6.2.1: Heat transfer coefficient plotted against Reynolds number over the square root of the piston velocity. The velocity is in units of m/s.

A third explanation, is that the velocity field depends on the aspect ratio (ratio of air column length to chamber diameter) in addition to the piston velocity. To test this hypothesis, Reynolds number is divided by the instantaneous aspect ratio. Figure 6.2.2 shows the results for all eleven of the uniform distribution insert cases. As the aspect ratio decreases, the surface areas on the top cap and on liquid interface make up a significant amount of the total heat transfer surface area. By normalizing the Reynolds number by the aspect ratio, the heat transfer coefficients from the end of the experiment are shifted to the

right and the heat transfer coefficients from the beginning of the experiment are shifted to the left. This normalization would make sense physically if the local Reynolds number did not very linearly from the piston to the top cap. The data collapse much better in Fig. 6.2.2 than when they were originally plotted as in Fig. 5.2.9. The piston velocity describes the primary aspects of the flow field, and it is believed that the aspect ratio somehow captures secondary flow characteristics. This is a bit surprising, because secondary flows were expected to be minimal with the presence of porous media. Relative to the method shown in Fig. 6.2.1, dividing by aspect ratio has the benefit that the number remains dimensionless.

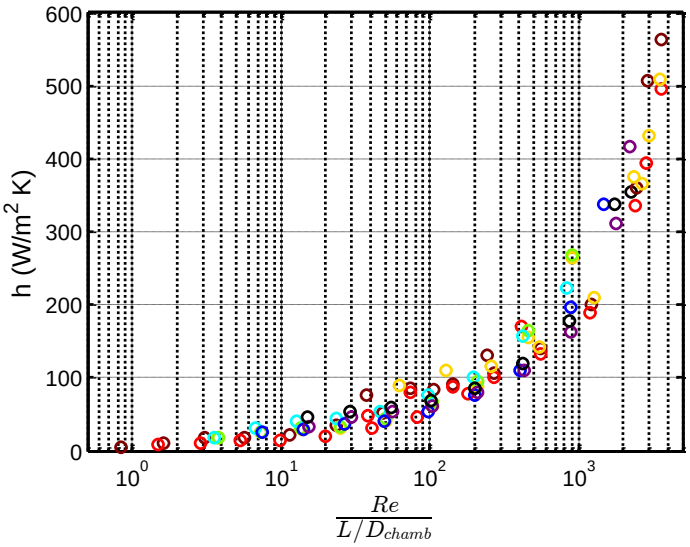

Fig. 6.2.2: Heat transfer coefficient plotted against Reynolds number, based on piston velocity and hydraulic diameter of insert, over instantaneous aspect ratio.

Additionally, it is fairly straightforward to compare experimental results with the CFD-based correlation for interrupted plate heat exchangers that was developed in [24]. The correlation is repeated here in Eqn. (6.1). This correlation was developed for a

representative elementary volume (REV) where the characteristic length scale for Reynolds number and Nusselt number is the hydraulic diameter of the interrupted plate.

$$Nu_{dh} = 9.7 + 0.0876\, Re_{dh}^{0.792} Pr^{(\frac{1}{3})} \tag{6.1}$$

Figure 6.2.3 shows the comparison between the experimental results with 2.5mm interrupted plates at constant flow rates and the heat transfer correlation from Eqn. (6.1). The comparison is based on the assumption that the characteristic velocity is one half of the piston velocity. This characteristic velocity comes from assuming that the air velocity varies linearly from the liquid piston interface to the top cap of the compressor, where it is zero. This assumption is reasonable, since the one dimensional formulation used in [25] showed a linear velocity distribution in the porous medium in a similar liquid piston compression event.

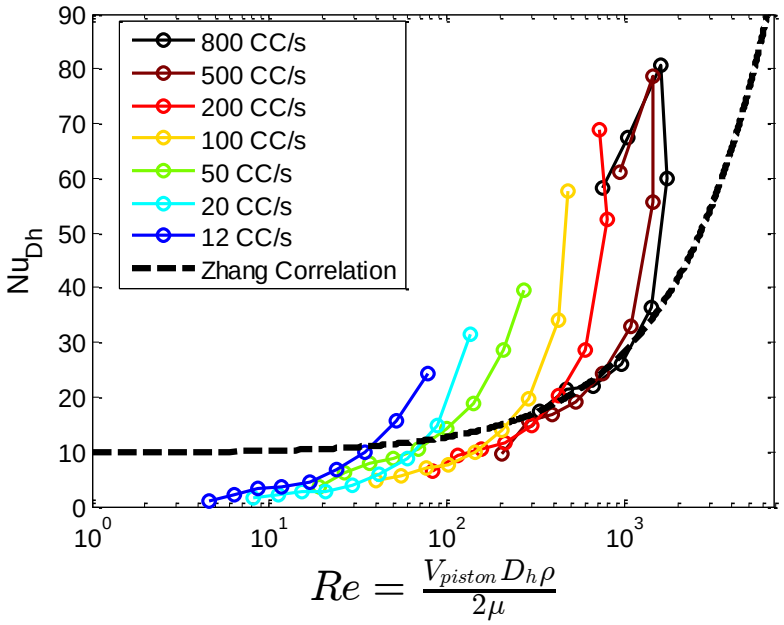

Fig 6.2.3: Comparison of heat transfer correlation with 2.5 mm interrupted plates constant flow rate experiments, using one half piston velocity as characteristic velocity. Pr=0.71. The legend indicates the compression rate of the experiment.

Unfortunately, the experimental results and the heat transfer coefficient correlation do not agree when this method is used. Not only this, but, as was previously shown, the experiments do not collapse at different compression rates. Figure 6.2.2 showed that the heat transfer coefficients for uniformly distributed interrupted plates collapsed to a single curve when the aspect ratio of the air column was taken into account. With this in mind, a new characteristic velocity, given by Eqn. (6.2), was used to better describe the flow in the compression chamber. The coefficient of 0.7 was found from a visual best-fit. Figure 6.2.3 plots the same data from Fig. 6.2.2 using this new characteristic velocity.

$$V_{char} = \frac{\frac{1}{2}V_{piston}}{0.7^{L}/_{D}} \tag{6.2}$$

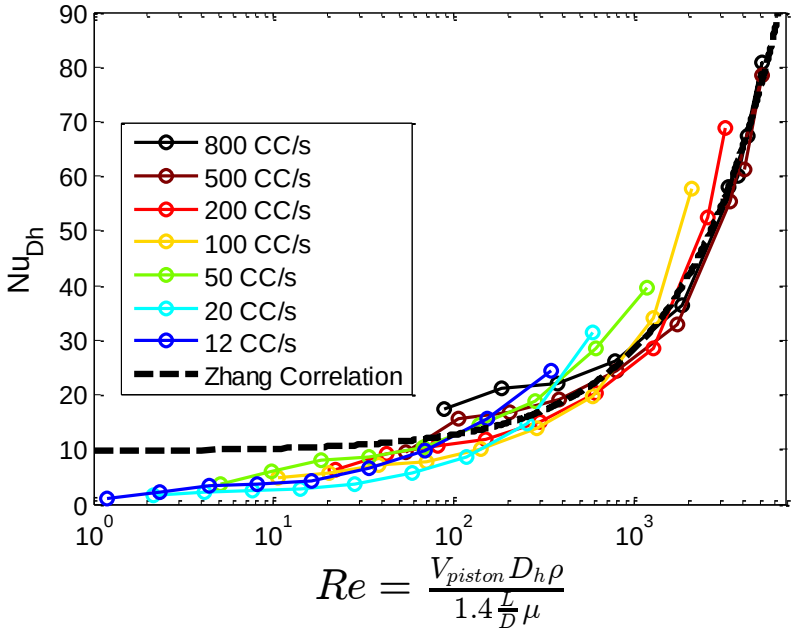

Fig. 6.2.4: Comparison of CFD-based correlation and experimental results. Characteristic length scale is the hydraulic diameter of the insert. Characteristic velocity of the experimental cases is taken to be the piston velocity over 1.4 times the aspect ratio. Correlation assumes Pr=0.71.

Overall, the correlation and the experiments are in agreement (within 25%) at high Reynolds numbers. At low Reynolds number there is more disagreement. The correlation

predicts a Nusselt number of 9.7 as Reynolds number goes to zero; however, experiments show that the Nusselt number tends toward one as Reynolds number goes to zero. At low Reynolds numbers (slow compression rates and low pressure), the driving temperature difference that is used to calculate the experimental heat transfer coefficient is generally small and the uncertainty in this temperature difference is relatively high. The lumped temperature model which is used for the porous medium, may underestimate the skin temperature of the porous medium, which would cause calculations of the heat transfer coefficient to be artificially low. Another item to note is that the CFD simulation models ideal, infinitely repeating geometry. The experimentally calculated heat transfer coefficient is based on a zero-dimensional model, which includes heat transfer to the side walls, top cap, liquid piston surface, and to interrupted plates which are not perfectly smooth, as in the simulation.

6.3 Comparison with other Results

It is difficult to make a make a direct comparison with other experimental results from the literature because of the large number of parameters that are different for each experimental setup: pressure ratio, chamber volume, initial pressure and temperature, compression frequency, compression trajectory, types of porous media (if any), number and type of spray/foam nozzles (if any), and more. Additionally, not all of this information is available from each of the relevant works that were considered. Table 5 summarizes some of the key information from the references that were discussed in Chapter 1.

Reference	Coney [18]	Shirazi, Saadat [11]	Rice [22]	Yan [27]
Volume (L)	11.0	0.30	0.45	0.71
L/D of Compressor	1.75	2.92	4.37	6.95
Method	Droplet Spray	Trajectory Control	Porous Media: Minitube, Metal Mesh	Porous Media: Metal Foam, Interrupted Plates
Pressure Ratio	25	10	7	10
Compression Time (s)	0.3 - 1.2	1.5 - 3	2 s	2 - 60
Approximate Power (W)	3-12 kW	20 - 50 W	25 W	2 - 90 W
Approximate Power Density (W/m^3)	2.7 E5 - 1.1 E6	7.7 E4 - 1.5 E5	5.6 E4	3.8 E3 to 1.8 E5
Key Results	28% savings in work input compared to adiabatic case	33% improvement in power density with optimal trajectory compared to constant flow	87% reduction in temperature rise compared to case with no porous media	10x increase in power density with porous media as compared to baseline case without at same efficiency of 95%

Table 5: Summary of experimental results from literature.

It is, however, possible to make qualitative comparisons with experiments that were conducted using a liquid piston compressor and porous media at low pressure [27]. Figure 6.3.1 plots the compression efficiency against power per unit area for these low pressure experiments, as was done in Fig. 5.4.11 for the experiments from this thesis. The efficiencies in the two figures should not be compared directly. The minimum efficiency, or adiabatic efficiency, is based on the pressure ratio used. For the experiments in Fig. 5.4.11, the pressure ratio was 30 and the minimum compression efficiency is 49%, while in Fig. 6.3.1 the pressure ratio is 10 and the minimum compression efficiency is 70%. Fig. 6.3.1 also incorporates the ejection work term into the efficiency definition, which tends to increase efficiency by approximately 2% and is not included in Fig. 5.4.11. The specific surface area definition used in Fig. 6.3.1 is the ratio of initial surface area to initial volume,

which is different than Eqn. (5.2). This difference is negligible when comparing cases with uniform distributions of porous media.

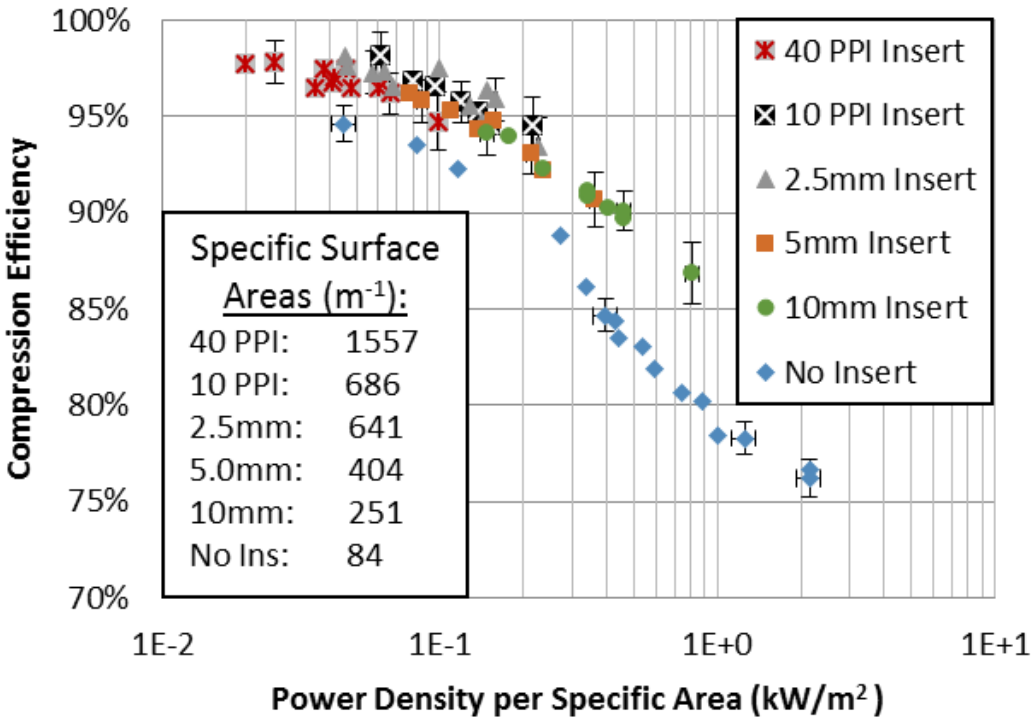

Fig. 6.3.1: Compression efficiency vs. storage power per unit area for liquid piston compressor operating from 1 to 10 bar. Porous media are indicated in the legend; specific surface areas are indicated in the textbox. Data from [27] and additional experiments completed by this author.

Despite these differences, the trends are remarkably similar. For both figures, the data collapse where the efficiency is high. In Fig. 5.4.11, this was true for the uniform 2.5 mm distribution, the baseline case, and distributions E and D, where the porous medium was near the top of the chamber. In Fig. 6.3.1, all of the insert cases, which are uniform distributions, collapse when efficiency is high. The no insert cases are slightly lower in efficiency and do not collapse perfectly. In both figures, the no insert cases diverge from the uniform distribution cases as power per unit area increases. This divergence begins

around 200 W/m^2. Both figures support the notion that compression performance is enhanced with porous media and that for a fixed efficiency, power can be increased by some factor, provided that the in-cylinder surface area is increased by the same factor.

Finally, experiments were compared with a one dimensional simulation of liquid piston compression, written by M. Saadat [34]. This code simulates the chamber and insert geometries that were used in the compression experiments with uniformly distributed 2.5 mm interrupted plates. The air volume is discretized into twenty nodes which compress with the bulk air volume. Real gas air properties from [30] are used. The simulation assumes a uniform pressure field, calculates the heat transfer coefficient using Eqn. (6.1), Zhang's correlation for interrupted plates [24], and solves the energy equation for each node. The simulation is run at constant flow conditions that vary from 2 cc/s to 10,000 cc/s. Figure 6.3.2 shows the comparison between experimental and simulation efficiency, plotted against compression time. The simulation and experimental results exhibit the same trend, and are in agreement for short compression times; however, for long compression times the simulation tends to under predict compression efficiency by 2-5%.

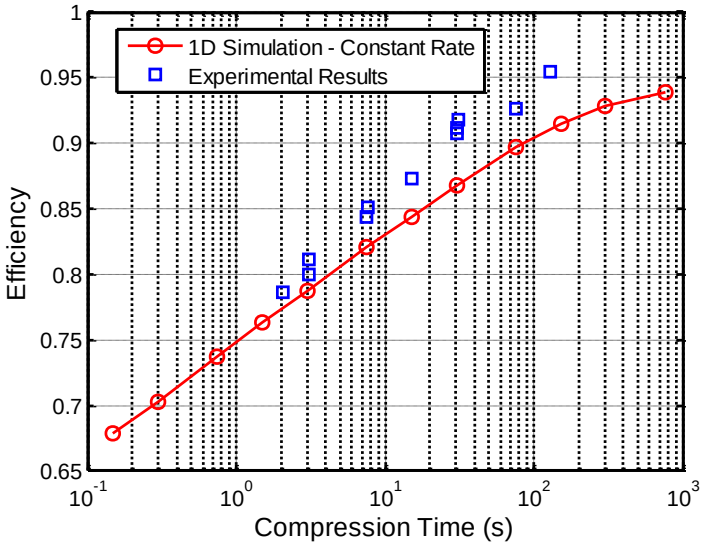

Fig. 6.3.2: Comparison between one-dimensional simulation and experiments with constant flow rate and uniformly distributed 2.5 mm interrupted plates.

Figure 6.3.3 compares the simulated and the experimental temperature trends for two flow conditions: 50 cc/s and 500 cc/s. The temperatures are in agreement for most of the compression, but at the end of the process the simulation temperature rises steeply. The simulation includes calculations for heat transfer between the air and the porous medium, air and the top cap, conduction within the porous medium, and heat transfer between the porous medium and the liquid piston. However, the simulation takes a conservative approach and does not model heat exchange to the compressor side walls. The additional heat transfer provided by this surface, may account for the discrepancy in temperature between the experiments and simulations at the end of compression as well as the lower efficiency of the simulation.

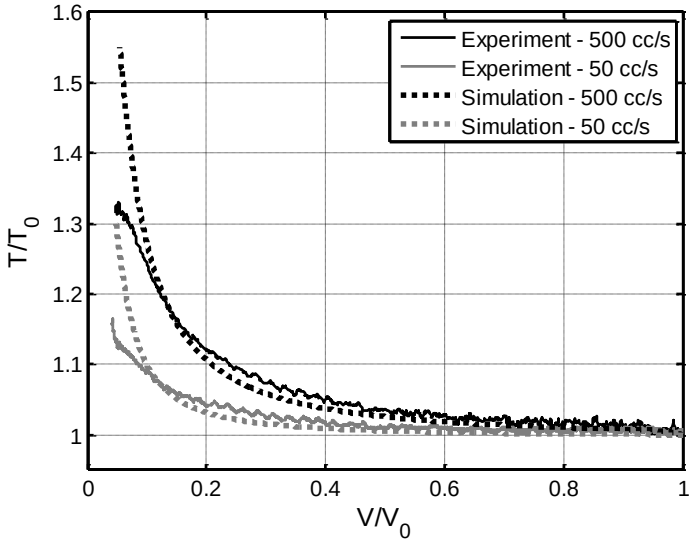

Fig. 6.3.3: Temperature plotted against volume for two experiments and the corresponding simulation with constant flow rate and uniformly distributed interrupted plate inserts. Simulation temperature is the "mixing cup" bulk temperature.

Figure 6.3.4 provides a comparison between the experimental heat transfer coefficients (given by Eqn. (5.1)) and the volume-averaged heat transfer coefficients from the one-dimensional simulations. These are the same cases that are plotted in Fig. 6.3.3: simulations and experiments at compression rates of 50 cc/s and 500 cc/s. Figure 6.3.4 shows that the simulated heat transfer coefficient is greater than the experimental value early in the compression process, but lower than the experimental value near the end of the compression process. This is consistent with Fig. 6.2.3 which showed that the heat transfer coefficient correlation tended to over predict Nusselt number for low Reynolds numbers, but under predict Nusselt number for high Reynolds number. All four of the cases compared tend to be relatively isothermal and have a temperature rise less than 10% of the initial temperature for the first 80% compression. These relatively small temperature differences cause h to be very sensitive to errors in absolute temperature. In fact, the calculated values of h for 500 cc/s experiment and simulation (which have a larger ΔT)

tend to be much closer than the 50 cc/s cases. Although there are large discrepancies in the calculated values of *h* for experiments and simulation, it is not unreasonable considering the small ΔT.

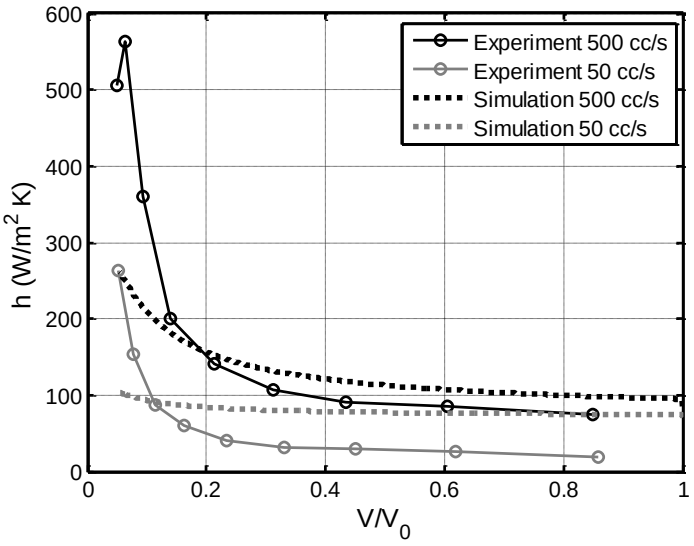

Fig. 6.3.4: Comparison of heat transfer coefficients for two constant flow experiments with a uniform distribution of 2.5mm interrupted plates and two one-dimensional simulations. The experimental values for *h* are found from Eqn. (5.1). The simulation value for *h* is the volume-averaged heat transfer coefficient.

Finally, Fig. 6.3.5 shows the Nusselt number – Reynolds number plot for all of the one dimensional simulations. This figure can be directly compared with Fig. 6.2.3, which is a similar plot for the corresponding experiments. Both figures show a deviation from the correlation, but they deviate in different ways. The experimentally measured values for heat transfer coefficient tend to increase and hook upward from the correlation at high Reynolds numbers. The volume-averaged heat transfer coefficients of the one-dimensional simulations tend to hook downward at high Reynolds numbers.

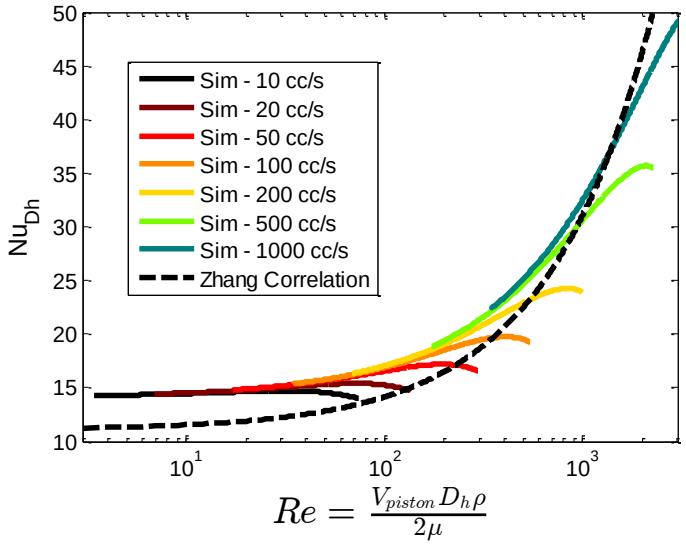

Fig. 6.3.5: Nusselt number vs. Reynolds number for one-dimensional simulations of constant compression and uniform distribution of 2.5mm interrupted plates. Legend indicates compression rate. Nusselt number is based on the volume-averaged heat transfer coefficient. Correlation from [24] (Eqn. (6.1)) and assumes constant Pr=0.71.

6.4 Implications for Design and Future Research

6.4.1 Model Validation

One of the stated goals for this thesis was to provide experimental data for compression and expansion under relatively high compression pressure ratios (30) and relatively high pressures (210 bar). These data can be used by researchers in future investigations. For example, a general model of the liquid piston compressor/ expander can be created. If the model is run under the same conditions as explained in this thesis, then the results from the model should agree with the experimental results. This thesis has provided a number of conditions to evaluate behavior: fast and slow cases, compression and expansion cases, with or without inserts, and uniform or non-uniform distributions of solids in the porous material. This thesis has also presented a variety of results that can be used for validation: pressure-volume curves, temperature-volume curves, temperature changes vs.

compression/ expansion time, efficiency vs. power density, and efficiency vs. area-normalized power density. All of the experimental data will be included digitally with this thesis if more detailed data are required for comparison. Once a model has been validated, it can be used in a variety of useful simulations.

6.4.2 Porous Media Considerations

Because of the clear difference between different non-uniform distributions of porous media, it is desirable to determine the optimal distribution of porous media for a given set of constraints. For these experiments, relatively narrow constraints were imposed, and distribution E (medium at the top) was found to be the best for both compression and expansion. Future work could compare a model-based optimization against these experiments. If the same constraints were imposed, one would expect similar results as the experiments. Even more interesting, would be the results of a general optimization with relaxed constraints.

From these experiments it is clear that increasing the power-weighted average specific area improves performance. It is also clear that leaving even a small gap at the top of the chamber for valves, nozzles, or instrumentation will reduce efficiency. In summary, we have learned that increasing surface area improves performance and moving the surface area to regions where the gas resides during high power operation improves performance further. Future research efforts should focus on the design of the porous media and their distribution in the chamber. Other geometries with fine features and higher specific areas should be investigated.

6.4.3 Optimal Compression/ Expansion Rate and Spray/Foam Injection

Two questions that are specifically related to this system remain unanswered. The first question is "how much of an improvement can be realized with an optimal compression rate in this high pressure system?" For low pressure experiments in a different facility, a 33% improvement in power density was realized [11], but the answer to the question for this system is not fully known as of the writing of this thesis. The second question that remains is "how much of an improvement can be realized with droplet spray or foam injection?" This question is less straightforward to answer because the number of nozzles, the location of the nozzles in the compression/ expansion chamber, the type of nozzle, and the injection timing are also important parameters. As discussed in the introduction, high efficiencies with droplet spray and foam injection have been reported in the academic literature as well as in commercial whitepapers, but this question is far from being definitively answered.

6.4.5 Liquid Piston Advantages

A liquid piston provides several of advantages over a solid piston and these advantages should be leveraged to the fullest extent possible in a compressor/ expander design. The first advantage is that a liquid piston allows for the addition of porous media heat exchangers. While deformable porous media can be used with a solid piston [22], a liquid piston permits the use of rigid, detailed, and highly optimized geometries. These geometries can be designed to maximize heat transfer, while minimizing water holdup and drag. The second advantage of a liquid piston over a solid piston is that it allows optimal compression/ expansion trajectories to be followed. This could be realized in a solid piston

system with an advanced mechanism design, but in a liquid piston it is as simple as controlling the flow rate. A liquid piston also eliminates leakage around piston rings and provides a low friction seal. Finally, a liquid piston permits the use of non-cylindrical compression/ expansion chambers. This is not so easy in a solid piston compressor. Non-cylindrical chambers allow for a more flexibility between compression rate and local air velocity in the porous medium. A conical compressor, with a large diameter base and small diameter top cap, would permit a near-uniform air velocity, as opposed to a velocity profile that varies linearly from the piston to the top. A gourd-shaped chamber would allow for high and low velocity regions, which may help balance the trade-offs between maximizing heat transfer and minimizing viscous losses. Other benefits may include cost or weight reduction, more effective water droplet injection, and reduced manufacturing costs due to looser tolerances. These three differences make a liquid piston unique, and they should be fully explored in future research and fully exploited in future designs.

6.4.6 Considerations for open-accumulator CAES system

For this thesis, the liquid piston compressor/ expander was analyzed as a stand-alone unit. When the compressor/ expander is integrated into an open accumulator CAES system [6], there are a number of other considerations. The CAES system presumably under design will include the addition of a low pressure or first stage compressor. Depending on the efficiency of the first stage, inter-stage heat exchange may be required to reduce the temperature of the charge air entering the second stage compressor. Both the low pressure and high pressure compressor/ expanders will require well-designed valves that allow high mass flow rates and do not add dead volume. Additional losses that were not considered in

this study, but that may be important in an energy storage system include: pressure drop in plumbing and porous media, pump and motor losses, valve losses, and inter-stage heat exchanger efficiency.

6.4.7 Other applications of quasi-isothermal compression/ expansion

Although compressed air energy storage was the focus of this thesis, there are other applications where isothermal compression or expansion would be valuable. Igobo and Davies present a review article on the application of quasi-isothermal expansion to low temperature vapor power cycle engines [34]. The use of quasi-isothermal expansion allows for a number of novel power cycles to be developed which are generally more efficient because the expansion is done isothermally rather than adiabatically. Quasi-isothermal Rankine cycles, Stirling cycles, and cryogenic heat engines are reviewed. In [35], a liquid nitrogen cryogenic engine is discussed in detail. This engine has an energy density that is comparable with batteries, a faster refill time than the recharge time for batteries, and zero emissions. A critical portion to this open Rankine cycle is the quasi-isothermal expansion. The authors discuss ways to realize this quasi-isothermal expansion by using heated fins in the cylinder head. If a liquid piston and porous media were incorporated in this engine, the efficiency and/or power density could likely be increased.

Additional applications include the industrial gas sector which produces and distributes a number of compressed gases. According to a leader in the industrial gas industry, “energy is the single largest cost item in the production and distribution of industrial gases” [36]. Reducing the energy cost associated with this compression process would likely be of great interest. Additionally, Eaton Corporation is developing an efficient

compressed natural gas (CNG) refueling station for home use that uses the liquid piston concept [37]. Eaton hopes to provide a charging station at a fraction of the cost of existing recharging stations. This would allow individuals to refuel CNG vehicles with low cost natural gas at their own home.

Chapter 7: Conclusion

Objectives of this thesis included providing experimental data at high pressures and high pressure ratios, evaluating the effectiveness of a liquid piston compressor using porous media, experimentally determining the optimal distribution of these porous media, and comparing these results with other published results.

To achieve these goals, an experimental facility was designed and constructed. Based on lessons learned from a previous test facility, care was taken to ensure accurate volume and pressure measurements. Because of the high pressures encountered, a real gas model for air was used and water compressibility was accounted. Compression and expansion tests with no inserts, constant flow rates, and a nominal pressure range of 7-210 bar established a baseline for comparison. Additional tests were conducted with uniform and non-uniform distributions of interrupted plate heat exchanger inserts.

These experiments found that the addition of porous media drastically improved compression and expansion efficiency and power density. Compared to the baseline, the uniform distribution improved compression power density by a factor of 20 and expansion power density by a factor of 27 at the same efficiency, 80%. At the highest power densities, compression efficiency was increased from 54.4% to 78.7% and expansion efficiency was increased from 48.0% to 77.2%, using a conservative definition of efficiency. When ejection work is included in the efficiency calculation, then at the highest power densities, compression efficiency was increased from 62.8% to 84.0% and expansion efficiency was increased from 63.5% to 84.0%.

The tests with non-uniform distributions showed that even a relatively small amount of porous media placed in the right location can make a big difference. When the surface area was placed at the top of the chamber, compression or expansion performance was nearly as high as for the uniform distribution case and when the surface area was placed at the bottom of the chamber, compression or expansion performance was nearly as low as for the baseline case with no insert.

These results showed that the mean power density divided by the power-weighted specific area is a good parameter for predicting the compression or expansion efficiency. This parameter combines the compressor/ expander size, compression/ expansion time, and the amount and distribution of porous media into one factor. By increasing the total amount of surface area and placing it in regions in which the gas resides during high power operation of the compressor/ expander, power density can be increased without reducing efficiency. In this study only one type of porous medium was considered, but many different kinds of porous media could be used to improve performance. In short, the combination of a liquid piston and a porous medium is an excellent candidate for power dense and efficient compressor/ expanders.

A characteristic velocity equal to half the piston velocity and a characteristic velocity that accounts for the aspect ratio of the compressor were considered. It is not clear which of these two velocities is better for characterizing the heat transfer in a liquid piston compressor using a zero-dimensional model. Initially, half the piston velocity was believed to be the best choice, this follows from the assumption a uniform pressure field and is supported with one-dimensional CFD simulations; however, there appears to be some

dependence on the instantaneous aspect ratio as well. When the aspect ratio is not included, the experimental heat transfer coefficients are higher than the heat transfer coefficient correlation they were compared against. When the aspect ratio is taken into account there is good agreement between a CFD-based correlation for heat transfer coefficient and the experimental results when operating at higher Reynolds numbers (50 – 5000). At Reynolds numbers less than 30, the CFD correlation predicts higher Nusselt numbers than are measured experimentally.

This thesis showed significant improvement in performance when porous inserts were used; however, only one type of insert was considered and the studies of the optimal distribution were highly constrained. A porous insert with high specific area that has been optimized in a more general way would be extremely useful to test experimentally and to use in a compressor design. Future work should also evaluate the optimal trajectory that was discussed in section 4.6. The use of spray and/or aqueous foam should also be considered, but a thorough investigation should investigate the number and type of nozzles, droplet injection timing, and mass loading. Finally, since this thesis focused on a CAES application, this liquid piston compressor/ expander should be incorporated into a pilot-scale demonstration system.

References

[1] U.S. Energy Information Administration, "EIA - Electricity Data," June 2014. [Online]. Available: http://www.eia.gov/electricity/monthly/current_year/june2014.pdf. [Accessed 22 July 2014].

[2] National Renewable Energy Laboratory, "Renewable Energy Futures Study (Entire Report)," Golden, 2012.

[3] U.S. EPA, "Carbon Dioxide Emissions - Climate Change - US EPA," 2014. [Online]. Available: http://www.epa.gov/climatechange/ghgemissions/gases/co2.html. [Accessed 22 July 2014].

[4] Minnesota Office of the Revisor of Statutes, *Minnesota Statute . §216B.1691,* St. Paul, 2013.

[5] United States Department of Energy, "DOE Global Energy Storage Database," 2014. [Online]. Available: http://www.energystorageexchange.org/. [Accessed 22 July 2014].

[6] P. Y. Li, E. Loth, T. Simon, J. D. Van de Ven and S. D. Crane, "Compressed Air Energy Storage for Offshore Wind Turbines," in *International Fluid Power Exposition*, Las Vegas, 2011.

[7] H. Ibrahim, A. Ilinca and J. Perron, "Energy storage systems—Characteristics and Comparisons," *Renewable and Sustainable Energy Reviews,* vol. 12, pp. 1221-1250, 2008.

[8] E. Drury, P. Denholm and R. Sioshansi, "The Value of Compressed Air Energy Storage in Energy and Reserve Markets," 4 May 2011. [Online]. Available: http://www.nrel.gov/analysis/pdfs/drury_coopt_caes_050411.pdf. [Accessed 2014].

[9] B. Li, *The Economic Performance of the Ocean Compressed Air Energy Storage - MS Thesis,* Raleigh: North Carolina State University, 2013.

[10] P. Denholm and R. Sioshansi, "The value of compressed air energy storage with wind in transmission-constrained electric power systems," *Energy Policy,* vol. 37, pp. 3149-3158, 2009.

[11] F. A. Shirazi, M. Saadat, B. Yan, P. Li and T. Simon, "Iterative Optimal and Adaptive Control of a Near Isothermal Liquid," in *Proc. of American Control Conference*, Washington, DC, 2013.

[12] H. Sun, *Research on a New Hybrid Wind Turbine System - PhD Dissertation,* Birmingham: University of Birmingham, 2014.

[13] A. O. Converse, "Seasonal Energy Storage in a Renewable Energy System," *Proceedings of the IEEE,* vol. 100, no. 2, pp. 401-409, 2012.

[14] J. D. Lewins, "Optimizing an Intercooled Compressor for Ideal Gas Model," *International Journal of Mechanical Engineering Education,* vol. 31, no. 3, pp. 189-200, 2003.

[15] G. Grazzini and A. Milazzo, "A Thermodynamic Analysis of Multistage Adiabatic CAES," *Proceedings of the IEEE,* vol. 100, no. 2, pp. 461-472, 2012.

[16] C. Qin, E. Loth, P. Y. Li, T. W. Simon, J. D. Van de Ven, S. Crane and A. Pourmosa, "Spray-Cooling for Wind-Based Compressed Air Energy Storage," in *AIAA 11th International Energy Conversion Engineering Conference,* San Jose, 2013.

[17] C. Qin and E. Loth, "Liquid piston compression efficiency with droplet heat transfer," *Applied Energy,* vol. 114, pp. 539-550, 2014.

[18] M. W. Coney, P. Stephenson, A. Malmgren, C. Linnemann and R. E. Morgan, "Development Of A Reciprocating Compressor Using Water Injection to Achieve Quasi-Isothermal Compression," in *International Compressor Engineering Conference*, 2002.

[19] LightSail Energy, "Technology - LightSail Energy," 2013. [Online]. Available: http://www.lightsail.com/. [Accessed 21 July 2014].

[20] T. McBride, A. Bell and D. Kempshire, "ICAES Innovation: Foam-based heat exchange - SustainX Whitepaper," Seabrook, 2013.

[21] C. Sancken and P. Li, "Optimal Efficiency-Power Relationship for an Air Motor/Compressor in an Energy Storage and Regeneration System," in *Proc. ASME Dynamic Systems and Control Conference*, Hollywood, 2009.

[22] A. T. Rice, *Heat Transfer Enhancement in Cylindrical Compression Chamber by Way of Porous Inserts and the Optimization of Compression and Expansion Trajectories for Varying Heat Transfer Capability - MS Thesis*, Minneapolis: University of Minnesota, 2011.

[23] M. Saadat, P. Y. Li and T. Simon, "Optimal Trajectories for Liquid Piston Compressor/ Expander in a Compressed Air Energy Storage System with Consideration of Heat Transfer and Friction," in *2012 American Control Conferenece*, Montréal, 2012.

[24] C. Zhang, F. A. Shirazi, B. Yan, T. W. Simon, P. Y. Li and J. D. Van de Ven, "Design of an interupted - plate heat exchanger used in liquid piston compression chamber for compressed air energy storage," in *Proceedings of the ASME 2013 Summer Heat Transfer Conference*, Minneapolis, 2013.

[25] C. Zhang, T. W. Simon and P. Y. Li, "Optimization of the axial porosity distribution of porous inserts in a liquid-piston gas compressor using a one-dimensional formulation," in *Proceedings of the ASME 2013 International Mechanical Engineering Congress and Exposition*, San Diego, 2013.

[26] B. Yan, J. H. Wieberdink, F. A. Shirazi, P. Li, T. Simon and J. D. Van de Ven, "Experimental Study of Heat Transfer Enhancement in a Liquid Piston Compressor/ Expander for Compressed Air Energy Storage Using Porous Inserts," *Unpublished*, 2014.

[27] B. Yan, *Compression/expansion within a cylindrical chamber: Application of a liquid piston and various porous inserts - MS Thesis,* Minneapolis: University of Minnesota, 2013.

[28] National Institute of Standards and Technology, "NIST ITS-90 Thermocouple Database," National Institute of Standards and Technology, 25 July 2013. [Online]. Available: http://srdata.nist.gov/its90/main/.

[29] J. D. Van de Ven and P. Y. Li, "Liquid Piston Gas Compression," *Applied Energy*, vol. 86, no. 10, pp. 2183-2191, 2009.

[30] E. W. Lemmon, R. T. Jacobsen, S. G. Penoncello and D. G. Friend, "Thermodynamic Properties of Air and Mixtures of Nitrogen, Argon, and Oxygen From 60 to 2000 K at Pressures to 2000 MPa," *Journal of Physical and Chemical Reference Data,* vol. 29, no. 331, 2000.

[31] D. Green and R. Perry, Perry's Chemical Engineer's Handbook, New York: McGraw Hill, 2007.

[32] E. Trostmann and B. Froelund, Tap Water as a Hydraulic Pressure Medium, CRC, 2000.

[33] A. A. Kornhauser and J. J. Smith, "Application of a Complex Nusselt Number to Heat Transfer During Compression and Expansion," *Transactions of the ASME,* vol. 116, pp. 536-542, 1994.

[34] M. Saadat, *Personal Correspondence,* 2014.

[35] O. N. Igobo and P. A. Davies, "Review of low-temperature vapour power cycle engines with quasi-isothermal expansion," *Energy,* vol. 70, pp. 22-34, 2014.

[36] C. Knowlen, J. Williams, A. T. Mattick, H. Deparis and A. Hertzberg, *Quasi-Isothermal Expansion Engines for Liquid Nitrogen Propulsion,* SAE Technical Paper 972649, 1997.

[37] Praxair, Inc., *2012 Annual Report,* Danbury, 2013.

[38] Eaton Corporation, "Eaton to Develop Affordable Home Refueling Station for Natural Gas Vehicles," 20 July 2012. [Online]. Available: http://www.eaton.eu/Eaton/OurCompany/NewsEvents/NewsReleases/PCT_378453. [Accessed September 2014].

Appendix A: Design Calculations

Final Design Safety Factors and Assumptions		
Total Axial Load (3200 psi on 3.94" diameter piston)	40	kip
Load Each Side Must Support	20	kip
Max Friction Hold on Oil Side Per Side	36	kip
Assumes: 6 bolts with 8 of 13 thread engagement torque to 900 in-lb using lubrication (k=0.15), mu=0.5		
Internal Thread Shear Stress	17.4	ksi
External Thread Shear Stress	25	ksi
Internal Thread Safety Factor	1.8	
External Thread Safety Factor	2.1	
Slipping Safety Factor	1.8	
Max Friction Hold on Water Side Per Side	39.2	kip
Assumes: 7 bolts with 5 of 13 thread engagement torque to 700 in-lb using lubrication (k=0.15), mu=0.6, 23 ksi allowable shear in internal threads		
Max Internal Thread Shear Stress	22	ksi
Max External Thread Shear Stress	31	ksi
Internal Thread Safety Factor	1.0	
Low safety factor; however, bolts were torqued to 900 in-lb in an assembly test without observable damage to internal threads. Likely the stainless steel threads have been work hardened.		
External Thread Safety Factor	1.7	
For bolts with more thread engagement: 6, 7 threads, respectively		
Internal Thread Safety Factor, 6 threads engaged	1.3	
External Thread Safety Factor, 6 threads engaged	2.0	
Internal Thread Safety Factor, 7 threads engaged	1.5	
External Thread Safety Factor, 7 threads engaged	2.3	
Slipping Safety Factor	2.0	

Appendix B: Table of Experimental Data

Test Name	Time (s)	P0 (bar)	V0 (CC)	T0 (K)	Rho0 (kg/m^3)	Vf (CC)	Viso,f (CC)	Max Temp Change (K)	Integral of PdV (J)	Cooling Work (J)	Low Press. Work (J)	Integral of Isothermal PdV (J)	Isothermal Low Press. Work (J)	Eqn. (3.6) Efficiency	Peak Power (W)	Power-Averaged Specific Area (1/m	Rate (CC/s)	Compression / Expansion	Case/ Distribution	Mean Power (W)	Mean Power Density (W/m^2)	Area-Normalized Power Density (W/m^2
Comp-5	428.4	6.9	2241	300.2	8.0	90.3	77.8	43	5251	257	1484	5147	1484	91.03%	110	83	5	Compression	Baseline	8.5	3.82E+03	46.1
Comp-10	213.7	6.9	2241	300.5	8.0	96.9	77.9	64	5302	392	1491	5169	1491	87.51%	213	82	10	Compression	Baseline	17.2	7.68E+03	94.1
Comp-12	178.2	6.9	2248	292.3	8.2	99.9	77.7	72	5343	459	1495	5179	1495	85.52%	278	81	12	Compression	Baseline	20.7	9.20E+03	113.7
Comp-20	106.6	6.9	2248	291.6	8.3	106.9	77.7	94	5414	604	1499	5192	1499	81.71%	467	80	20	Compression	Baseline	34.7	1.54E+04	193.0
Comp-50(1)	42.3	6.9	2249	293.4	8.2	123.8	77.8	152	5586	952	1499	5191	1499	73.27%	1037	78	50	Compression	Baseline	87.3	3.88E+04	499.8
Comp-50(2)	42.4	6.9	2248	293.4	8.2	122.2	77.7	147	5583	919	1493	5174	1493	73.49%	937	78	50	Compression	Baseline	86.8	3.86E+04	495.8
Comp-100(3)	21.0	6.8	2245	292.6	8.1	138.1	77.3	204	5732	1242	1476	5116	1476	66.21%	2075	76	100	Compression	Baseline	173.6	7.73E+04	1014.5
Comp-100(4)	21.0	6.9	2246	293.0	8.2	138.2	77.7	202	5774	1251	1495	5179	1495	66.62%	2053	76	100	Compression	Baseline	175.6	7.82E+04	1025.8
Comp-100(2)	21.0	6.8	2246	293.0	8.1	138.3	77.4	205	5737	1246	1478	5123	1478	66.21%	2073	76	100	Compression	Baseline	173.4	7.72E+04	1013.6
Comp-100(1)	21.1	6.8	2246	293.1	8.1	137.6	77.5	202	5752	1232	1481	5133	1481	66.37%	1766	76	100	Compression	Baseline	173.4	7.72E+04	1012.0
Comp-200	10.2	6.5	2213	298.0	7.6	154.5	75.6	277	5559	1547	1394	4846	1394	60.44%	3834	76	200	Compression	Baseline	337.6	1.53E+05	2018.0
Comp-200(2)	10.4	6.9	2240	300.7	7.9	155.1	77.8	275	5928	1593	1482	5139	1482	60.55%	4366	75	200	Compression	Baseline	351.3	1.57E+05	2095.7
Comp-400	5.2	6.8	2227	296.0	8.0	172.0	76.7	336	6003	1934	1454	5042	1454	55.35%	5776	74	400	Compression	Baseline	695.5	3.12E+05	4228.0
Comp-600	3.5	6.9	2228	296.3	8.1	175.3	77.1	347	6112	2025	1479	5121	1479	54.70%	7271	74	600	Compression	Baseline	1041.5	4.67E+05	6345.4
Comp-800(2)	2.7	6.7	2248	291.8	8.1	179.9	77.2	352	6038	2079	1465	5081	1465	54.36%	7438	73	800	Compression	Baseline	1343.3	5.98E+05	8203.9
Comp-800(1)	2.7	6.9	2228	297.0	8.1	173.6	77.1	343	6115	1989	1477	5116	1477	54.91%	7056	74	800	Compression	Baseline	1326.5	5.96E+05	8062.5
Comp-12	129.5	6.7	1628.0	293.9	8.0	62.8	56.0	29.9	3669.3	137.0	1061	3680.831	1061.0307	95.43%	298.81	883	12	Compression	Uniform, 2.5mm	20.2	8.94E+03	10.1
Comp-20	75.8	6.9	1591.8	290.5	8.2	62.5	54.9	33.7	3703.5	156.2	1054.8	3654.439	1054.8176	92.68%	557.68	903	20	Compression	Uniform, 2.5mm	34.3	1.54E+04	17.1
Comp-50(1)	30.4	6.9	1591.3	287.9	8.4	65.3	54.8	47.6	3710.4	217.2	1058.4	3662.172	1058.426	90.75%	967.73	902	50	Compression	Uniform, 2.5mm	85.8	3.85E+04	42.7
Comp-50(2)	30.4	6.9	1593.9	287.7	8.3	65.2	54.8	45.7	3697.2	214.0	1057.6	3659.503	1057.5863	91.18%	939.97	900	50	Compression	Uniform, 2.5mm	85.5	3.84E+04	42.6
Comp-50(3)	31.0	6.8	1627.7	293.0	8.0	67.3	56.0	49.6	3688.3	229.7	1062.1	3684.368	1062.1439	91.82%	1033.6	882	50	Compression	Uniform, 2.5mm	84.5	3.73E+04	42.3
Comp-100	15.2	6.9	1593.5	291.3	8.3	68.5	55.1	61.7	3781.7	276.8	1062	3678.11	1061.951	87.31%	1792.5	900	100	Compression	Uniform, 2.5mm	171.9	7.71E+04	85.7
Comp-200(1)	7.6	6.9	1592.5	287.5	8.4	71.9	54.8	76.7	3788.1	354.3	1058	3660.265	1057.9628	84.37%	2893.8	900	200	Compression	Uniform, 2.5mm	344.4	1.55E+05	171.8
Comp-200(2)	7.6	6.8	1593.3	286.8	8.3	72.3	54.6	78.2	3722.6	362.5	1049.8	3633.97	1049.8439	85.14%	2846.5	899	200	Compression	Uniform, 2.5mm	338.3	1.52E+05	168.9
Comp-500(1)	3.1	6.8	1582.5	291.2	8.2	75.0	54.5	96.3	3803.3	421.2	1045.6	3623.547	1045.5835	81.10%	5367.7	904	500	Compression	Uniform, 2.5mm	837.8	3.78E+05	417.8
Comp-500(2)	3.1	6.9	1593.2	287.6	8.4	77.7	54.9	103.7	3851.8	473.6	1061.7	3672.589	1061.7441	80.00%	5368.9	897	500	Compression	Uniform, 2.5mm	839.8	3.77E+05	419.9
Comp-800	2.1	6.9	1591.2	287.3	8.4	77.6	54.8	103.5	3898.9	472.0	1059.5	3664.874	1059.5321	78.68%	5976.1	899	800	Compression	Uniform, 2.5mm	1270.9	5.71E+05	635.2

Test Name	Time (s)	P0 (bar)	V0 (CC)	T0 (K)	Rho0 (kg/m^3)	Vf (CC)	Viso,f (CC)	Max Temp Change (K)	Integral of PdV (J)	Cooling Work (J)	Low Press. Work (J)	Integral of Isothermal PdV (J)	Isothermal Low Press. Work (J)	Eqn. (3.6) Efficiency	Peak Power (W)	Power-Averaged Specific Area (1/m	Rate (CC/s)	Compression / Expansion	Case/ Distribution	Mean Power (W)	Mean Power Density (W/m^2)	Area-Normalized Power Density (W/m^2
Comp-A-50	35.5	6.8	1891.5	300.4	7.9	101.4	65.6	143.5	4659.3	733.6	1246.1	4322.5	1246.1	74.19%	1307.8	99	50	Compression	A	86.6	4.43E+04	447.9
Comp-A-100	17.7	6.8	1891.5	300.7	7.9	113.0	65.6	191.2	4795.0	971.2	1244.4	4317.4	1244.4	67.96%	2644.4	97	100	Compression	A	174.0	8.90E+04	919.7
Comp-A-200	8.8	6.8	1891.5	301.0	7.9	123.7	65.6	241.1	4971.8	1188.0	1242.6	4312.0	1242.6	62.42%	3929.4	95	200	Compression	A	348.0	1.78E+05	1871.1
Comp-A-500	3.6	6.8	1891.7	301.1	7.9	133.4	65.5	284.3	5173.5	1384.4	1241.4	4308.3	1241.4	57.69%	6989.7	94	500	Compression	A	853.6	4.36E+05	4651.8
Comp-B-50	35.8	6.8	1890.3	298.2	8.0	101.4	65.4	143.2	4551.4	737.4	1246.5	4320.0	1246.5	76.03%	1236.6	157	50	Compression	B	85.8	4.39E+04	279.9
Comp-B-100	17.8	6.8	1890.0	298.5	8.0	110.7	65.5	182.1	4620.2	929.8	1248.0	4325.5	1248.0	71.54%	2756.6	156	100	Compression	B	173.0	8.85E+04	568.0
Comp-B-200	8.9	6.8	1891.2	299.4	8.0	119.0	65.6	221.4	4717.7	1096.9	1249.7	4332.6	1249.7	67.53%	3696.4	155	200	Compression	B	347.1	1.77E+05	1143.4
Comp-B-500	3.6	6.8	1891.7	299.8	8.0	127.0	65.6	253.8	4836.8	1263.0	1250.8	4336.9	1250.8	63.65%	6606.1	154	500	Compression	B	856.1	4.38E+05	2833.2
Comp-C-50	35.8	6.9	1890.7	299.2	8.0	98.0	65.6	131.7	4448.8	666.6	1251.4	4337.7	1251.4	79.87%	1205.5	229	50	Compression	C	86.1	4.40E+04	192.2
Comp-C-100	17.9	6.8	1890.8	299.2	8.0	104.9	65.6	158.2	4492.4	809.6	1250.1	4333.6	1250.1	76.10%	3164.7	230	100	Compression	C	172.7	8.83E+04	384.0
Comp-C-200	8.9	6.9	1891.0	299.4	8.0	111.6	65.6	184.9	4570.0	946.7	1251.1	4337.2	1251.1	72.35%	4017.4	232	200	Compression	C	345.6	1.77E+05	762.9
Comp-C-500	3.6	6.9	1891.2	299.6	8.0	118.1	65.6	216.9	4707.8	1080.2	1250.6	4335.7	1250.6	67.99%	6559.1	234	500	Compression	C	851.5	4.36E+05	1863.2
Comp-D-50	36.2	6.8	1892.5	299.5	8.0	84.6	65.6	74.4	4406.5	389.2	1249.6	4332.7	1249.6	86.94%	1506.7	484	50	Compression	D	85.3	4.36E+04	90.0
Comp-D-100	18.0	6.8	1892.5	299.0	8.0	89.0	65.6	94.1	4450.1	481.3	1247.7	4325.7	1247.7	83.56%	2598.5	485	100	Compression	D	170.6	8.72E+04	179.9
Comp-D-200	9.0	6.8	1892.5	298.8	8.0	93.8	65.5	113.9	4549.3	579.9	1246.1	4320.0	1246.1	79.16%	4189.7	486	200	Compression	D	341.0	1.74E+05	358.9
Comp-D-500	3.7	6.8	1892.5	299.2	8.0	99.7	65.6	137.4	4768.9	700.8	1247.5	4325.1	1247.5	72.89%	6601.6	490	500	Compression	D	837.5	4.28E+05	872.9
Comp-E-50	36.3	6.8	1893.0	299.3	8.0	79.4	65.6	53.4	4446.1	284.1	1247.6	4326.0	1247.6	88.39%	1253.7	592	50	Compression	E	84.9	4.34E+04	73.3
Comp-E-100	18.1	6.8	1893.5	297.7	8.0	83.6	65.5	70.2	4503.0	371.1	1248.4	4325.9	1248.4	84.88%	2393.7	587	100	Compression	E	170.0	8.68E+04	147.9
Comp-E-200	9.1	7.0	1894.9	297.7	8.1	88.5	65.9	88.0	4672.4	473.0	1272.6	4404.5	1272.6	80.87%	3779.0	582	200	Compression	E	345.7	1.76E+05	303.2
Comp-E-500	3.7	6.8	1893.2	297.1	8.0	93.9	65.4	114.7	4866.5	585.2	1248.5	4325.4	1248.5	73.20%	6553.7	583	500	Compression	E	841.1	4.30E+05	737.7

Test Name	Time (s)	P0 (bar)	V0 (CC)	T0 (K)	Rho0 (kg/m^3)	Vf (CC)	Viso,f (CC)	Max Temp Change (K)	Integral of PdV (J)	Low Press. Work (J)	Integral of Isothermal PdV (J)	Isothermal Low Press. Work (J)	Eqn. (3.7) Efficiency	Peak Power (W)	Power-Averaged Specific Area (1/m	Rate (CC/s)	Compression / Expansion	Case/ Distribution	Mean Power (W)	Mean Power Density (W/m^2)	Area-Normalized Power Density (W/m^2
Exp-5	414.3	209.9	78	306.4	227.8	2156.8	2236.7	33	4839	1460	5232	1510	90.81%	140	85	5	Expansion	Baseline	8.2	3.78E+03	44.7
Exp-10	207.1	210.0	78	303.7	230.5	2155.8	2231.1	47	4675	1456	5223	1507	86.66%	211	84	10	Expansion	Baseline	15.5	7.21E+03	85.4
Exp-20	101.5	210.0	79	302.1	232.5	2119.0	2285.5	67	4447	1428	5348	1544	79.36%	615	84	20	Expansion	Baseline	29.7	1.40E+04	166.9
Exp-50(2)	39.1	209.9	77	296.8	238.8	2045.1	2237.9	91	3972	1405	5227	1512	69.08%	1053	86	50	Expansion	Baseline	65.6	3.21E+04	374.1
Exp-50(1)	39.3	210.0	79	299.2	235.8	2053.5	2277.7	93	3993	1401	5326	1539	68.43%	1398	85	50	Expansion	Baseline	66.0	3.21E+04	376.4
Exp-100(2)	18.2	209.8	76	296.4	239.1	1910.2	2215.6	110	3522	1295	5174	1496	60.57%	2541	88	100	Expansion	Baseline	122.1	6.39E+04	722.5
Exp-100(3)	18.2	209.8	76	296.3	239.3	1907.8	2214.8	111	3525	1282	5171	1496	61.03%	2546	88	100	Expansion	Baseline	123.2	6.46E+04	729.7
Exp-100(1)	18.0	209.8	77	296.9	238.5	1890.6	2223.6	111	3503	1277	5193	1502	60.30%	1713	88	100	Expansion	Baseline	123.5	6.53E+04	738.5
Exp-200(2)	7.7	199.8	77	306.8	219.3	1639.5	2232.6	128	2959	1068	4990	1436	53.21%	3941	93	200	Expansion	Baseline	244.8	1.49E+05	1605.4
Exp-200(1)	7.5	210.0	77	296.7	238.9	1588.2	2243.3	137	2970	1069	5242	1516	51.04%	3573	93	200	Expansion	Baseline	253.5	1.60E+05	1716.1
Exp-200(3)	7.2	209.8	75	297.3	238.0	1516.3	2163.2	127	2913	994	5052	1461	53.42%	4708	95	200	Expansion	Baseline	268.1	1.77E+05	1861.0
Exp-300	4.3	210.0	77	302.5	232.0	1321.7	2214.7	151	2641	871	5184	1496	48.01%	3497	97	300	Expansion	Baseline	412.6	3.12E+05	3211.2
Exp-500	2.0	210.0	75	295.0	241.0	1080.1	2177.1	152	2436	708	5090	1472	47.76%	8164	101	500	Expansion	Baseline	868.0	8.04E+05	7920.4
Exp-800	1.2	209.9	73	291.5	244.3	957.0	2143.1	162	2309	610	5009	1448	47.71%	7987	104	800	Expansion	Baseline	1477.3	1.54E+06	14834.8
Exp-900	0.9	210.0	75	294.8	241.2	873.6	2189.8	178	2141	558	5120	1481	43.48%	12164	106	900	Expansion	Baseline	1744.8	2.00E+06	18863.4
Exp-20	73.4	209.6	54.9	292.7	242.9	1538.2	1601.0	17.7	3557.0	1036	3736.826	1080.23	94.90%	727.66	906	20	Expansion	Uniform, 2.5mm	34.3	1.58E+04	17.4
Exp-50(1)	29.5	209.8	54.8	296.2	239.4	1546.9	1595.3	30.0	3512.1	1042.4	3725.379	1077.4342	93.27%	1535.7	905	50	Expansion	Uniform, 2.5mm	83.6	3.83E+04	42.3
Exp-50(2)	29.4	209.7	54.5	291.9	243.7	1541.3	1590.6	31.9	3479.5	1040.1	3714.354	1073.7704	92.38%	1525.7	904	50	Expansion	Uniform, 2.5mm	82.9	3.81E+04	42.1
Exp-100	14.7	212.2	54.1	294.7	243.4	1539.3	1574.7	43.8	3437.2	1050.5	3717.163	1075.5834	90.35%	2639.8	904	100	Expansion	Uniform, 2.5mm	162.4	7.47E+04	82.6
Exp-200(1)	7.6	208.6	55.9	300.1	233.2	1558.1	1614.2	65.0	3288.3	1043.4	3753.171	1083.582	84.09%	2615.8	885	200	Expansion	Uniform, 2.5mm	297.3	1.36E+05	153.2
Exp-200	7.4	210.1	54.3	290.5	245.1	1544.2	1580.6	59.1	3302.9	1045.8	3696.524	1068.8415	85.90%	3809.2	904	200	Expansion	Uniform, 2.5mm	306.1	1.40E+05	155.3
Exp-300	5.1	209.9	55.2	298.1	237.0	1555.5	1600.6	71.4	3231.0	1049.5	3739.607	1081.041	82.06%	3064.1	885	300	Expansion	Uniform, 2.5mm	429.5	1.96E+05	221.5
Exp-500	3.0	210.1	54.4	290.4	245.2	1547.6	1585.5	78.5	3141.8	1044.9	3707.622	1072.0689	79.56%	6264.3	904	500	Expansion	Uniform, 2.5mm	708.9	3.25E+05	359.2
Exp-800	1.9	210.0	53.8	289.2	245.9	1547.5	1564.8	80.3	3051.2	1043.9	3656.312	1057.6259	77.24%	6347.7	905	800	Expansion	Uniform, 2.5mm	1061.5	4.86E+05	537.4

Test Name	Time (s)	P0 (bar)	V0 (CC)	T0 (K)	Rho0 (kg/m^3)	Vf (CC)	Viso,f (CC)	Max Temp Change (K)	Integral of PdV (J)	Low Press. Work (J)	Integral of Isothermal PdV (J)	Isothermal Low Press. Work (J)	Eqn. (3.7) Efficiency	Peak Power (W)	Power-Averaged Specific Area (1/m	Rate (CC/s)	Compression / Expansion	Case/ Distribution	Mean Power (W)	Mean Power Density (W/m^2)	Area-Normalized Power Density (W/m^2
Exp-A-50	33.8	210.0	64.9	303.4	230.9	1760.5	1862.9	92.9	3346.1	1184.8	4360.5	1258.5	69.67%	1254.2	108	50	Expansion	A	63.9	3.50E+04	325.5
Exp-A-100	16.2	210.2	64.6	303.4	231.2	1682.2	1856.4	114.7	3010.0	1132.9	4349.2	1255.4	60.67%	3836.5	109	100	Expansion	A	115.7	6.63E+04	609.1
Exp-A-200	6.3	209.9	64.7	303.9	230.3	1303.7	1857.0	139.7	2466.6	867.4	4346.3	1254.3	51.72%	5379.2	112	200	Expansion	A	252.7	1.85E+05	1644.6
Exp-B-50	34.2	209.8	65.0	302.2	232.3	1768.8	1871.1	91.7	3466.9	1191.0	4375.8	1263.2	73.12%	943.9	172	50	Expansion	B	66.6	3.63E+04	210.8
Exp-B-100	16.7	209.8	64.7	301.2	233.4	1724.7	1865.7	113.1	3215.9	1160.7	4363.2	1259.8	66.22%	1420.0	174	100	Expansion	B	122.9	6.87E+04	395.5
Exp-B-200	8.1	210.0	64.6	301.3	233.5	1670.7	1862.5	136.0	2959.6	1123.5	4357.9	1258.4	59.24%	2873.4	173	200	Expansion	B	227.7	1.31E+05	759.2
Exp-B-500	2.9	210.0	64.9	302.3	232.3	1486.1	1867.6	151.4	2594.0	994.9	4370.7	1261.7	51.43%	5306.2	169	500	Expansion	B	555.2	3.58E+05	2123.2
Exp-C-50	33.9	209.9	64.8	301.6	233.0	1758.6	1869.1	90.9	3614.9	1182.4	4372.5	1262.4	78.21%	1141.7	239	50	Expansion	C	71.8	3.94E+04	164.6
Exp-C-100	16.7	210.0	64.6	301.3	233.5	1711.0	1864.3	109.3	3401.8	1151.7	4362.8	1259.7	72.51%	1826.5	239	100	Expansion	C	134.7	7.59E+04	318.0
Exp-C-200	8.0	210.0	64.9	302.1	232.5	1654.9	1869.7	124.2	3163.7	1111.0	4375.4	1263.1	65.96%	2924.9	235	200	Expansion	C	257.4	1.50E+05	637.2
Exp-C-500	3.0	210.0	65.0	302.5	232.1	1546.9	1869.6	137.2	2858.9	1036.7	4375.9	1263.2	58.54%	5070.1	230	500	Expansion	C	606.0	3.76E+05	1639.1
Exp-D-50	33.4	209.9	65.0	302.6	231.8	1735.3	1870.7	46.1	3882.6	1166.9	4375.9	1263.1	87.24%	1140.7	484	50	Expansion	D	81.4	4.52E+04	93.5
Exp-D-100	16.1	209.9	65.1	302.7	231.7	1676.1	1871.0	58.2	3687.7	1126.8	4378.0	1263.7	82.23%	1842.0	485	100	Expansion	D	158.8	9.13E+04	188.3
Exp-D-200	7.5	209.9	65.2	303.2	231.1	1562.2	1872.6	72.1	3430.8	1046.3	4381.8	1264.7	76.50%	2949.2	489	200	Expansion	D	317.4	1.95E+05	398.8
Exp-D-500	2.7	210.0	65.1	303.1	231.3	1399.8	1871.6	88.2	3074.4	933.8	4380.4	1264.3	68.69%	5250.8	499	500	Expansion	D	789.9	5.40E+05	1080.3
Exp-E-50	33.5	209.9	65.2	303.2	231.0	1741.2	1872.6	30.8	3935.2	1172.8	4380.6	1264.3	88.64%	1137.7	621	50	Expansion	E	82.5	4.57E+04	73.6
Exp-E-100	15.9	209.9	65.3	302.7	231.6	1653.8	1879.3	46.1	3717.0	1112.3	4397.0	1269.2	83.27%	1935.6	628	100	Expansion	E	163.9	9.54E+04	151.9
Exp-E-200	7.5	210.1	66.8	303.3	231.1	1565.6	1918.3	60.5	3503.7	1048.5	4491.8	1296.5	76.83%	2961.7	635	200	Expansion	E	326.2	2.00E+05	315.0
Exp-E-500	2.6	210.0	65.0	301.5	233.2	1334.4	1875.0	83.8	3059.3	887.9	4387.0	1266.7	69.59%	5201.3	668	500	Expansion	E	840.7	6.01E+05	899.8

**These data are available in electronic form as well*

Appendix C: Nomenclature

Terms, Abbreviations, and Acronyms:

CAES	Compressed Air Energy Storage
EDM	Electrical discharge machining; fabrication process used to produce stainless steel interrupted plates
FR	Flow rate
GHG	Greenhouse gas
PI	Proportional-Integral; control system used in experiments
Power Density	Rate of energy storage or regeneration, normalized by the displacement of compressor/ expander; See Eqns. (3.11) & (3.12)
PPA	Power per unit area, area-normalized power density; used to compare different experiments by accounting for compressor/ expander size, compression/ expansion time, and the surface area; See Eqn. (3.13)
SSA	Specific surface area, specific surface; surface area per unit volume
RPS	Renewable portfolio standard; legislation requiring a percentage of energy production to come from renewable sources
VeroWhite	Trade name of photopolymer used in 3D printing process of plastic interrupted plate inserts

English Letter Symbols:

A	Surface area
a	Power-weighted specific surface area
D	Diffusion coefficient
D_h	Hydraulic diameter
dU	Infinitesimally small change in internal energy
E	Energy stored or recovered
h	Convective heat transfer coefficient
hA	Product of heat transfer coefficient and area
L/D	Instantaneous ratio of air column height (length) to chamber diameter
K	Bulk modulus
Nu_{dh}	Nusselt number based on hydraulic diameter
P_{air}	Air pressure
P_{high}	Pressure of high pressure reservoir
P_{low}	Pressure of low pressure reservoir
P_0	Initial pressure of air in chamber
Pr	Prandtl number
$\dot{Q}$	Heat transfer rate
R	Specific gas constant for air, 287 J/kg K
Re_{dh}	Reynolds number based on hydraulic diameter
SSA_{pwr}	Power-weighted specific surface area; See Eqn. (5.2)

T_{air}	Air temperature
T_{media}	Porous medium temperature
T_0	Initial air temperature
t	Compression/ expansion time
t_f	Time at end of compression/ expansion process
t_0	Time at beginning of compression/ expansion process
V_{add}	Volume of water added to the chamber, measured with encoder
V_{air}	Air volume
V_{cham}	Chamber volume
V_{char}	Characteristic velocity
V_f	Volume of air at process end
V_{ins}	Solid volume of porous insert
$V_{iso,l}$	Maximum volume of air along an isotherm
$V_{iso,s}$	Minimum volume of air along an isotherm
V_{piston}	Piston velocity
V_{wat}	Volume of water in the system
V_0	Initial air volume
V_{0e}	Volume of undissolved air in the water at P_0
W_{ejec}	Ejection work
$\underline{x}$	Normalized position of water hydraulic cylinder rod, varies from 0 to 1
Z	Compressibility factor

Greek Letter Symbols:

ΔT	Temperature difference between air and media
δQ_{out}	Infinitesimally small quantity of thermal energy transferred out of a system
δW_{in}	Infinitesimally small amount of work done on a system
μ	Gas viscosity
η	Efficiency, compression or expansion
η_{comp}	Compression efficiency; defined in Eqn. (3.6)
$\eta_{comp,ejec}$	Compression efficiency, with ejection work; defined in Eqn. (3.9)
η_{exp}	Expansion efficiency; defined in Eqn. (3.7)
$\eta_{exp,ejec}$	Expansion efficiency, with ejection work; defined in Eqn. (3.10)
ρ	Gas density
ρ_{rec}	Expansion power density based on recovered energy
ρ_{stor}	Compression power density based on stored energy

Appendix D: Grayscale Reprints of Select Figures

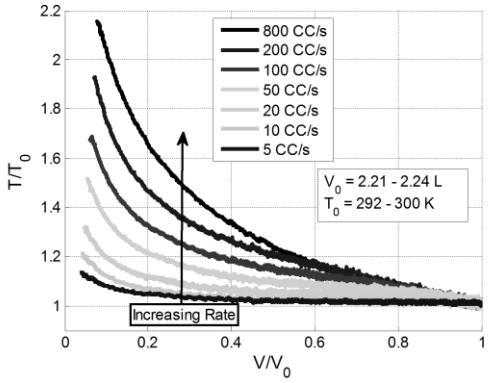

Fig. 5.1.9

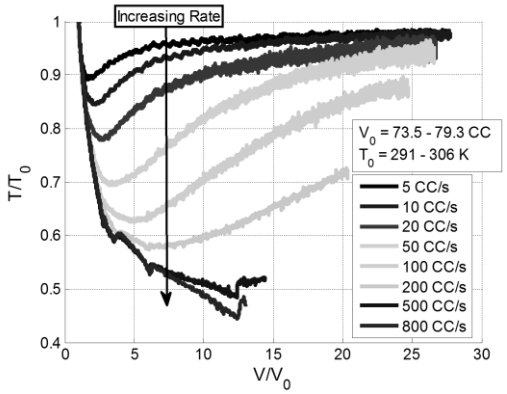

Fig. 5.1.10

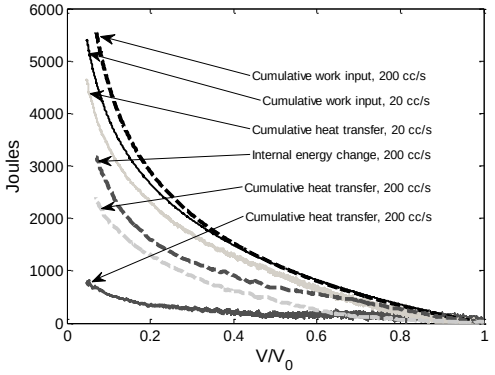

Fig 5.1.11

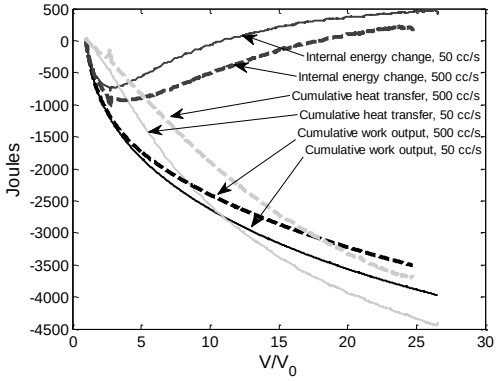

Fig. 5.1.12

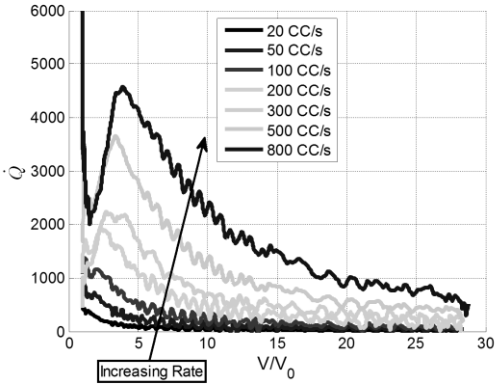

Fig. 5.2.6

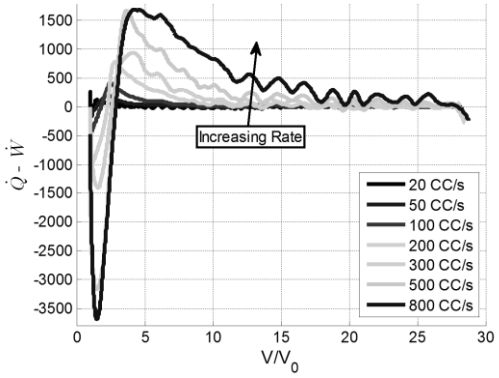

Fig. 5.2.7

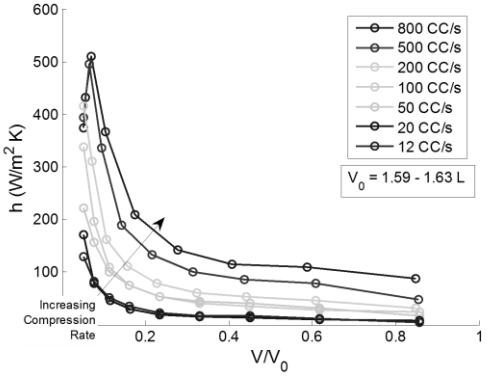

Fig. 5.2.8

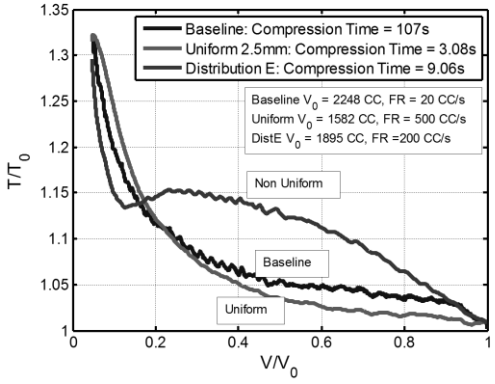

Fig. 5.4.1

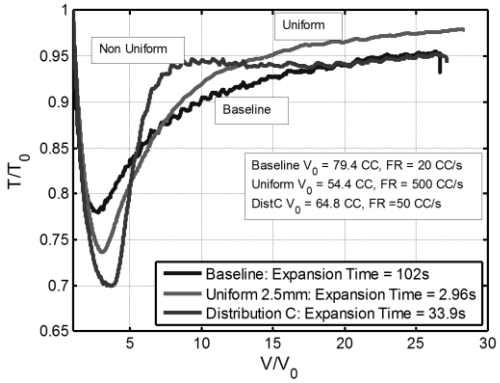

Fig. 5.4.2

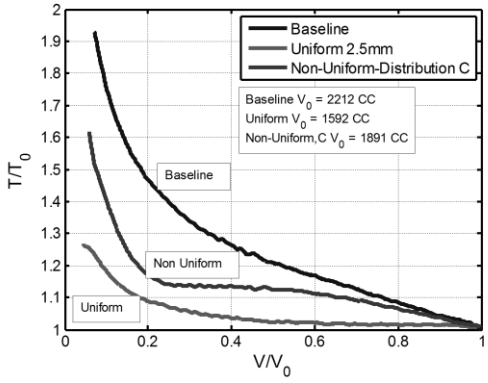

Fig. 5.4.3

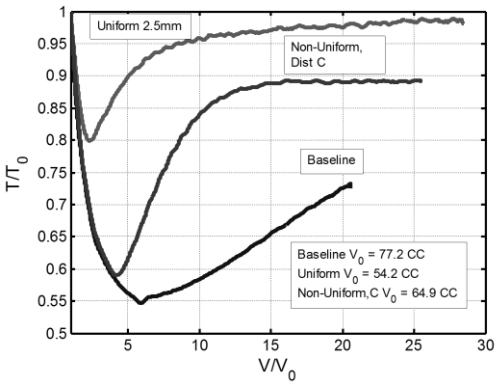

Fig. 5.4.4

*** Figures are available in electronic form as well.*